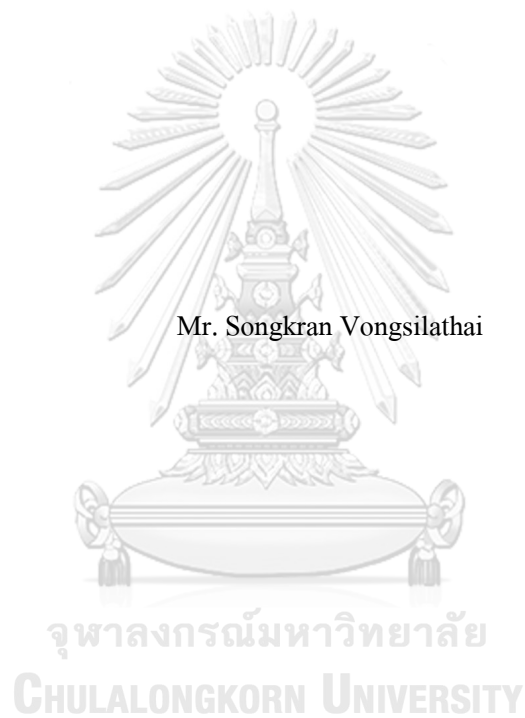Effects of Thiosulfate in Artificial Seawater on Corrosion Behaviour

of 25Cr-3Ni-7Mn-0.66N New Duplex Stainless Steel

Mr. Songkran Vongsilathai

A Thesis Submitted in Partial Fulfillment of the Requirements

for the Degree of Master of Engineering in Metallurgical and Materials Engineering

Department of Metallurgical Engineering

FACULTY OF ENGINEERING

Chulalongkorn University

Academic Year 2020

ผลของไทโอซัลเฟตในน้ำทะเลเทียมต่อพฤติกรรมการกัดกร่อน
ของ 25Cr-3Ni-7Mn-0.66N เหล็กกล้าไร้สนิมดูเพล็กเกรดใหม่

นายสงกรานต์ วงษ์ศิลาทัย

จุฬาลงกรณ์มหาวิทยาลัย
CHULALONGKORN UNIVERSITY

วิทยานิพนธ์นี้เป็นส่วนหนึ่งของการศึกษาตามหลักสูตรปริญญาวิศวกรรมศาสตรมหาบัณฑิต
สาขาวิชาวิศวกรรมโลหการและวัสดุ ภาควิชาวิศวกรรมโลหการ
คณะวิศวกรรมศาสตร์ จุฬาลงกรณ์มหาวิทยาลัย
ปีการศึกษา 2563

Thesis Title	Effects of Thiosulfate in Artificial Seawater on Corrosion Behaviour of 25Cr-3Ni-7Mn-0.66N New Duplex Stainless Steel
By	Mr. Songkran Vongsilathai
Field of Study	Metallurgical and Materials Engineering
Thesis Advisor	Professor Dr. GOBBOON LOTHONGKUM, Ing.

Accepted by the FACULTY OF ENGINEERING, Chulalongkorn University in Partial Fulfillment of the Requirement for the Master of Engineering

Dean of the FACULTY OF
ENGINEERING

(Professor Dr. SUPOT TEACHAVORASINSKUN, D.Eng.)

THESIS COMMITTEE

Chairman

(Assistant Professor Dr. EKASIT NISARATANAPORN, Ph.D.)

Thesis Advisor

(Professor Dr. GOBBOON LOTHONGKUM, Ing.)

Examiner

(Assistant Professor Dr. PANYAWAT WANGYAO, Ph.D.)

Examiner

(Dr. NITHI SAENARJHAN, Ph.D.)

External Examiner

(Dr. Ekkarut Viyanit, Ing.)

สงกรานต์ วงษ์ศิลาทัย : ผลของไทโอซัลเฟตในน้ำทะเลเทียมต่อพฤติกรรมการกัดกร่อน ของ 25Cr-3Ni-7Mn-0.66N เหล็กกล้าไร้สนิมดูเพล็กซ์เกรดใหม่. (Effects of Thiosulfate in Artificial Seawater on Corrosion Behaviour of 25Cr-3Ni-7Mn-0.66N New Duplex Stainless Steel) อ.ที่ปรึกษาหลัก : ศ. ดร.กอบบุญ หล่อทองคำ

ในงานวิจัยนี้ได้เตรียมเหล็กกล้าไร้สนิมดูเพล็กซ์เกรดใหม่ คือ 25Cr-3Ni-7Mn-0.66N ด้วยการหลอมอาร์ก ในเตาสุญญากาศ นำไปผ่านการกดอัด และอบชุบทางความร้อน ตามแผนภูมิสมดุลที่ได้จากการคำนวณด้วยโปรแกรม Thermo-Calc ที่อุณหภูมิ 1250 °C 1 ชั่วโมง ชุบในน้ำ และ 1050 °C เวลา 1.5 ชั่วโมง ชุบในน้ำ ตรวจสอบโครงสร้าง จุลภาค สัณฐานวิทยา และส่วนผสมทางเคมี ด้วยเครื่องมือวิเคราะห์ต่างๆ ศึกษาพฤติกรรมการกัดกร่อนในน้ำทะเลเทียม ตามมาตรฐาน ASTM D1141 ที่อุณหภูมิ 25°C และในน้ำทะเลเทียมผสมสารไทโอซัลเฟตสภาพเป็นกรด เปรียบเทียบ กับพฤติกรรมการกัดกร่อนของเหล็กกล้าไร้สนิมดูเพล็กซ์เกรดมาตรฐาน 2205 ด้วยวิธีการทางไฟฟ้าเคมี เหล็กกล้าไร้ สนิมดูเพล็กซ์เกรดใหม่มีโครงสร้างจุลภาคเป็นเฟร์ไรต์และออสเทไนต์ สัดส่วนโครงสร้างจุลภาคเฟร์ไรต์ต่อออสเท ไนต์เป็น 59:41 ไม่พบตะกอนของเฟสทุติยภูมิ ผลการทดลองทางไฟฟ้าเคมีพบว่าในน้ำทะเลเทียมเหล็กกล้าไร้สนิมดู เพล็กซ์เกรดใหม่มีพฤติกรรมการกัดกร่อนเหนือกว่าเหล็กกล้าไร้สนิมดูเพล็กซ์เกรดมาตรฐาน แต่ในน้ำทะเลเทียมผสม ไทโอซัลเฟตสภาพเป็นกรด พฤติกรรมการกัดกร่อนของเหล็กกล้าไร้สนิมเกรดใหม่ด้อยกว่าเกรดมาตรฐาน ผลการ ทดลองด้วยเทคนิคโพลาไรเซชัน และเทคนิคอิมพีแดนซ์ พบว่าพฤติกรรมการกัดกร่อนของเหล็กกล้าไร้สนิมดูเพล็กทั้ง สองเกรดด้อยลง ในน้ำทะเลเทียมผสมสารไทโอซัลเฟตสภาพเป็นกรด เมื่อความเข้มข้นของไทโอซัลเฟตสูงขึ้น ความ ต้านทานการกัดกร่อนแบบรูเข็มของโครงสร้างจุลภาคเฟร์ไรต์น้อยกว่าโครงสร้างจุลภาคออสเทไนท์ เนื่องจากพบการ เกิดรูเข็มในโครงสร้างจุลภาคเฟร์ไรต์ สอดคล้องกับการเปรียบเทียบจากการคำนวณค่าความต้านทานการกัดกร่อนแบบ รูเข็ม (PREN$_{16}$) ของแต่ละโครงสร้างจุลภาค ผลการวิเคราะห์ด้วยเทคนิคม๊อต-ชอทท์กี้ (Mott-Schottky) พบว่าฟิลม์พาส ซิฟของดูเพล็กซ์ทั้งสองเกรดประกอบด้วยสองชั้น ทั้งในน้ำทะเลเทียม และน้ำทะเลเทียมผสมไทโอซัลเฟตสภาพเป็น กรด ชั้นในและชั้นนอกของพาสสีฟฟิล์มเป็นสารกึ่งตัวนำประเภท p (p-type semiconductor) และเป็นสารกึ่งตัวนำ ประเภท n (n-type semiconductor) ตามลำดับ ในน้ำทะเลเทียม ค่าความหนาแน่นของที่ว่างไอออนประจุลบและประจุ บวกของฟิล์มพาสซิฟทั้งชั้นในและชั้นนอกของดูเพล็กซ์เกรดใหม่มีค่าน้อยกว่าค่าความหนาแน่นของว่างไอออนประจุ ลบและประจุบวกของเกรดมาตรฐานตามลำดับ แต่ในน้ำทะเลเทียมผสมไทโอซัลเฟตสภาพเป็นกรดค่าความหนาแน่นที่ ว่างไอออนประจุลบและประจุบวกของฟิล์มพาสซิฟทั้งชั้นในชั้นนอกของดูเพล็กซ์เกรดใหม่มีค่ามากกว่าค่าความ หนาแน่นของว่างไอออนประจุลบและประจุบวกของเกรดมาตรฐานตามลำดับ การวิเคราะห์ผลการทดลองได้ใช้ แผนภูมิปูแบร์ (Pourbaix) และแบบจำลองข้อบกพร่องแบบจุด (Point defect model, PDM) ในการอภิปรายพฤติกรรม การกัดกร่อนในน้ำทะเลเทียมและน้ำทะเลเทียมผสมไทโอซัลเฟตสภาพเป็นกรด

สาขาวิชา	วิศวกรรมโลหการและวัสดุ	ลายมือชื่อนิสิต ....
ปีการศึกษา	2563	ลายมือชื่อ อ.ที่ปรึกษาหลัก ....

6070332521 : MAJOR METALLURGICAL AND MATERIALS ENGINEERING

KEYWORD: Duplex stainless steel, Polarisation, Impedance, Mott-Schottky, Point defect model (PDM)

           Songkran Vongsilathai : Effects of Thiosulfate in Artificial Seawater on Corrosion Behaviour of 25Cr-3Ni-7Mn-0.66N New Duplex Stainless Steel. Advisor: Prof. Dr. GOBBOON LOTHONGKUM, Ing.

In this research, the 25Cr-3Ni-7Mn-0.66N new duplex stainless steel (DSS) was fabricated by the vacuum arc re-melting (VAR) process, then deformed by hot-forging process, and subsequently heat-treated at 1250°C for 1 hr + water quenched + 1050°C for 1.5 hr + water quenched., based on the calculation of the phase diagram by Thermo-Calc software. The material characterisations and chemical compositions were examined by various methods. The corrosion behaviours of the new duplex in artificial seawater (ASW) after ASTM D1141 and in artificial seawater mixing with thiosulfate was studied at 25°C and compared with that of the 2205 standard DSS by electrochemical methods. The final microstructures are ferrite and austenite. The phase ratio of ferrite to austenite is 59:41. The secondary phases were not found in the new duplex grade. The electrochemical test results show that the corrosion behaviours of the new duplex grade were better than that of 2205 DSS in the ASW, but it was reversed in the acidified ASW mixing with thiosulfate. According to the Polarisation and Electrochemical Impedance Spectroscopy test results, it is found that the corrosion behaviours on both duplex grades were more deteriorated when increasing the thiosulfate concentration in the acidified ASW mixing with thiosulfate. The pitting resistance of ferrite is lower than that of austenite since the pit exhibits in ferrite. It is confirmed by the $PREN_{16}$ calculation results of ferrite and austenite. The Mott-Schottky analysis showed the bi-layer structure of the passive film in both the ASW and the acidified ASW mixing with thiosulfate. The passive film structure consists of the p-type semiconductor inner layer and the n-type semiconductor outer layer. In the ASW, the densities of cation and anion vacancies in the inner and outer layer of new duplex steel are lower than that of 2205 DSS, respectively. However, in the acidified ASW mixing with thiosulfate, the densities of cation and anion vacancies in the inner and outer layer of new duplex steel are higher than that of 2205 DSS, respectively. The corrosion behaviours of two duplex grades in both the ASW and the acidified ASW mixing with thiosulfate were discussed based on the Pourbaix diagram and the Point Defect Model (PDM).

Field of Study:	Metallurgical and Materials Engineering	Student's Signature	
Academic Year:	2020	Advisor's Signature	

ACKNOWLEDGEMENTS

TABLE OF CONTENTS

จุฬาลงกรณ์มหาวิทยาลัย
CHULALONGKORN UNIVERSITY

LIST OF TABLES

LIST OF FIGURES

CHAPTER 1

INTRODUCTION

1.1   Background

Duplex stainless steel (DSS) is widely known as a positive candidate in severe environment services because of an excellent combination of mechanical properties and corrosion resistance [1]. Due to the high prices of Chromium (Cr), Nickel (Ni) and Molybdenum (Mo), a lean DSS alloying with lower element contents than normal DSS has been developed for cost-reduction [2, 3]. Nonetheless, the lean DSS is both lower in mechanical and corrosion properties than the normal DSS. To keep good mechanical properties, Manganese (Mn) and Nitrogen (N) are added to replace Ni. N also enhances the corrosion resistance of DSS.

Regarding to the previous studies [4] on the alloy series of (21-39) Cr and (5-28) Ni DSS, it was pointed out that the highest pitting corrosion resistance DSS was 28.5Cr-9Ni. G. Lothongkum and coworkers [5] continued to develop micro-duplex stainless steels of 28Cr-7Ni with various N contents. They found that for enough pitting corrosion resistance in 3.5 wt.% NaCl solution, it is not necessary to add more than 0.13 wt.% of N. This conformed that Nitrogen in the form of a solid solution in crystal lattice provides beneficial pitting corrosion resistance of DSS [1]. Although those investigated duplex alloys performed good pitting corrosion resistance in neutral chloride solution, their Cr and Ni contents were too high. Note that, it is necessarily accounting for further development of a new duplex grade by replacing Ni with Mn and N concerns an acceptable pitting corrosion resistance.

Thiosulfate salts ($Na_2S_2O_3$) acts as important role in many industrial systems such as pulp and paper, agricultural industry, gold leaching technologies, oil and gas pipelines platform and desalination system [6, 7]. The association reaction of thiosulfate anion ($S_2O_3^{2-}$) can be decomposed to a compound of sulphur species in the polythiooxyanions group, resulted in the degradation of metal and alloys [6-8]. Many works attempted to investigate the corrosion behaviours of stainless steel in the presence of thiosulfate and chloride solution [9-18]. Their results confirmed synergistic effects of chloride and thiosulfate would deteriorate the passivity on

stainless steels. However, a few attentions were paid to the corrosion susceptibility in the presence of thiosulfate in artificial seawater of the high Mn-N DSS.

This work continues to develop a new DSS by decreasing the Chromium and Nickel contents of 28.5Cr-9Ni and replacing Nickel with Manganese and Nitrogen. The new 25Cr-3Ni-7Mn-0.66N DSS, a high Mn-N DSS, was fabricated in a vacuum arc re-melting process and heat-treated in a duplex region according to the phase diagram. The corrosion behaviours of new duplex were investigated by electrochemical approaches in the artificial seawater solution (ASW) compared to the standard and super duplex grades. Furthermore, in an acidified ASW with varying thiosulfate concentration, the corrosion susceptibility was compared between the new duplex and the standard duplex grade. The passive film characteristics were discussed along with the point defect model (PDM) proposed by Digby D. Macdonald [19]. Figure 1-1 displays the overview of this work.

Sample preparation (fabrication and sequencing of heat-treatment steps) of the new 25Cr-3Ni-7Mn-0.66N duplex grade

$\downarrow$

Metallurgical characterisation (OES, Nitrogen analysis, OM, XRD, V_f, EPMA)

$\downarrow$

Electrochemical tests in neutral ASW and acidified ASW with varying thiosulfate concentrations of new duplex and 2205 DSS samples via various electrochemical approaches and pit morphology investigation in weaker phase.

Figure 1-1 Sequencing overview in this present study

1.2   Objectives

—   To achieve a newly developed duplex stainless steel casting by vacuum arc re-melting (VAR) process.

—   To study the effects of thiosulfate on corrosion behaviours of new duplex stainless steel in artificial seawater solution by electrochemical methods.

1.3   Scopes

—   Evaluation of the proper chemical composition and solution annealing temperature of economical Ni-saving duplex stainless steel via Thermo-Calc software package.

—   Sample preparation via vacuum arc remelting (VAR) method with determination arc parameter in mixed $Ar+N_2$ atmosphere.

—   Sample characterisations by various techniques such as optical microscopy (OM) and scanning electron microscopy (SEM), spark-optical emission spectroscopy (OES), Nitrogen analysis, X-ray diffractometry (XRD), electron probe microanalysis (EPMA) equipped with 5 channels wavelength dispersive X-ray analyser (WDS).

—   Scrutinising the effects of thiosulfate in artificial seawater on corrosion behaviour of the new duplex grade and standard duplex grade by various electrochemical techniques such as open circuit potential (E_{ocp}) measurements, potentiodynamic and potentiostatic polarisation tests, electrochemical impedance spectroscopy (EIS), and Mott-Schottky (M-S) analysis.

1.4   Advantages of work

—   To realise how to develop new DSSs with concerning economical cost-saving alloying elements and broaden alternative alloys for marine application.

—   To know how to fabricate the stainless steels casting by vacuum arc re-melting (VAR) and provide suitable parameters in arc operation.

—   To comprehend the effects of thiosulfate in artificial seawater (ASW) on corrosion behaviours of new duplex stainless steels.

CHAPTER 2

LITERATURE REVIEWS

This chapter is distributed into three main sections. The first section is an introduction of duplex stainless steels. Then, the electrochemical behaviour and passivity breakdown with defect in passive layer are discussed. Subsequently, it is the literature surveys of the synergistic effects of thiosulfate and chloride on electrochemical approaches.

2.1   Introduction of duplex stainless steel

2.1.1   Overview of duplex family

Two-phase ferrite–austenite stainless steels have been studied since the late 1920s [20]. In 1932, AVESTA Steelworks (Sweden) produced a ferrite–austenite material, which today is generally known as duplex steel. However, extensive use of this steel group has been started in the 1980s, due to increasing demands from the chemical industry. Scarcity of Ni caused conventional austenitic steel to become expensive [21].

Duplex stainless steels (DSSs) typically consist of 50:50 ratio in amounts of phase balance between δ-ferrite (BCC, body centred cubic crystallographic structure) and γ-austenite (FCC, face centred cubic crystallographic structure) [1, 20, 22]. The delta phase renders the high strength property and stress corrosion cracking (SCC) resistance while the gamma phase provides the toughness and general corrosion resistance [23]. Note that, DSSs have been chosen as an alternative stainless steels selection not only expecting the excellent mechanical property but also the acceptable corrosion susceptibility [24]. Due to their higher chromium contents (Cr > 22 wt.-%), they better function in severely corrosive environment compared with austenitic stainless steels. However, there were the fascinating metallurgical technology for steel production, resulting in the various duplex grades with different chemical compositions. The perception of alloy makers needs further to develop the economical saving of DSSs because of the substantial Nickel price in the recent years [2, 3, 22, 25-29]. It can be said that the leaner duplex grades have been lunched from that time on.

Table 2-1 General descriptions of duplex family

Descriptions	Ref.
• Lean duplex grades ($PREN_{16} > 21$) The intention of lean duplex is an apparent fluctuation of Ni and Mo price. The fact is to replace those ones with N and Mn. Among leaner grades are in strongly competition with the AISI 304L and 316L in volume market due to the higher yield strength and corrosion property. These grades are capable in a neutral environment.	[17, 20, 27, 30-32]
• Standard/Conventional duplex grades ($PREN_{16} > 34$) The most versatile in family is UNS S31208 and S32205 grades. The superior in corrosion protection and mechanical property are well-known in all of the stainless-steel series. It is crucial to point out that the well-known of "2205" duplex grade is not the trademark, but it is the compositional indication, namely 22 wt.% Cr and 5 wt.% Ni. The standard DSS has the Mo content is about 3 wt.-%. Its good corrosion resistance in chloride media.	[12, 33, 34]
• Super duplex grades ($PREN_{16} > 40$) The SDSS is typically minimum content of 25Cr, 3.5Mo and 0.2N in wt.-%. Their crevice resistance is generally accepted in these series. The grades are often specified instead of 6Mo austenitic grades. Their excellent corrosion performances are in strong acid with high temperature environment.	[1, 35, 36]
• Hyper duplex grades ($PREN_{16} > 50$) The excellent applicability of hyper DSSs in extremely corrosive or strong acid environment because of an extra high Cr additions (Cr > 27 wt.-%) combined with dedicated alloying levels in Mo, W or Cu, as well as, extra high N contents. These grades are endorsed in stress corrosion cracking (SCC) resistance.	[1, 35, 37]

Generally, duplex grades are classified according to their chemical compositions along with the Pitting Resistance Equivalent (PRE) number [38]. The PRE is an empirical value which approximates the pitting susceptibility in the chloride environment related to the elemental concentration regarding Cr, Mo, and N. The $PREN_{16}$ is expressed in the Equation 2.1, where the mass percent of Mo multiply with the coefficient of 3.3 and the mass percent of Nitrogen multiply by the coefficient of 16.

$$PREN_{16} = (\%Cr) + 3.3(\%Mo) + 16(\%N) \hspace{2cm} \text{Equation 2-1}$$

This is usually to distinguish the duplex grades into the Lean, Standard, Super, and Hyper duplex stainless steels, as shown in Table 2-1 [2, 3]. The designation of contemporary duplex grades with the chemical composition and $PREN_{16}$ values are listed in Table 2-2 [2, 3].
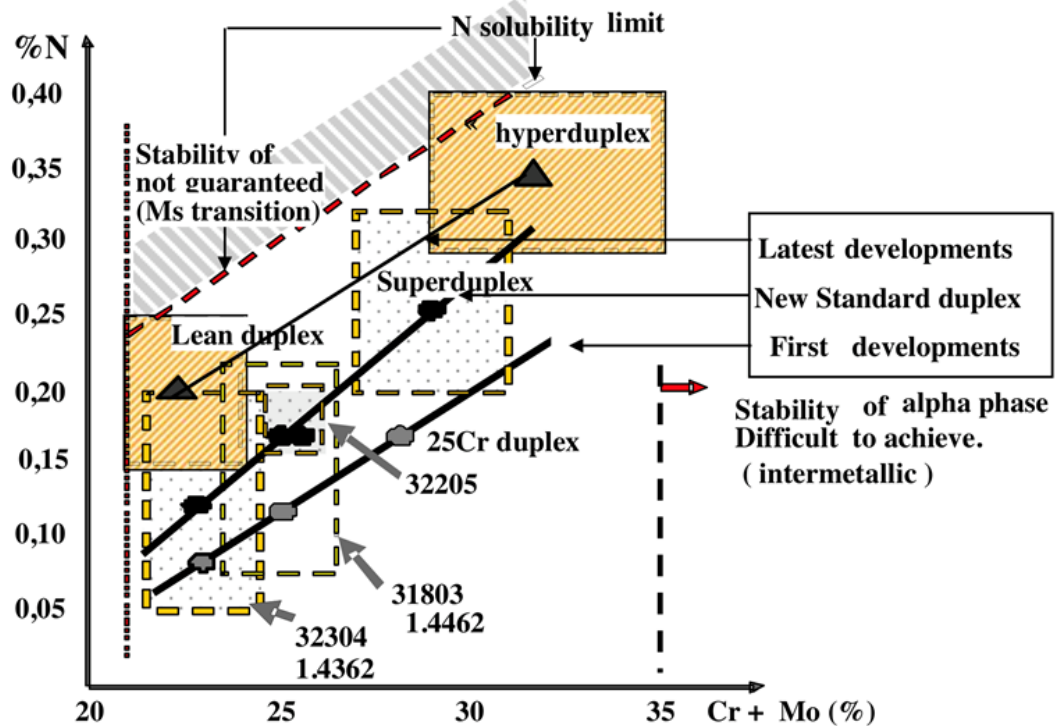
Figure 2-1 Trend of duplex stainless steels development with greater nitrogen contents [39]

The increasingly high demand for DSS usage and conventional stainless-steel casting in the industry has been restricted by fluctuating raw material prices of major alloying elements such as

Cr, Mo, mainly, Ni. There has a motivation to create a newly develop DSS by replacing expensive Ni with other austenite stabilisers such as Mn and N. Mn and N are austenite stabilisers, and they help to broaden the nitrogen solubility limit. N is also a powerful austenite stabiliser. The advantages of N increase the strength by interstitial solid solution in the crystal lattice and improve pitting susceptibility. As shown in the Figure 2-1, the development of different commercial DSS grades shows that the solubility limit of N increases with higher Cr and Mo contents which further improves the localised corrosion behaviour as well as mechanical properties [39].

2.1.2   In brief on metallurgy and corrosion resistance of duplex stainless steels

Chromium is a vital alloying element for stainless steel. A Cr content of at least 10.5% is needed to provide the stable passive film property obtaining the material corrosion resistance. Figure 2-2 displays a substantial decrease of corrosion rate profile with respect to Cr contents [40].
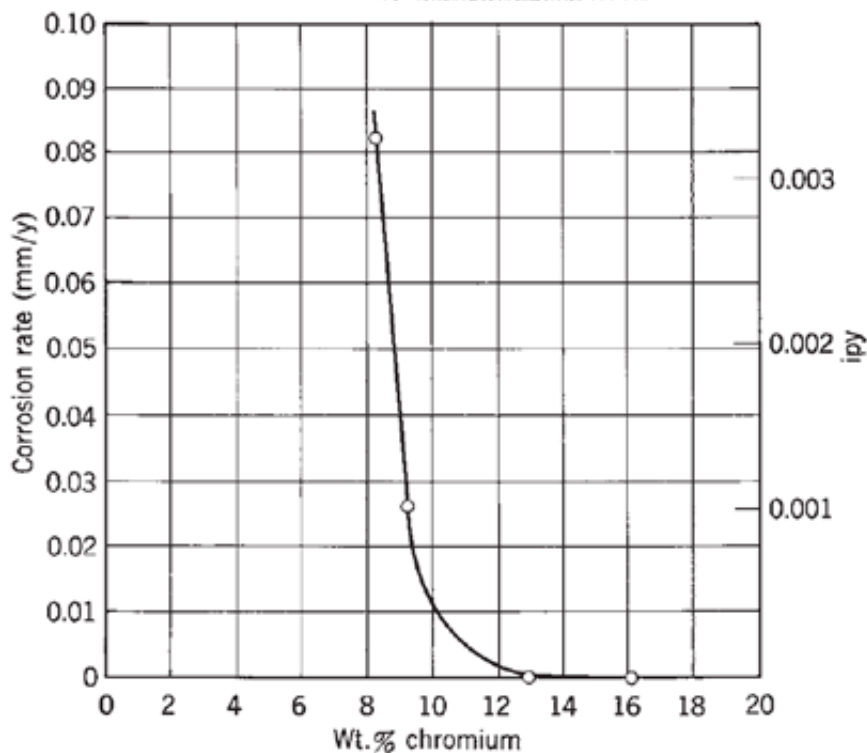
Figure 2-2 Corrosion rate of chromium-iron alloys in intermittent water spray at room temperature [40]

Table 2-2 Designation, composition and typical $PREN_{16}$ of some DSSs [2, 3]

Families	UNS	Standards	C	Cr	Ni	Mo	N	Mn	Cu	$PREN_{16}$
Lean duplex	S32001	1.4482	0.03	19.5-21.5	1.00-3.00	0.6	0.05-0.17	4.00-6.00	1	21-23
	S82012	1.4635	0.05	19.0-20.5	0.80-1.50	0.10-0.60	0.16-0.26	2.00-4.00	1	24-26
	S32101	1.4162	0.03	21.0-22.0	1.35-1.70	0.10-0.80	0.20-0.25	4.00-6.00	0.10-0.80	25-27
	S32202	1.4062	0.03	21.5-24.0	1.00-2.80	0.45	0.18-0.26	2	-	25-28
	S32304	1.4362	0.03	21.5-24.5	3.00-5.00	0.05-0.60	0.05-0.20	2.5	0.05-0.60	25-28
	S82031	1.4637	0.03	19.0-22.0	2.00-4.00	0.60-1.40	0.14-0.25	2.5	1	27-28
	S31500	1.4424	0.03	18.0-19.0	4.30-5.20	2.50-3.00	0.05-0.10	-	-	28-29
	S32900	1.446	0.03	23.0-25.0	2.50-5.00	1.00-2.00	-	1	-	30-31
	S82411	1.4662	0.03	23.0-25.0	3.00-4.50	1.00-2.00	0.20-0.30	2.50-4.00	0.10-0.80	33-34
Standard duplex	S31803	1.4462	0.03	21.0-23.0	4.50-6.50	2.50-3.50	0.08-0.20	2	-	33-35
	S32205	1.4462	0.03	22.0-23.0	4.50-6.50	3.00-3.50	0.14-0.20	2	-	35-36
Super duplex	S32520	1.4507	0.03	24.0-26.0	5.50-8.00	3.00-4.00	0.20-0.35	1.5	0.50-2.00	40-43
	S32550	1.4507	0.03	24.0-27.0	4.40-6.50	2.90-3.90	0.10-0.25	1.5	1.50-2.50	38-41
	S32750	1.441	0.03	24.0-26.0	4.40-6.50	3.00-5.00	0.24-0.32	1.2	0.5	40-43
	S32906	1.4477	0.03	28.0-30.0	5.80-7.50	1.50-2.60	0.30-0.40	0.80-1.50	0.8	41-43
Hyper duplex	S32707	-	0.03	26.0-29.0	5.50-9.50	4.00-5.00	0.30-0.50	1.5	1	49-50
	S33207	-	0.03	29.0-33.0	6.00-9.00	3.00-5.00	0.40-0.60	1.5	1	52-53

Typical phase diagram of duplex stainless steels

The early investigations of the metastable phase diagram of the Fe-Cr-Ni system (obtained for rapid cooling, such as casting or welding processes) started in the second decade of the 20th century with the works of Strass and Maurer [41], Scherer, Riedrich, and Hoch [42] and A. L. Schaeffler [43]. This type of bivariate graph, known as Schaeffler's diagram (see Figure 2-3), uses the equivalence coefficients of the alloying elements, either as ferrite or austenite stabilizers, to predict the final microstructure of the stainless steels (SSs) under metastable conditions as a function of the values of Cr and Ni equivalents (Cr_{eq} and Ni_{eq}, see Figure 2-3) [44]. These efficiently useful microstructure prediction tools are only based on the chemical composition of the stainless steels and the empirical equations of Cr_{eq} and Ni_{eq}.
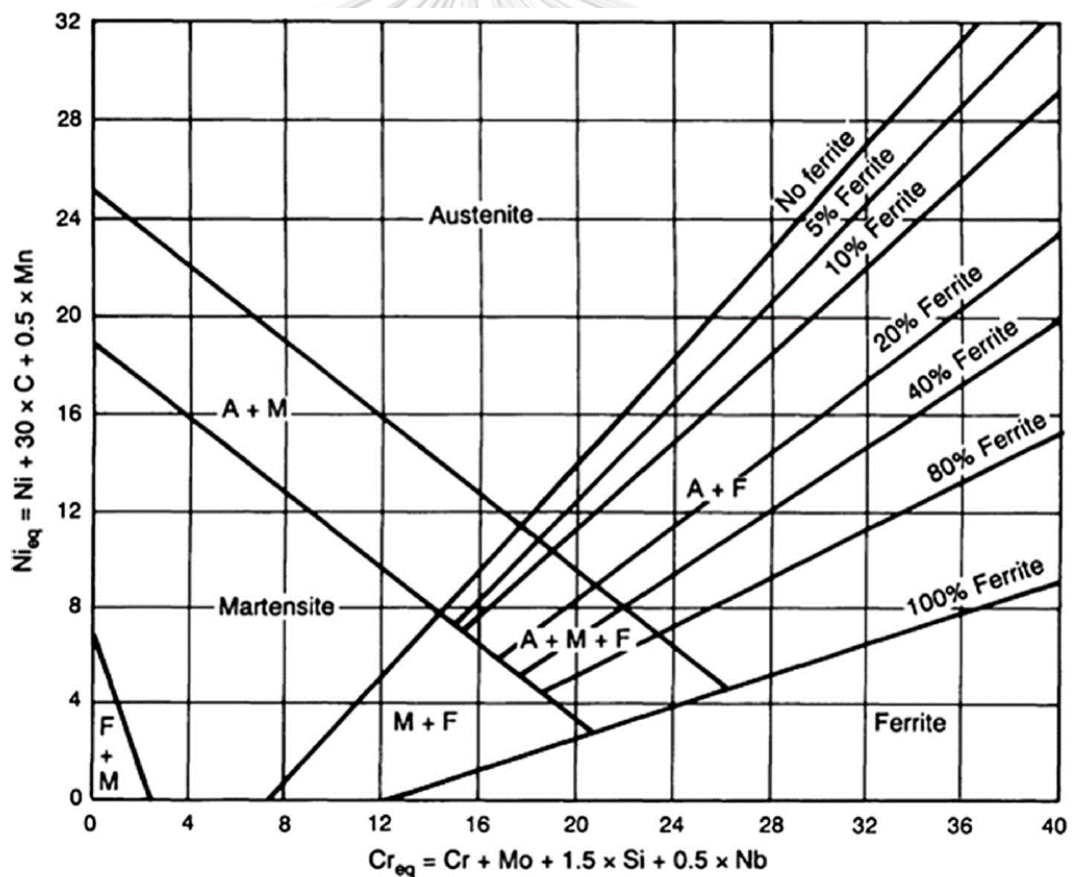
Figure 2-3 Schaeffler's constitution diagram, showing the microstructure of stainless steels after rapid cooling (casting and welding) according to the values of Cr and Ni equivalent [44]

Apart from the Schaeffler's diagram, the work of Bain and Griffith in 1927 reported their results on the Fe-Cr-Ni ternary system and mentioned the existence of a two-phase field comprising austenite and ferrite. That is to say, the first mention one of the stainless-steel family is duplex type. Figure 2-4 illustrated the ternary Fe-Cr-Ni phase diagram showing the presence of only three solid phases: austenite (γ), ferrite (α) and sigma phase (σ).
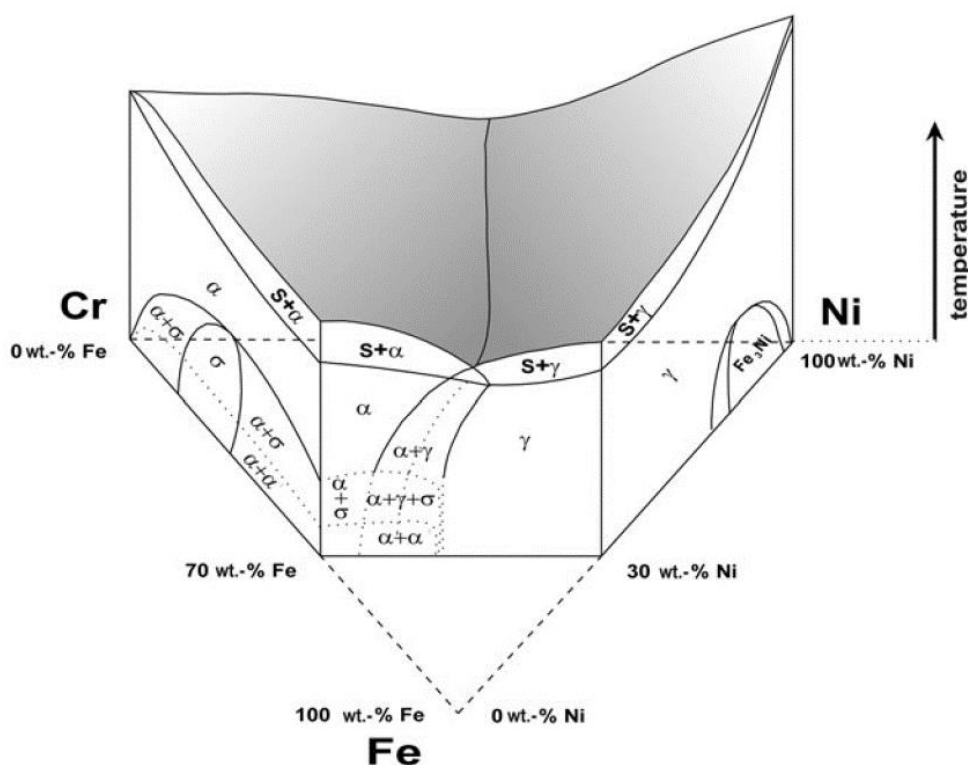
Figure 2-4 Quasi-binary section through the Fe-Cr-Ni diagram at 70 wt.-%Fe [21]

Solidification and austenite precipitation

Figure 2-5 shows the range of the existence of duplex steels (gray) and overview of phase transformation. Solidification of duplex steels is controlled by chemical composition. If the percentage of ferrite formers is high, the material will solidify at the chromium-rich side of the eutectic field, with the formation of α-crystals. Initially, the solidification is completely ferritic. On further cooling, a diffusion-controlled solid-state reaction takes place, resulting in inter-and intra-granular precipitations of the austenitic phase.
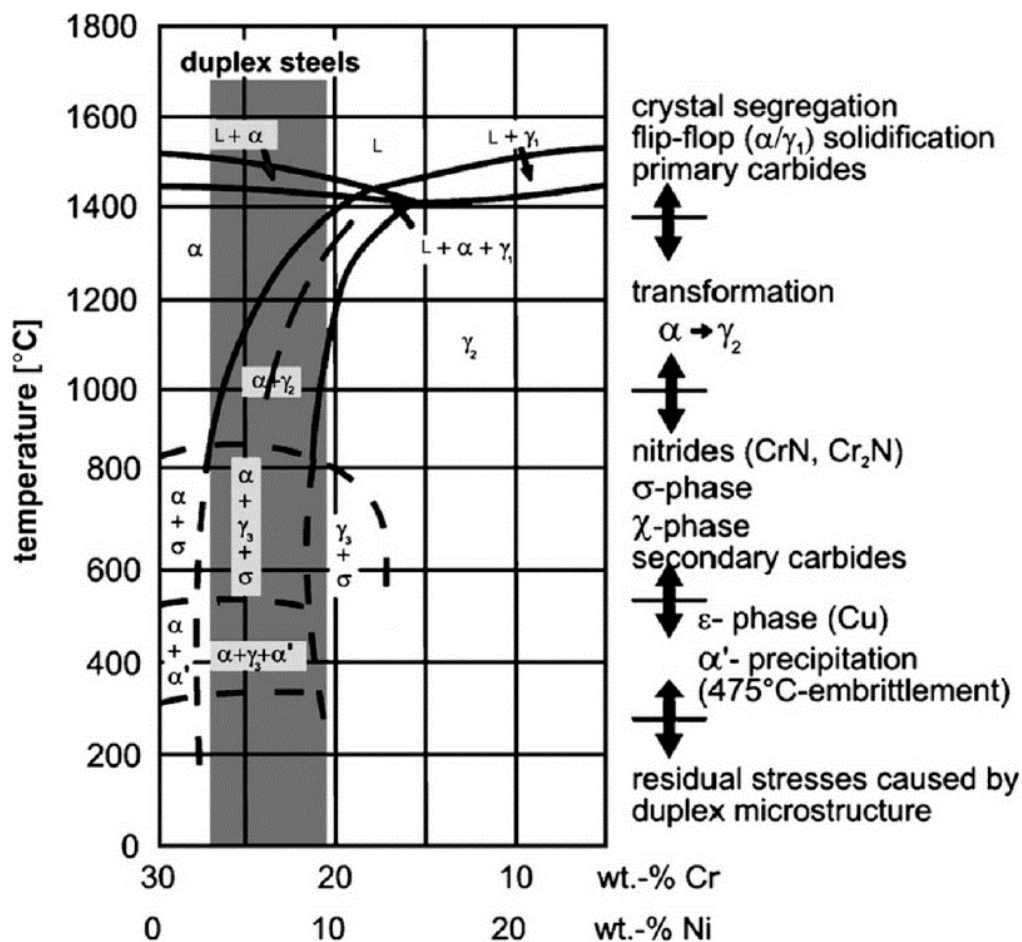
Figure 2-5 Pseudo-binary phase diagram of the Fe-Cr-Ni system [21]

The second possible route is a L→ α + γ₁ solidification which occurs close to the eutectic valley at a very slow cooling rate and with an increased number of austenite-stabilising elements (especially C and N). In this case, solidification begins with primary ferrite crystallisation from the liquid phase. The melt is hence depleted of ferrite-stabilising elements (e.g., Cr and Mo) and the concentration of austenite stabilisers (Ni, Cu, Mn, C, and N) increases. Equilibrium is thus shifted in the three-phase valley, which promotes formation of the γ-solid solution crystals. Formation of austenite leads to melt depletion of the austenite stabilisers and so ferrite solidification is again favoured.

Cooling down, the austenite ratio increases due to diffusion-driven growth of the γ-crystals, or also due to diffusion-controlled solid solution transformation. The austenite emerging "primarily" from the molten metal, as a result of the crystallization is indicated as γ₁ (L $\rightarrow$ α + γ₁). The

"secondary" austenite, γ_2, is formed by solid solution transformation from the ferritic phase ($\alpha \rightarrow \alpha + \gamma_2$).

During rapid cooling, and especially at low temperatures, a solid-state transformation of the ferrite into an austenite structure is possible due to a nearly diffusion-less transformation, which shows like martensite formation. The secondary austenite formed in this way has a similar composition to the ferritic matrix. The tertiary austenite γ_3 arises below 1,000 $^\circ$C, because of ferrite decomposition due to eutectoid solid-state reaction ($\alpha \rightarrow \sigma + \gamma_3$).

Influence of alloying elements on corrosion resistance in stainless steels.

The corrosion property of stainless steels is dependent due to the presence of the ferrite and austenite phases. To control the balance of phases and crystal structure in alloys, the effects of δ-stabiliser and γ-stabiliser should be considered on the basic Fe-Cr system. The δ-stabiliser is Cr and Mo alloying elements, in the other hand, the γ-stabiliser is Ni, Mn and Ni alloying elements. From now on, the influences of alloying elements in corrosion resistance will be discussed.
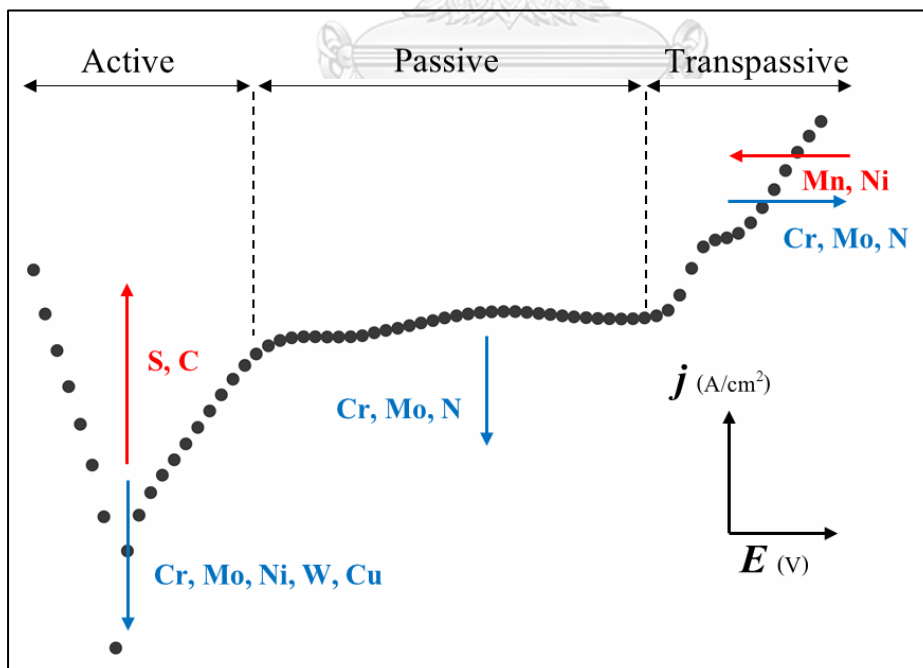
Figure 2-6 Summary of alloying elements influence on the potentiodynamic behaviour

Chromium (Cr)

The Cr is a vital alloying element for providing a passive character into the Fe-base system (see Figure 2-2) . Its content is relatively high in DSSs, typically 21-33 wt.-% to stabilise the ferrite phase. The stability of passive film would be enhanced, consequently, its excellent in strongly corrosive environment by Cr content of approximately 25-33 wt.-% in super and hyper duplex grades (Table 2-2). The Cr would reduce the corrosion current density (j_{corr}), thereby, higher corrosion rate in stainless steel. The stability of passive film would be enhanced lead to higher pitting resistance [45]. It is generally accepted that, the chromium oxide (Cr_2O_3) is spontaneous formation which acted as a barrier layer for protecting environment [46]. The formation of Cr rich inter-metallic phase at the adjacent of δ/γ grain boundaries, namely sigma phase (σ), at around 600-850°C would be deteriorated both mechanical and corrosion property due to the depletion of Cr content of the primary phases, see Figure 2-5.

Molybdenum (Mo)

The strong promoting alloying element for the crevice and pitting corrosion susceptibility is the Molybdenum. The favorable effects of Mo could be attributed to the formation of an MoO_3 type oxide [47]. The Mo accelerates the formation kinetics of the passive films and confers to stainless steels an increased resistance to de-passivation. The addition of Mo in duplex stainless steels should not exceed approximately 4% since it makes the material more susceptible to inter-metallic phase precipitation by widening the σ phase field.

Nickel (Ni)

The Nickel has a less positive effect than Chromium and Molybdenum. Ni addition reduces the corrosion rate of stainless steel when exposed in alkaline solution [40]. Ni had no effect on the pitting resistance of stainless steels in chloride solution [48]. In the duplex stainless steels, however, the main role of nickel is to maintain the ferrite-austenite balance, rather than to modify the corrosion resistance.

Copper (Cu)

The presence of copper always improves the corrosion resistance in acidified media. The most favorable effect is observed in the active region in the potentiodynamic polarisation curve because of the formation of passive film of this element from Cu^+ and Cu^{2+} cations initially taking into the solution by solution [49]. Cu is added to highly corrosion resistant in duplex grades such as Ferralium 255 (EN 1.4507, UNS S32550 and Zeron 100 (EN 1.4501, UNS S32760) to further improve the corrosion resistance in, for instance, reducing acids such as dilute sulphuric acid [50].

Tungsten (W)

Tungsten has become more commonly used as an alloying element in commercial stainless steels where it is used as a supplement to Mo for improved corrosion resistance. When used in the PRE expression, the factor for W is approximately half of that for Mo because of higher atomic weight. W has also been reported to promote formation of inter-metallic phases and cause a more rapid embrittlement than Mo [51].

Manganese (Mn)

Manganese element provides a negative effect on pitting susceptibility. Mn stabilises austenite and replaces partly Nickel. Mn Additions to stainless steel have been used to increase the solubility of Nitrogen, which have a strong beneficial influence on the pitting resistance [20, 22, 25-28]. It has been reported that Mn itself may have a negative effect on the pitting resistance, but combined additions of Nitrogen and Manganese override this effect [47].

Nitrogen (N)

Nitrogen has been used for 20 years because of its positive effect on the mechanical properties and corrosion properties of the stainless steels. It retards the precipitation of the intermetallic phases, which allow larger quantities of Cr and Mo to be added to the DSS to enhance passivation. Furthermore, N improves a corrosion resistance in acidified media, for it buffers the solution at the film/solution interface, via ammonia formation [25, 26, 52-54]. Levey et al., estimated that the N content required for achieving the same pitting resistance in both ferrite and

austenite in 22Cr steels is approximately 0.18%. In base metals with lower N content, the austenite would be less resistant to pitting [53].

2.1.3   Literatures of economical Ni-saving duplex stainless steels

A many of constructive research had been published the insight of new designed Ni-saving and high Mn-N duplex stainless steel [22, 28]. Zhang et al. [55] created the 21.5Cr-3.5Ni-0.2N with Mo-free DSS. Wan et al. [56] exhibited the 15Cr-2Ni with varying 1.2-2.8 wt.%Al and 8-12 wt.%Mn. DSS. Merello et al. [57] investigated a low-Ni, high-Mn-N DSS series and proposed an exponential equation for pitting corrosion resistance relating the pitting potential and the pitting resistance equivalent number (PREN). AN et al. [47] illustrated the preferential pitting at the grain boundaries and weaker phase by 27Cr-9Ni DSS with different contents of Mo and Mn. They found that Mo improved the pitting resistance whilst Mn reduced the PREN value and induced pit nucleation in the γ phase. Abdallah and Toor [58] exhibited the highest pitting potential on the 18Cr-5Mn-1Mo-0.22N new designed DSS. Moallemi et al. [59] scrutinised the ultra-fine grain 25Cr-8Mn-0.3N DSS for mechanical study and showed that an excellent UTS of ~900 MPa and elongation to fracture of ~94%. Zhao et al. [30] exhibited the transformation-induced-plasticity (TRIP) effect during plastic transformation and possessed an excellent combination of strength and ductility about 860 MPa and 63%, respectively, on 21.8Cr-4.52Mn-1.16Ni-0.16N lean DSS. These publications showed the constructive results of new DSS series with the highest N content alloy, which exhibited superior yield strength, ultimate tensile strength, and pitting (resistance) susceptibility.

Hence, the beneficial of N element, which in the form of solid solution in the crystal lattice, provides better corrosion resistance and mechanical property in duplex stainless steels [1, 60, 61]. Additionally, the invention of new duplex design, which parallels to the excellent corrosion property and mechanical performance, have been intense and inspired the alloy maker to find the alternative way for creating new DSS grades.

2.2   General aspect of electrochemistry approaches and stability of passive film

To measure a polarisation curve, one uses a dc current source called potentiostat/galvanostat and a three-electrode arrangement comprising the working electrode, the counter electrode, and a reference electrode. A potentiostat is essentially an electronic amplifier that regulates the current between the working electrode and the counter electrode in such a way as to keep the potential difference between the working electrode and the reference electrode constant [62].
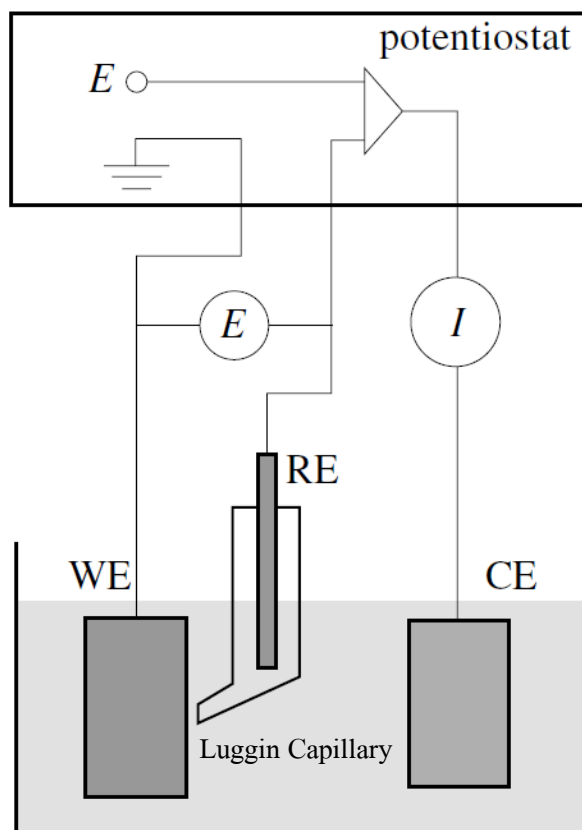
Figure 2-7 Experimental set up for potentiostatic polarisation. WE: working electrode, RE: reference electrode, CE: counter electrode [62]

The electrochemical cell components and their functions are described below (see Figure 2-7).

Counter electrode (CE): It passes current to the working electrode (specimen) to be studied.

Luggin Capillary: It is a probe filled with an electrolyte to provide an ionic conductive path through the soluble ionic salt (KCl). The Luggin capillary and salt bridge connecting the cell and

the **reference electrode (RE)** do not carry the polarising current, and it serves the purpose of reducing the ohmic resistance gradient through the electrolyte between the WE and AE.

Working electrode (WE): A 1-cm^2 exposed surface area is desirable. The distance between the WE surface and the tip of the Luggin capillary should be in the range of 1-2 mm. During an electrochemical corrosion experiment, the specimen immersion time must be constant in order to stabilise the electrode in the electrolyte prior to start the polarisation test.

2.2.1 Potentiodynamic polarisation method

Open circuit potential (E_{ocp}) measurement
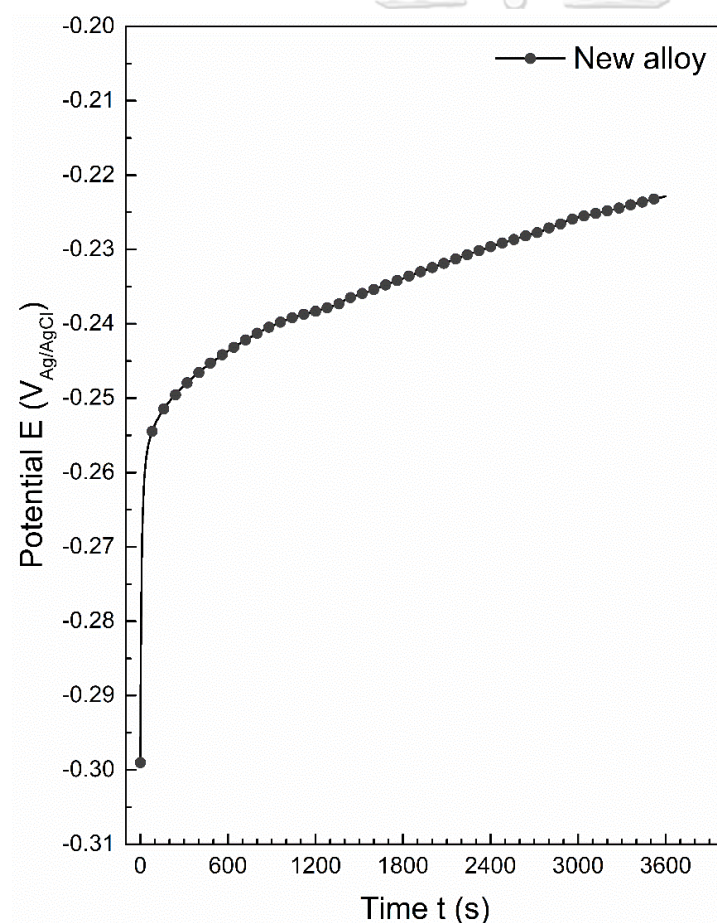
Figure 2-8 An example of E_{ocp} measurement for 1 hr in artificial seawater electrolyte

The open circuit potential (E_{ocp}) is the potential set up spontaneously by an electrode in the absence of an external current. For a single electrode, the open circuit potential is equal to the

equilibrium potential. In the mixed electrode undergoing corrosion, the open circuit potential is called the **corrosion potential** (E_{corr}). The corrosion potential is a value that lies in between the equilibrium potentials of the partial electrode reactions (anodic and cathodic reactions). In contrast to the equilibrium potential, which is a thermodynamic quantity, the corrosion potential is determined by kinetics; its value depends on the rates of both the anodic and the cathodic partial reactions present. Figure 2-8 shows an example of the open circuit potential measurement when the WE immersed in the studied electrolyte for 1 hr, then the E_{ocp} reaches to 0.22 $V_{Ag/AgCl}$.

Potentiodynamic polarisation curves
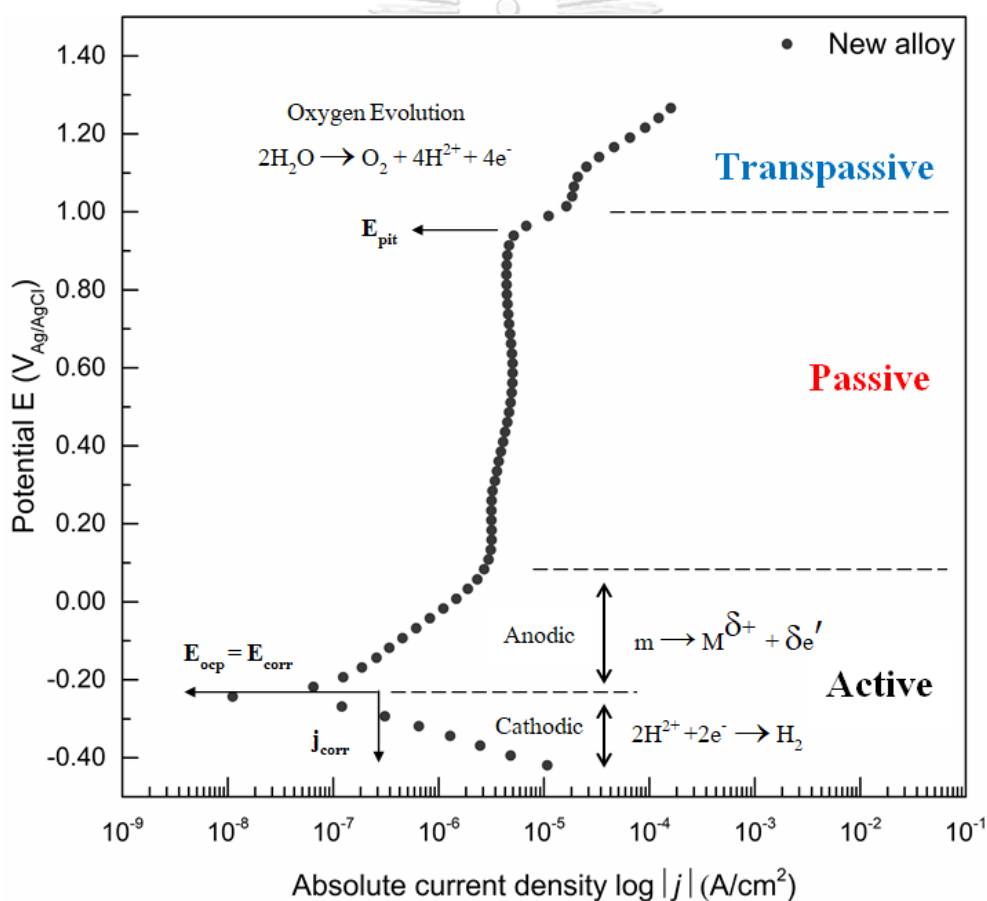
Figure 2-9 An example of potentiodynamic polarisation curves of passive metal immersed in chloride environment. This curve was run after the E_{ocp} measurement. E_{corr} : corrosion potential, j_{corr} : corrosion current density, E_{pit} : pitting potential

This is a technique that uses a programmed potentiostat to supply a continuously increasing potential (E) at a desired linear potential scan rate (dE/dt) along with a current logarithmic converter [63]. Note that, the diagram is recorded "signals" for characterising the electrochemical behaviour (the anodic and cathodic behaviours) and extracting kinetic parameters of those reactions of a WE.

Generally, the Fe-Cr alloys has a thin oxide layer formed on the surface substrate [46, 64], the passive film, which separates the metal from its environment. Typically, the thickness of passive film formed on the one is about 1-3 nm.

When the potential of Fe-Cr alloy is controlled and shifted in the anodic (positive) direction, the current required to cause that shift will vary. A demonstration of cathodic-anodic polarisation curve of Fe-Cr alloy in a neutral chloride environment is shown in Figure 2-9. This curve ran after the E_{ocp} measurement (see Figure 2-8), it can be said that $E_{ocp} = E_{corr}$. In this sense, the curve can be distinguished three regions of a passivation metal: the active region; the passive region; and the transpassive region.

In the active state (active dissolution), soluble ions, are formed and dissolve into the electrolyte, while the liberated electrons are taken up by an oxidising agent. The Equation can be written as

$$m \rightarrow M^{\delta+} + \delta e^{-}$$
Equation 2-2

where m: metal, M: metal cation, and δ: metal charge number. The reaction of active metal dissolution obeys the Butler-Volmer equation and therefore, the anodic current density increases monotonically with the potential [65, 66]. As for considering in the passive region, when a passive layer dissolves (passive dissolution), cations are formed by a charge transfer reaction at the metal/film interface. They migrate across the passive film to the film/solution interface, where they dissolve into solution as complexed ions (see Figure 2-10).

Metal	Passive film	Solution

$$(MO_{\chi/2})$$

$$m + \left(\tfrac{\chi}{2}\right)H_2O \rightarrow MO_{\frac{\chi}{2}} + \chi H^+ + \chi e'$$

$$MO_{\frac{\chi}{2}} + \chi H^+ \rightarrow M^{\delta+} + \left(\tfrac{\chi}{2}\right)H_2O + (\chi-\delta)e'$$

$$m \rightarrow M^{\delta+} + \delta e'$$
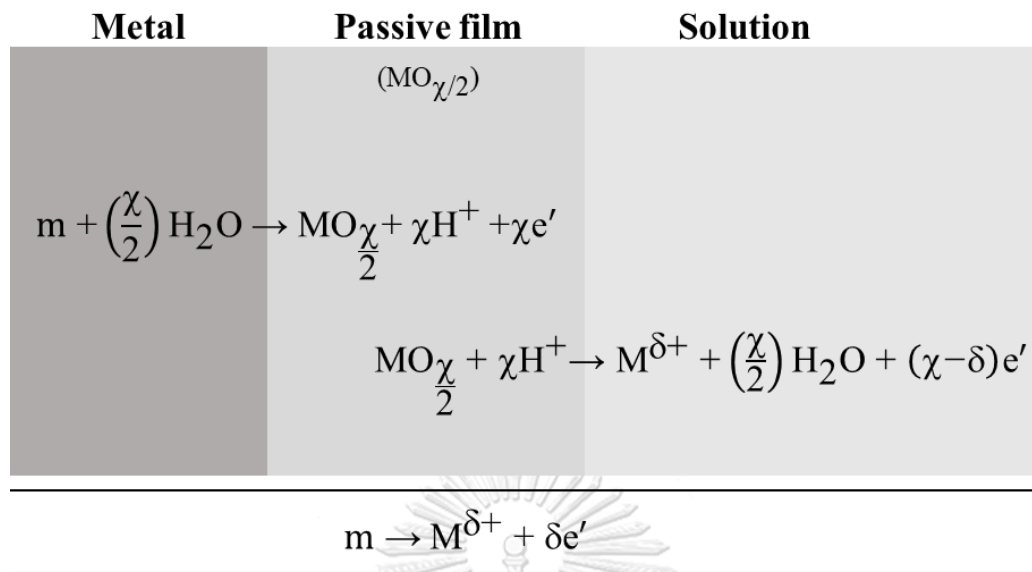
Figure 2-10 Schematic representation of passive disolution

The overall stoichiometric Equation 2.2 is the same for active and for passive dissolution but depending on the metal the charge number (δ). At the transpassive region, when the potential up to about 1.1 $V_{Ag/AgCl}$, the oxidation of water to oxygen becomes possible.

$$2H_2O \rightarrow O_2 + 4H^{2+} + 4e^- \qquad \qquad \text{Equation 2-3}$$

The corrosion rate analysis is calculated based on the result of fitting the cathodic-anodic Tafel slope using the Butler-Volmer equation [62, 63, 65, 66] that is given by

$$j_{tot} = j_a + j_c = j_{corr}\left[exp\left(E\text{-}E_{corr}/\beta_a\right) - exp\left(E\text{-}E_{corr}/\beta_c\right)\right] \qquad \text{Equation 2-4}$$

where j_a and j_c is the anodic and cathodic current density, respectively, E is the applied potential. The Tafel slopes of β_c and β_a are anodic branch and cathodic branch in V/decade, respectively.
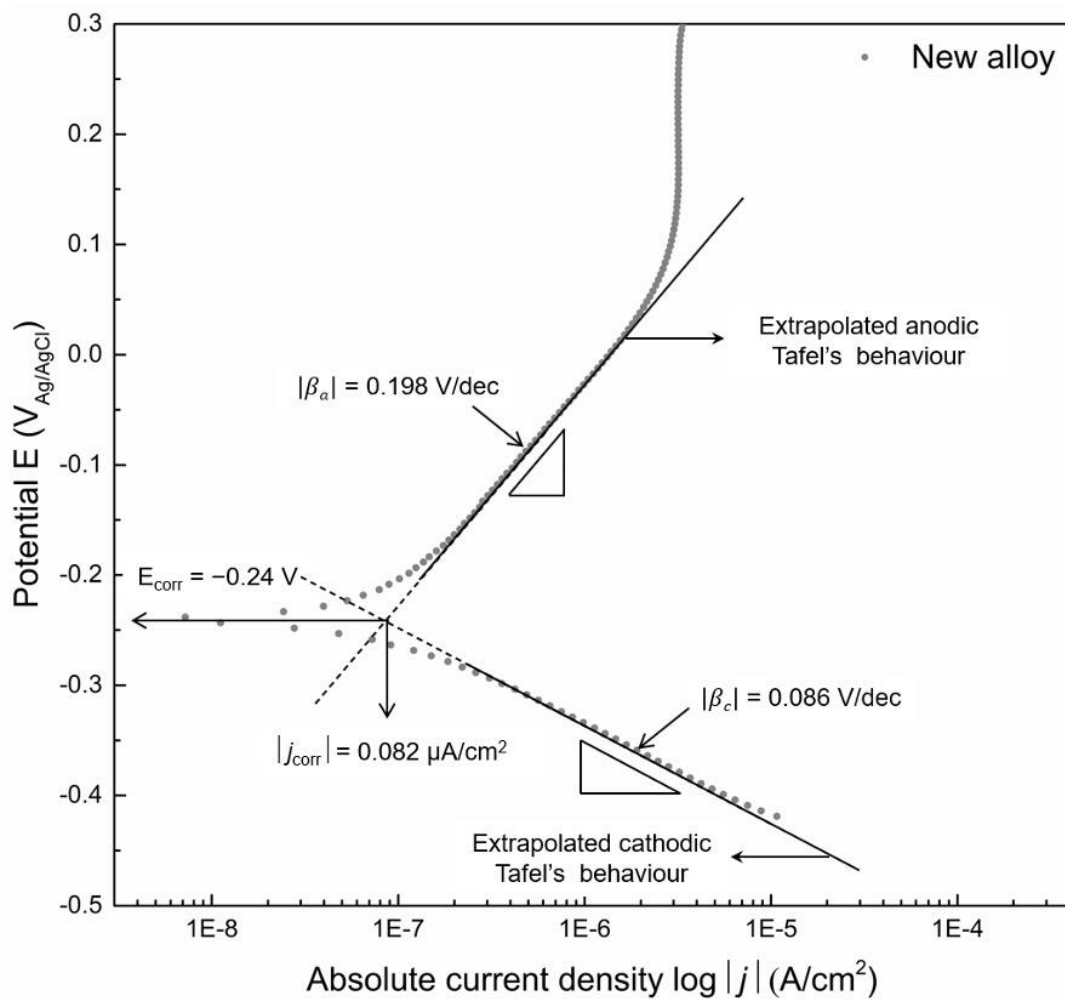
Figure 2-11 Representative example of fitting parameters by using Tafel's extrapolation method in potentiodynamic polarisation curve

Figure 2-11 shows the extrapolation fitting j_{corr} for evaluating the corrosion rate from the potentiodynamic polarisation curve. Thereby, the corrosion rate (r), in the unit of mm/y, from the Faraday's law can be expressed as

$$r = 0.00327(aj_{corr}/\delta D)$$ Equation 2-5

where a is the atomic weight, δ is the number of electrons transferred or the oxidation number changed during the reaction and D is the atomic density. In this case, the corrosion rate is 0.001 mm/year when the j_{corr} obtained by the Tafel's fitting is 0.082 μA/cm^2.

2.2.2   Impedance method

The alternating current (AC) technique or EIS assessment provides various the interfacial process information that can be further analysed and/or determined such as the kinetics of the chemical reaction, resistances, and capacitances in the complex electrochemical processes [67].

Usually, the impedance measurements produce the simultaneous two types of graphs, expressed in the Nyquist plot (real impedance Z' and imaginary impedance -Z") and the Bode modulus |Z|/phase angle θ as a function of frequency f. The record signal usually helps in deciding whether the experiments are proceeding correctly and in making a first assessment of data. Both types of plots be used, especially when comparing experimental data with the fit to the equivalent electrochemical circuit (EEC).

According to the previously equilibrium state obtained by open circuit measurement, we assumed the passive film was formed on the metal surface when it immersed in aqueous (see Figure 2-10). For simplify an EEC explanation correlated with the passive film stability, Figure 2-12 displays an inserted $R_S(R_PC_{dl})$ circuit, representing of a simple corroding surface under activation control [63]. The circuit consists of a parallel circuit connected in series with the solution resistance (R_S). The parallel circuit comprises a polarisation resistance (R_p) and the double layer capacitance (C_{dl}) at the metal/passive film interface. The EEC has been performed to interpret and characterise the behaviour of passive film, regarding to the impedance results. The AC impedance of double layer capacitance (C_{dl}) and polarisation resistance elements (R_p) are

$$Z_c = \frac{1}{j\omega C_{dl}}$$

<div align="right">Equation 2-6</div>

$$Z_R = R_p$$

<div align="right">Equation 2-7</div>

where $j^2 = -1$ is the imaginary number and ω is the angular frequency in (rad/s). Hence, the total impedance of the system (see Figure 2-12) can be expressed as

$$Z_{tot} = R_s + \cfrac{1}{\cfrac{1}{R_p} + j\omega C_{dl}} = R_s + \cfrac{R_p}{1 + j\omega R_p C_{dl}}$$

Equation 2-8
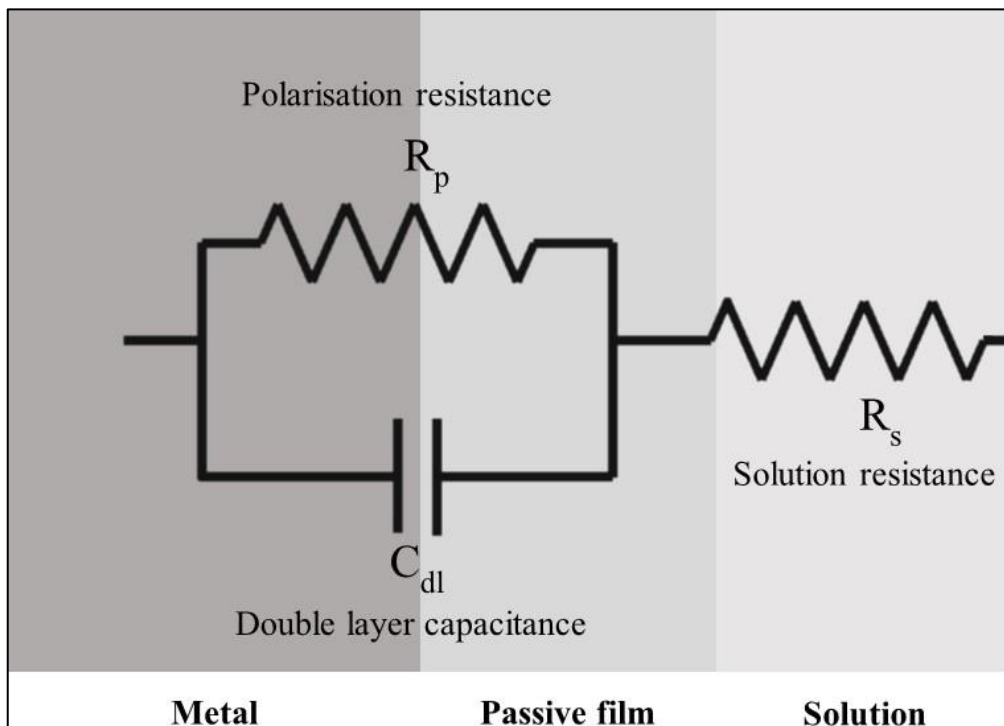
Figure 2-12 Schematic model of the metal/passive film interface with the $R_s(R_{ct}C_{dl})$ EEC

Figure 2-13 shows the complex plane impedance (a) and Bode plot (b and c, respectively), fitted by the $R_s(R_{ct}C_{dl})$ EEC. The Nyquist plot shows a semicircle, with lowering frequency in a clockwise direction. At high frequency domain, the imaginary impedance *-Z"* displayed only the solution resistance (R_s). In the other hand, the low frequency domain, the *-Z"* showed the polarisation resistance (R_p). In the Bode curves, at the immediate frequency domain, the double layer capacitance plotted a linear with a slope and a maximum phase angle.

In the corrosion system, the interpretation of R_p value provides the corrosion susceptibility in the alloy. In other word to say that the lower corrosion rate is correlated with the larger polarisation resistance.

There were many cases when the maximum phase angle lower than 90° in the Bode phase, it can be said that the property of passive film acts as in-ideal capacitive characteristic. It may be due to the fact that, the different factors at film/solution interface leading to the distribution of the relaxation times, therefore, the constant phase element (Q_{CPE}) can be employed instead of an ideal double layer capacitance element (C_{dl}). The Q_{CPE} represents the constant phase element impedance (Z_{CPE}) at the interfacial of film/solution resistance. The behaviour of Q_{CPE} is generally attributed to distributed surface reactivity, surface inhomogeneity, roughness, electrode porosity, etc. [68-70]. The impedance of this element is defined as

$$Z_{CPE} = \left[Q_{CPE}(j\omega)^\alpha \right]^{-1} \qquad\qquad \text{Equation 2-9}$$

where the coefficient Q is the constant phase element parameters in $F \cdot cm^{-2} \cdot s^{\alpha-1}$ and α is the constant phase element component, indicating the circuit parameter with limiting behaviour.
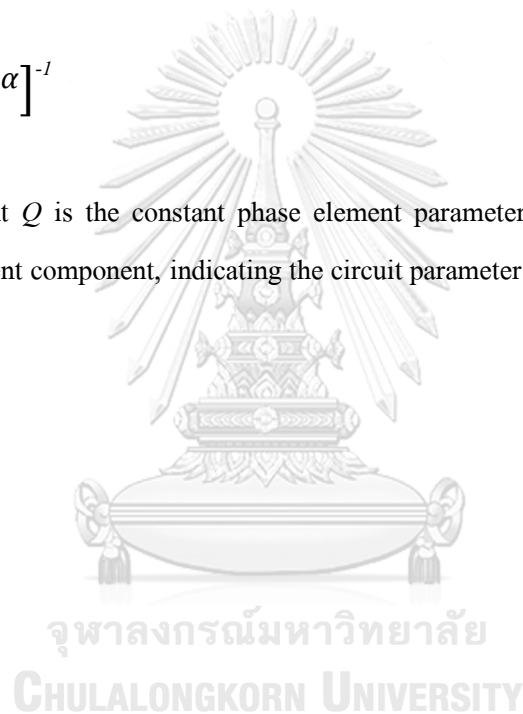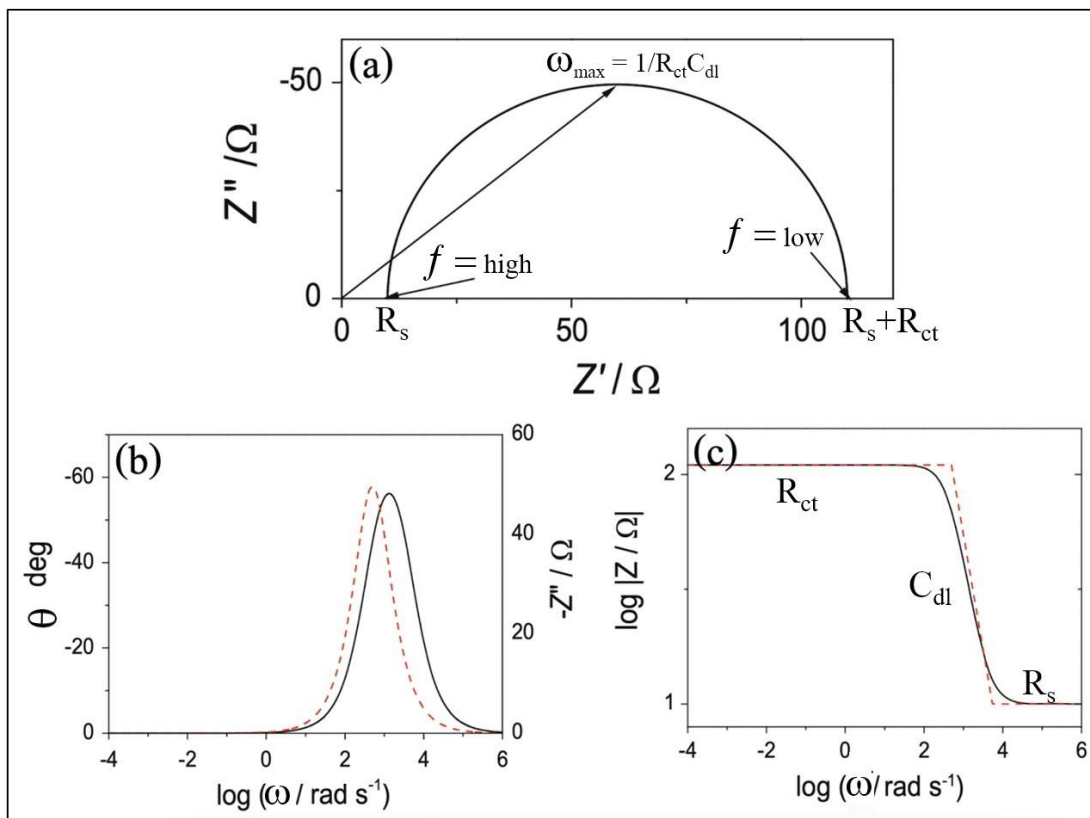
Figure 2-13 Signal record for EIS measurement (a) Nyquist plot, (b) Bode phase and (c) Bode magnitude for a corroding electrode simulated by $R_s(R_pC_{dl})$ EEC, R_s = 10 Ω, R_{ct} = 100 Ω, C_{dl} = 20 μF. The red lines represent the fitting curve result [67].

2.2.3 Capacitive measurement or Mott-Schottky (M-S) analysis
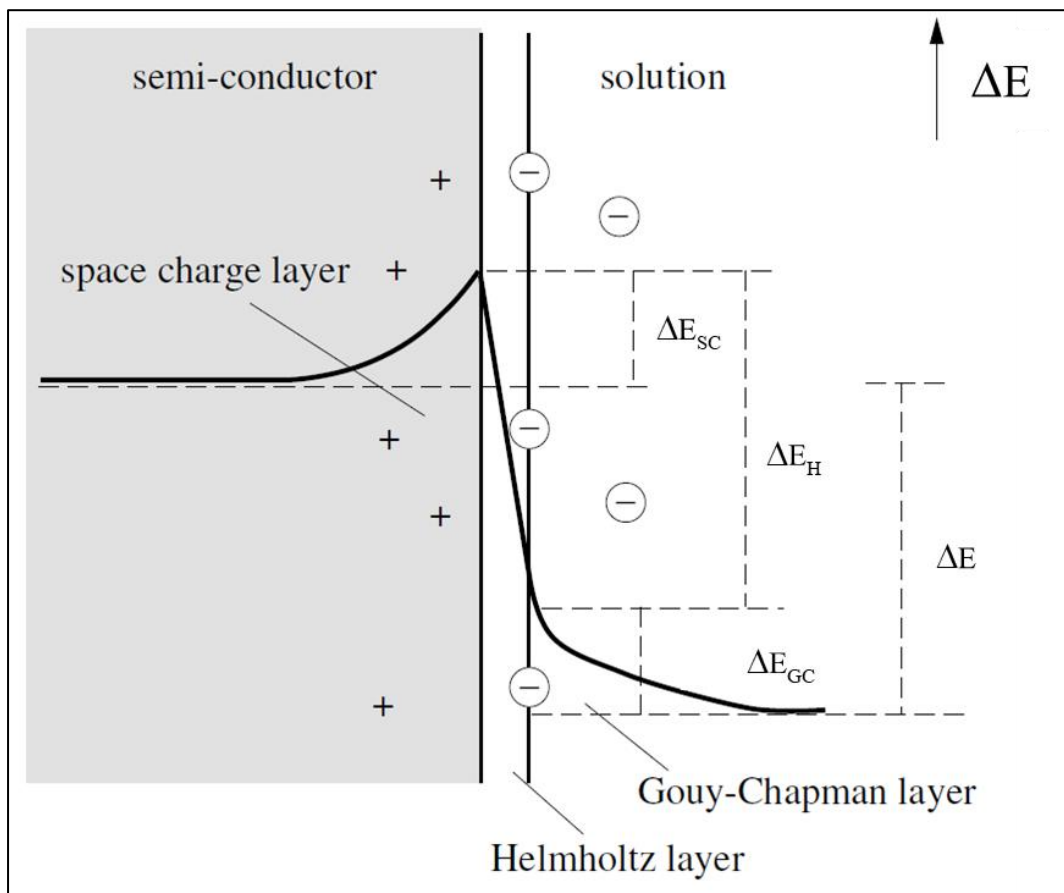
Figure 2-14 Double layer at semiconductor-electrolyte interface [62]

Figure 2-14 shows the potential different layer (Space Charge layer ΔE_{SC}, Helmholtz layer ΔE_H, Gouy-Chapman layer ΔE_{GC}) at the semiconductor-electrolyte interface. The sum of three terms can be written as

$$\Delta E = \Delta E_{SC} + \Delta E_H + \Delta E_{GC} \qquad \text{Equation 2-10}$$

Semiconducting characteristics of the passive film can be explored by measuring the capacitance at metal/film/solution interfacial layer as a function of the applied electrode potential. The surface states contribution of passive layer for the total capacity of the double layer provides the relationship become (Equation 2.11):

$$\frac{1}{C^2} = \frac{1}{C_{sc}^2} + \frac{1}{C_H^2} + \frac{1}{C_{GC}^2} \qquad\qquad \text{Equation 2-11}$$

Where C_{sc}^2, C_H^2, and C_{GC}^2 are the Space Charge capacitance, Helmholtz capacitance and Gouy-Chapman capacitance, respectively. The capacitance of the space charge layer is exceedingly small compared with the other ones, so the measured interfacial capacitance can be regarded as that of the space charge layer when the potentials are applied with sufficiently high frequency [12, 62].

The defects and electrical property in semiconducting of the passive film can be explained in the fundamental of Mott-Schottky (M-S) theory. The M-S explanation provides the correlation between the square of reciprocal space charge capacitance, and applied potential can be written as the Equation (2.12):

$$\frac{1}{C^2} = \frac{1}{C_{sc}^2} = \pm \left(\frac{2}{\varepsilon\varepsilon_0 e N_q}\right)\left(E + E_{fb} + \frac{kT}{e}\right) \qquad\qquad \text{Equation 2-12}$$

where ε is the dielectric constant of the passive film, ε_0 is the vacuum permittivity (8.8542×10^{-14} F·cm^{-1}), e is the electron charges (1.602×10^{-19} C), E_{fb} is the flat band potential, k is the Boltzmann constant (1.3807×10^{-23} J·K^{-1}) and T is the absolute temperature. N_q is the number of defects-type density in passive film. E is potential applied. Besides, the term of $kT/e = 0.025$ V is negligible since relatively small enough at room temperature [71]. As the dielectric constant of a material is dependent on its chemical composition, passive layers with different chemical composition will have different dielectric constant. However, determining the exact dielectric constant for a thin layer is not trivial. Hence, the dielectric constant in this work is assumed as 15.6 [16].

According to the passive state of Fe-Cr alloys, the thin film is likely bi-layer structure which are oxide inner layer and hydroxide outer layer when it immersed in aqueous. Figure 2-15 shows the different capacitive behaviour, namely Mott-Schottky plot, of passive layer formed on 2507 SDSS surface in 3.5 wt.-% NaCl [72]. In this sense, the values of density of defects (N_q) within

the passive films can be calculated from the positive and/or negative slope of the linear zones in M-S plot, which the positive slope represents the n-type semiconductor or donor density (N_D) and, on the other hand, the negative slope represents the p-type semiconductor or acceptor density (N_A). The intersection of the linear segments on both p-type and n-type semiconductor can determine the E_{fb} at the abscissa for $C^{-2} = 0$.

Figure 2-15 reveal the presence of two regions. In the anodic region (E >0.5 V_{SCE}) the capacitance represents the electrochemical behaviour of a n-type semiconductor. On the other hand, in the more cathodic region (E <-0.5 V_{SCE}), the capacitance describes the behaviour of a p-type semiconductor. Note that, the E_{fb} is -0.5 V_{SCE}. The decrease of the N_D (n-type) in the external layer, when lower immersion time, leads to a thickening of the space charge region and could therefore be responsible for the raise of the corrosion susceptibility.
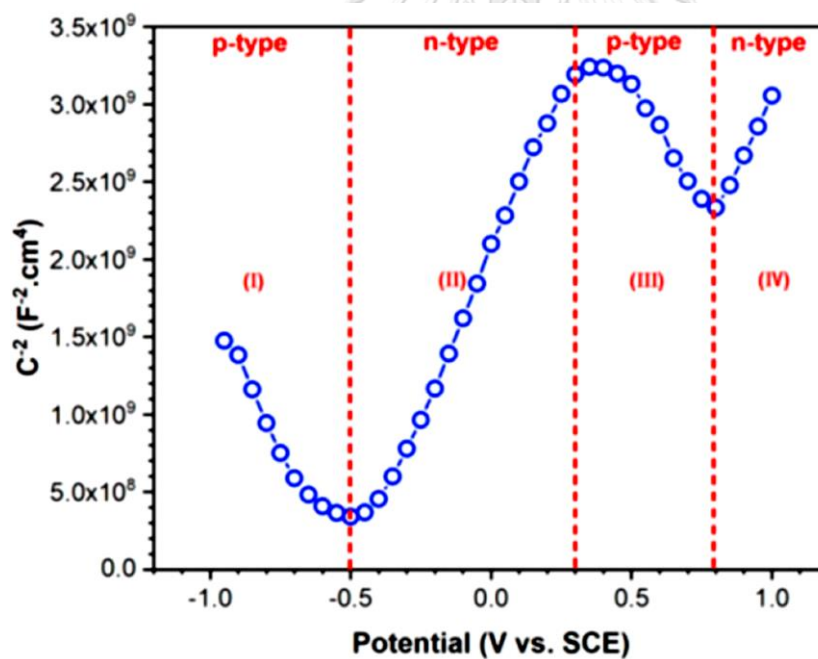
Figure 2-15 Mott-Schottky analysis of super DSS sample in the 3.5% NaCl corrosive solution [72]

2.2.4 Point defect model by Digby D Macdonald [19]

Digby D Macdonald postulated the properties of passive state of metal and alloys on the surface substrate in aqueous solution under equilibrium state, namely the point defect model (PDM). Figure 2-16 illustrates the proposed physicochemical process of point defect model. Those defects accumulate at the interface and finally lead to a local accumulation if they penetrate the metal phase at a slower rate than their transport through the film. This situation leads to accumulating the stress within the passive film and its subsequent breakdown, as shown in Figure 2-17. The model informs of the defect generation by Reactions (1) and (4) and annihilation by Reactions (2) and (3) of oxygen (anion) vacancy $V_O^{\bullet\bullet}$ and cation vacancy $V_M^{\chi'}$ at metal/film and film/solution interfaces, respectively. Here is the Kroger-Vink notation is used for the representative of virtually double-positive charge ($^{\bullet\bullet}$) and negatively charge ($^{\chi'}$) in those vacancies.
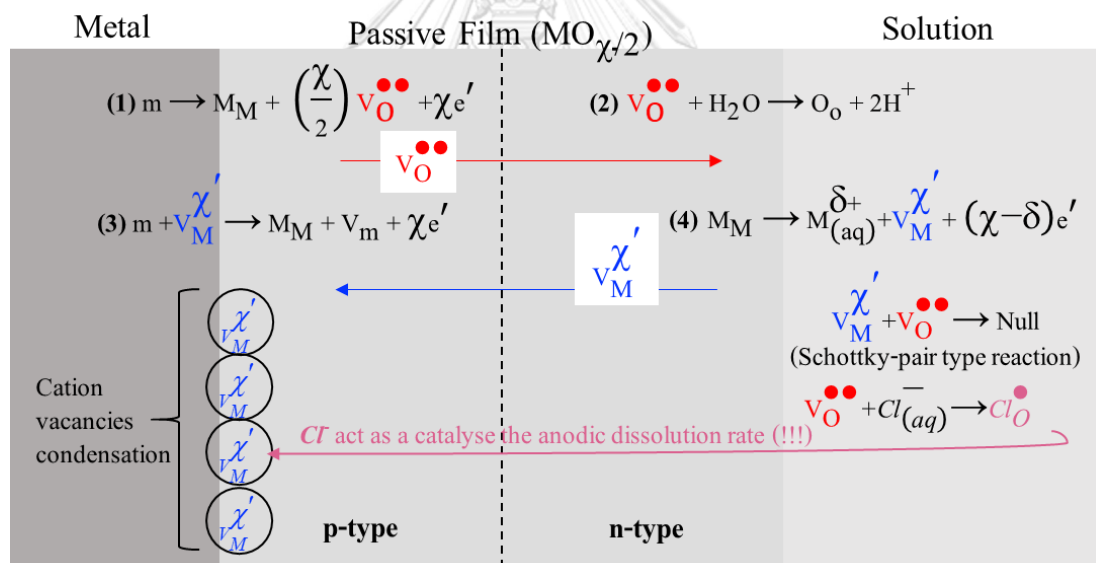
Figure 2-16 The proposed physicochemical processes of point defect model (PDM) by Macdonald [19]

The m is a metal atom, $M_{(aq)}^{\delta+}$ is the cation in film/solution interface, M_M is cation in cation site on the cation sub-lattice, O_O is oxide ion in anion site on the anion sub-lattice, $MO_{\chi/2}$ is stoichiometric barrier layer oxide. Note that, the PDM assumed that the $V_M^{\chi'}$ migrate from the film/solution to metal/film interfaces, and this is equivalent to the transport of cation in the opposite direction. Theoretically, the predominant dopant defect in the p-type semiconductor is

cation vacancies $V_M^{\chi'}$ (acceptor species) and n-type semiconductor are oxygen vacancy $V_O^{\bullet\bullet}$ (donor or carrier species). Consequently, the PDM perspective considers the migration of point defects (vacancies) and the influence of concentration gradients within the passive film under steady-state condition.
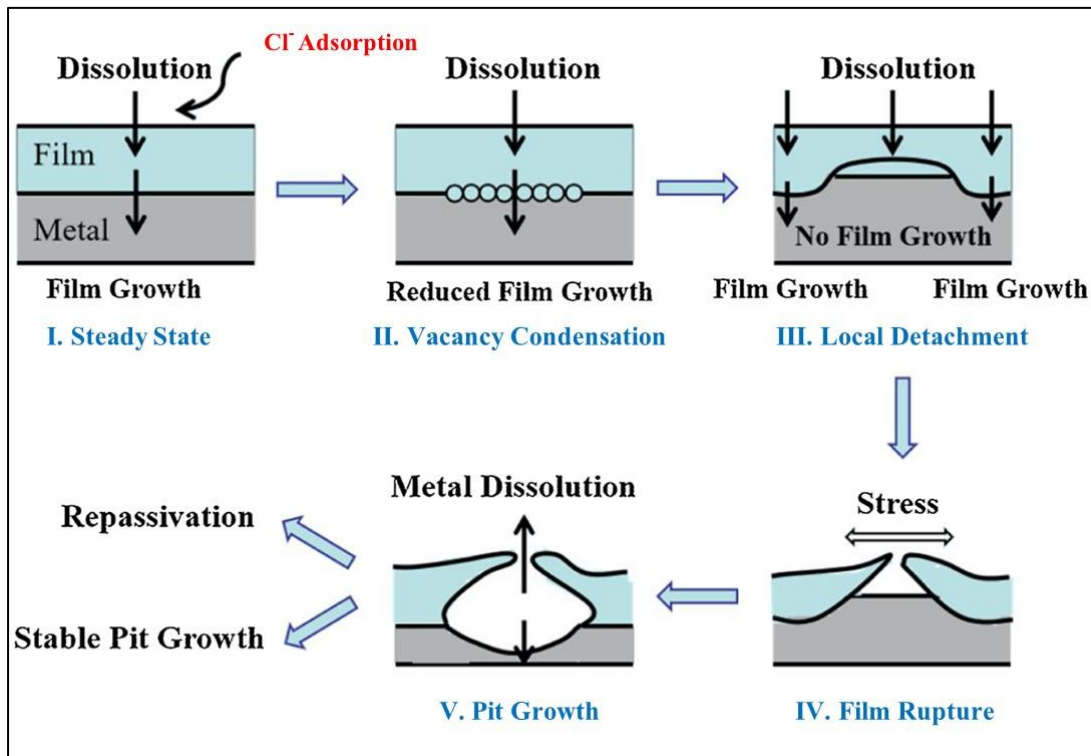
Figure 2-17 Stages of pit nucleation according to the Point Defect Model [19]

Figure 2-17 shows the ordering stages of pit nucleation in accordance with the Point Defect Model. Assuming the metal (such as Fe-Cr alloys) immersed in the chloride media in a period of time (likely E_{ocp} measurement), the metal formed the passive layer then reached to the steady-state condition. To analysis the passivity breakdown phenomena in the Fe-based metal system in terms of PDM, it is generally accepted that the anion species (e.g., chloride ions Cl^-) act as a catalyse the anodic dissolution rate, this is to say the chloride ion is adsorbed at the film/solution interface into the surface oxygen vacancy (**Stage I**), which may be expressed as
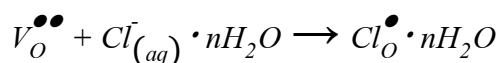
$$V_O^{\bullet\bullet} + Cl^-_{(aq)} \cdot nH_2O \longrightarrow Cl_O^{\bullet} \cdot nH_2O \qquad\qquad \text{Equation 2-13}$$

However, the Reaction (D) is simultaneous occurred and inhibited by the Reaction (2.13) at the film/solution interface, since the Cl^- ion competes with the oxide anion (O^{2-}) for the occupation of the oxygen vacancy $V_O^{\bullet\bullet}$. Since the metal responds to the loss of oxygen vacancy by generating cation vacancy Reaction (C) and oxygen vacancy Reaction (B) via Schottky-pair type of reaction (Reaction 2.14), which can be written as follows

$$V_M^{\chi'} + V_O^{\bullet\bullet} \longrightarrow Null \qquad\qquad \text{Equation 2-14}$$
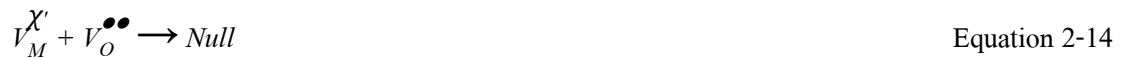
Since the $V_O^{\bullet\bullet}$ reacts with the addition anion, see Reaction 2.13, the cation vacancy is more generate at the film/solution interface and, thereby, the annihilation reaction (Reaction A) is incapable of consuming the cation vacancy arriving at the metal/film interface, resulting in the excess vacancies will condense (**Stage II**) and lead to the local detachment of the film from the underlying of metal (**Stage III**) because of the presence of tensile stresses in the film coupled with the film dissolution (**Stage IV**). Finally, the Cl^- directly contacted with the metal surface and thereby generated the dissolution process became to the pit nucleation (**Stage V**).

2.3   Effects of thiosulfate on pitting susceptibility in duplex stainless steels

Most of desalination plants or oil/gas pipeline system often operate in contact with chloride- and hydrogen sulfide (H_2S) media. Because H_2S is the essential constituent of sour gas environments, brines saturated with H_2S have been used traditionally to investigate the sour gas resistance of materials. They concerned how the employed materials must resist to pitting corrosion and stress-corrosion cracking (SSC) in these environments. The H_2S is one of the most toxic, flammable, and corrosive substances, thereby, the researchers are prevented from conducting SCC tests in sour environment. Particularly, this work focused on its pitting susceptibility in acidified artificial sea water (ASW) containing thiosulfate ions ($S_2O_3^{2-}$), while minimizing the health hazards during laboratory tests and reducing the cost of equipment required to operate under safety condition. The approach to add the $S_2O_3^{2-}$ instead of H_2S gas in acid salt solutions in order to simulate the aggressiveness of sour well environments, which is acceptable [73].
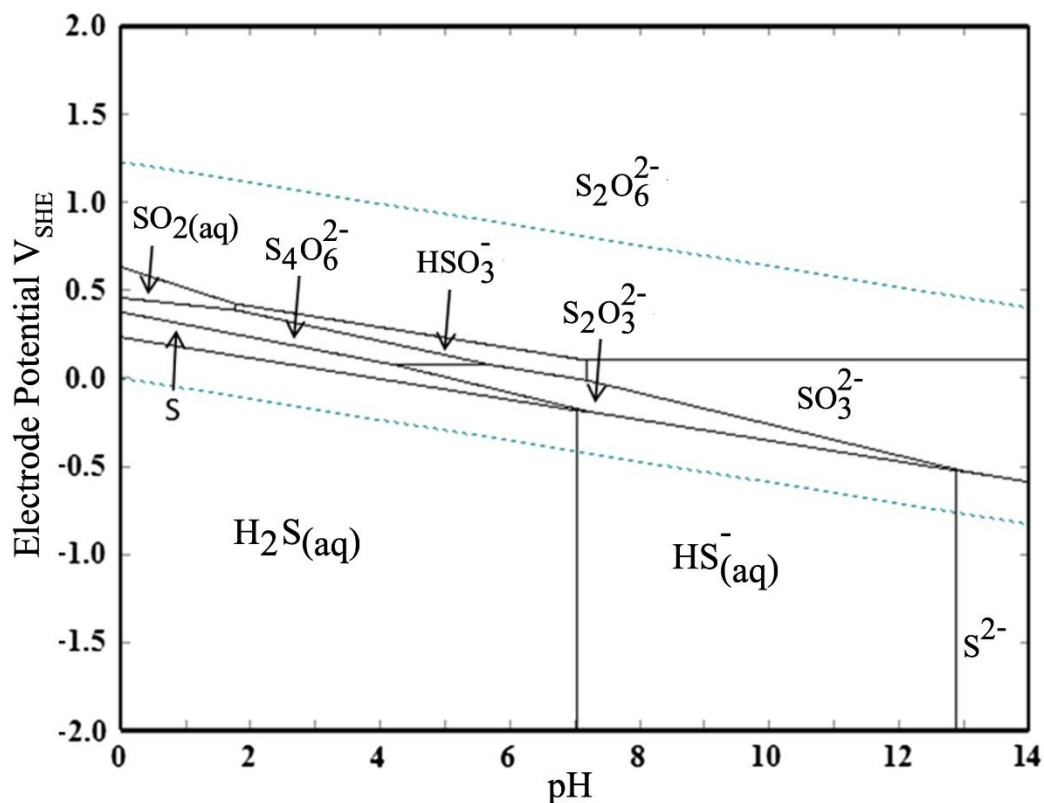
Figure 2-18 E-pH (Pourbaix) diagram for the S-H_2O system at 25 $^\circ$C [6]. The thermodynamically stable sulfates are omitted for clarity in displaying the metastable species domains. Dissolved sulfur species activity = 0.001.

The emphasis in the section literature is on thiosulfate, it is important to note that $S_2O_3^{2-}$ is only one of polysulphur oxyanions that exist in the $S\text{-}H_2O$ system, depending upon the pH and redox potential of the environment (see Figure 2-18). In other word to say, the thiosulfate ion is thermodynamically metastable. It dissociates to form elemental sulphur by the following reaction as shown in Equation 2-15, which must be considered when the solution pH is less than 5 [73]. However, in the Pourbaix diagram as shown in Figure 2-18, thiosulfate ion will transform to H_2S when pH and potentials are in between 5 to 7 and -2.0 to 0 V_{SHE}, respectively.

$$S_2O_3^{2-} + 6H^+ + 4e^- \longrightarrow 2S + 3H_2O \qquad \text{Equation 2-15}$$

Then, the elemental sulfur produced by the above reaction can be reduced (Equation 2.16) or disproportionated (Equation 2.17) to yield H_2S [6]. Therefore, the artificial seawater containing thiosulfate ions can be used as chloride- and hydrogen sulfide (H_2S) media.

$$2S + 2H^+ + 2e^- \longrightarrow H_2S \qquad \text{Equation 2-16}$$
$$4S + 4H_2O \longrightarrow 3H_2S + HSO_4^- + H^+ \qquad \text{Equation 2-17}$$

Many papers deal with the thiosulfate-containing in chloride media of lean duplex [14,17,74−75], standard duplex, and super duplex stainless steels [12,16,76,78−79]. Federaica Zanotto et al. [74] compared the SCC resistance of two lean DSSs (DSS 2304 and LDSS 2404) by slow strain rate test (SSRT) in the presence of chloride and thiosulfate media. They found that the high SCC resistance of DSS 2404 was connected to its high Mo content, while the significant SCC susceptibility of LDSS 2101 in NACE TM-0177 solution was likely due to the high Mn content of the alloy. Yushu Wang et al. [14] studied the metastable pitting behaviour of AISI 304L ASS and LDX 2101® and found that, increasing thiosulfate concentration resulting increasing peak currents for the metastable pitting and promoted the growth of metastable pitting events with shorter growth time and faster pit growth kinetics on 304L. The preferential pit initiation was found on the ferrite phase for lean duplex alloy. F. Zanotto et al. [75] also pointed out the selective corrosion of the ferrite phase became the main cause of failure when the thiosulfate concentration was increased to 0.1 M. Moreover, the work of Liang He et al. [17]

proved the ferrite phase is more susceptibility to localised corrosion than austenite phase in thiosulfate-containing environment of the lean duplex grade (DSS 2304). Consequently, the synergistic effects of chloride and thiosulfate enhanced the passive breakdown phenomena and made it easier for Cl^- to initiate pitting by reducing to hydrogen sulphide which catalysed the anodic dissolution on the ferrite phase.

Considering for the standard and super duplex grade, Jiantao Zhang et al. [76-78] exhibited the enhancing of dissolution rate in ferrite phase and thinner of passive film when higher applied anodic potential in DSS 2205. They showed the degradation of passive state in EIS and M-S analysis when the potential above 0.2 V_{SCE}. H.Luo et al. [12] investigated the bi-layer structure of passive film (n-type and p-type) obtained by capacitive measurement in DSS 2205. Their XPS results showed the iron oxides in the passive film changed into $FeOOH$, FeO when the applied potential above 0.6 V_{SCE}. Maysam Mohammadi et al. [79] showed the E_{OCP} curves of DSS 2205 from 1-120 hr, immersed in thiosulfate electrolyte and displayed the more accurately predicted thickness of passive layer by the power-law model. Zhongyu Cui et al. [16] revealed the passivation behaviours and surface chemistry of SDSS 2507. They showed only n-type semi-conductivity exhibiting in the passive film and was independent of the thiosulfate levels. Their XPS results confirmed thiosulfate promoted the formation of Fe(II) in the pre-passive region and accelerated the transformation of Cr(III) to Cr(VI) in the transpassive region. Accordingly, the duplex stainless steels may suffer sulphur-induced degradation in the local acidified environment in seawater.

From the studied literatures, there have not been appeared the study of high Mn-N DSS in the thiosulfate-containing chloride solution.

CHAPTER 3

EXPERIMENTAL PROCEDURES

This chapter presents the new duplex stainless steel processing starting from sample preparation in vacuum arc re-melting (VAR) furnace, heat-treatment, and characterisations. The characterisation techniques consist of chemical composition analysis by OES and Nitrogen analyser, phase composition analysis by EPMA, phase identification by XRD and pit investigation by SEM. Corrosion behaviours of the new duplex, and standard duplex stainless steel (2205 DSS) are studied by potentiodynamic and potentiostatic polarisation methods, Electrochemical Impedance Spectroscopy (EIS) and Mott-Schottky (M-S) analysis.

3.1   Sample preparations and heat-treatment

3.1.1   Supplies, Equipment and Accessories

Table 3-1 Chemical compositions (wt.-%) of the thin pieces of AISI 316L and AISI 430.

Materials	C	Si	Mn	Cr	Ni	Mo	Cu	Al	Fe
316L	0.017	0.589	1.061	16.590	10.470	2.030	0.260	0.003	Bal.
430	0.054	0.194	0.742	16.325	0.101	0.004	0.023	0.097	Bal.

- Raw elemental substances: 99.9% pure chromium (Cr) flake and 99.5% pure manganese (Mn) flake, obtained by Alfa Aesar (see certification analysis in appendix).

- The polished thin pieces of AISI 316L austenitic, and AISI 430 ferritic stainless steels with about 4-cm^2 area and 0.4-mm thickness, contributed by the Posco Thainox Co., Ltd. Their chemical compositions are listed in Table 3-1.

- Vacuum single arc melting furnace (model SA-200 MRF) with a vacuum pump system, see Figure 3-1.

- Replaceable 2% Thoriated W electrode $\varnothing$ 2.4 mm rod

- An analytical balance

- High purity mixed 90%Ar + 10%N$_2$ shielding gas, obtained by Linde (Thailand) PLC.

- Cu heart mould

– Vertical tube furnace for heat-treatment, see Figure 3-3

Figure 3-1 Vacuum single arc melting furnace (model SA-200 MRF) with pressure guage

3.1.2   Casting operation steps via vacuum arc re-melting (VAR) equipment

I. Starting from the chemical composition of 28.5Cr-9Ni DSS [4, 5, 80], the new chemical composition of DSS was designed by decreasing Cr and Ni contents and adding N from Ar+N_2 shielding gas and Mn to the new alloy. The decrease of Cr content is expected to reduce corrosion resistance of alloy, but it will compensate by the increase of N content.

II. Weigh all of charge materials as pure Cr and Mn flakes, AISI 430, and AISI 316L pieces using analytical balance. Total charged materials do not exceed 5 grams per charge for melting and casting.

III. Locate the thoriated tungsten electrode in furnace to appropriate position for melting.

IV. Load all combined charge materials into a copper heart mould in the VAR furnace as shown in Figure 3-2. Before the operation, check the drain system and assure the copper heart mould. They must be securely fastened to the base with three clamps beneath the furnace base. All gas lines correctly purge to the chamber.

V. Decrease of air/oxygen partial pressure in furnace atmosphere by feeding the Ar+N_2 shielding gas into the chamber at 0.3 bar at the flow rate of 5 L/min [23]. Check the operating pressure at the pressure gauge. Close the gas release valve. Switch on the vacuum pump and allow the pump to run for 20 seconds, then the pressure in the chamber will rapidly decrease.

VI. Repeat the previous procedure at least five times to ensure that all air/oxygen is completely enough removed from the chamber.

VII. Prepare the arc into charged materials after the vacuum procedure finish, then turn on the welder power supply and adjust the current to 100 A on the welder front control panel.

VIII. Move the electrode towards the charged material pieces. Switch on the arc to begin by foot control. When the arc start, move the arc over the charged material to melt. At the same time, look after inside the furnace through the welding grey glass. Allow the water and inert gas to flow until the furnace is cooled down completely.

IX. When the charged material is melted completely, remove foot from foot control to stop the arc and remove the stinger rod or the thoriated tungsten electrode from the melt at least one inch.

X.   Switch off the welder power supply and gas, allow the casting specimen and electrode cool down then open the copper heart to bring specimen out.

XI.   Repeat the arc melting process previously at least five times in another side of casting specimen to ensure homogenisation of the melt.

XII.   Take the casting specimen to the hot-forged machine for expanding the surface area with decreasing thickness specimen.
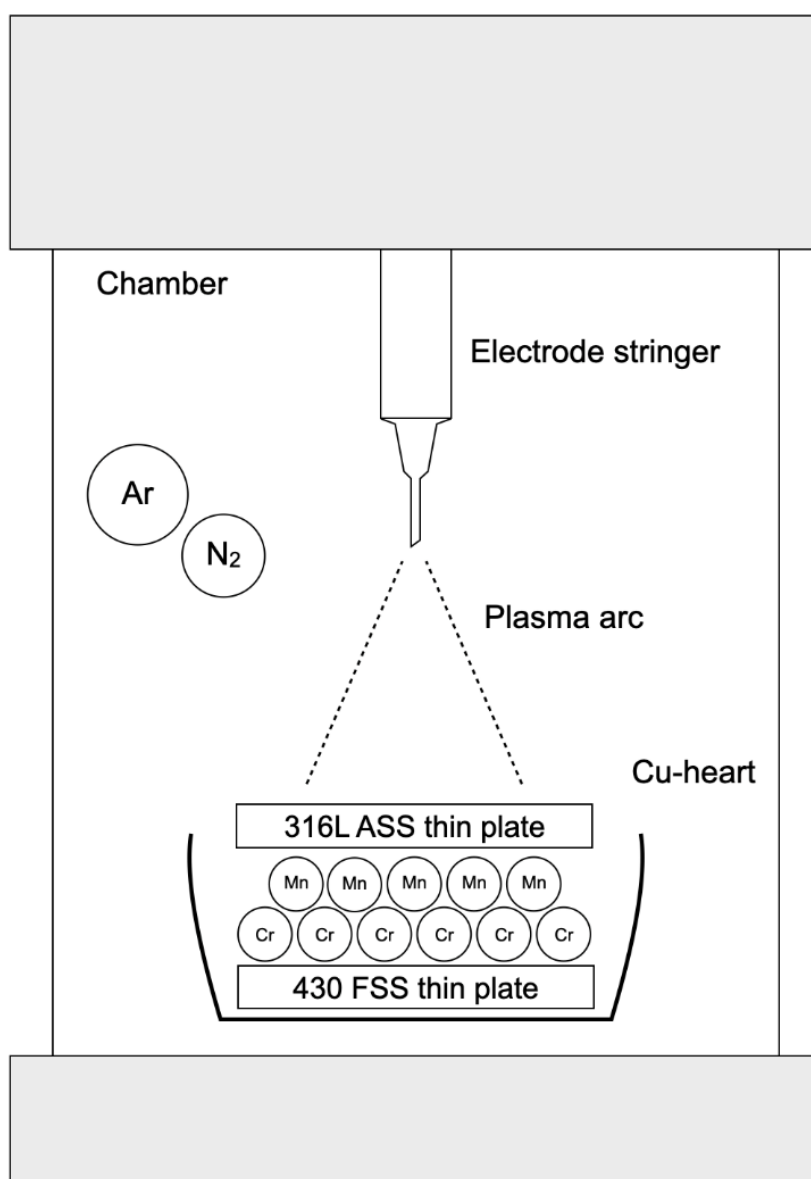
Figure 3-2 Schematic illustration of VAR construction with charging raw

3.1.3   Heat-treatment after Thermo-Calc® simulation

The as-cast samples were deformed by hot-forging process into cylinder shape with diameter of ~24 mm and thickness of ~3-5 mm. Then, the "as-forged" samples were subjected into the vertical tube furnace (see Figure 3-3) for heat-treatment in Argon atmosphere to prevent sample oxidation. The silicon-carbide heaters were used for heating the samples in vertical tube furnace. The temperature of vertical tube furnace was measured and controlled by using the K-type thermocouple and controlled by digital temperature controller. The optimum hot zone of furnace was also calibrated for hanging position of samples. The samples were screw at the edge and hang with the Nichrome wire. After each heat-treatment step, the samples were quenched in water.

Figure 3-3 Establishement of verticle tube furnance

To achieve the duplex microstructure of the new alloy about 50 vol.-% of δ phase, the heat-treatment procedure must be followed the duplex area of phase diagram calculated by Thermo-Calc software as shown in Figure 3-4. The Thermo-Calc database in this work is SGTE solid solution SSLO8. The first stage was solutionised the sample at 1250°C for 1 hr to achieve full ferrite microstructure and quenched in water. The second stage was to keep the ferritised sample at 1050°C for 1.5 hr and quenched in water to achieve about 50 vol.-% of δ phase. After that, the ferrite volume percent of samples were determined by the point counting method according to ASTM E562 described in the Section 3.2.2 [81].
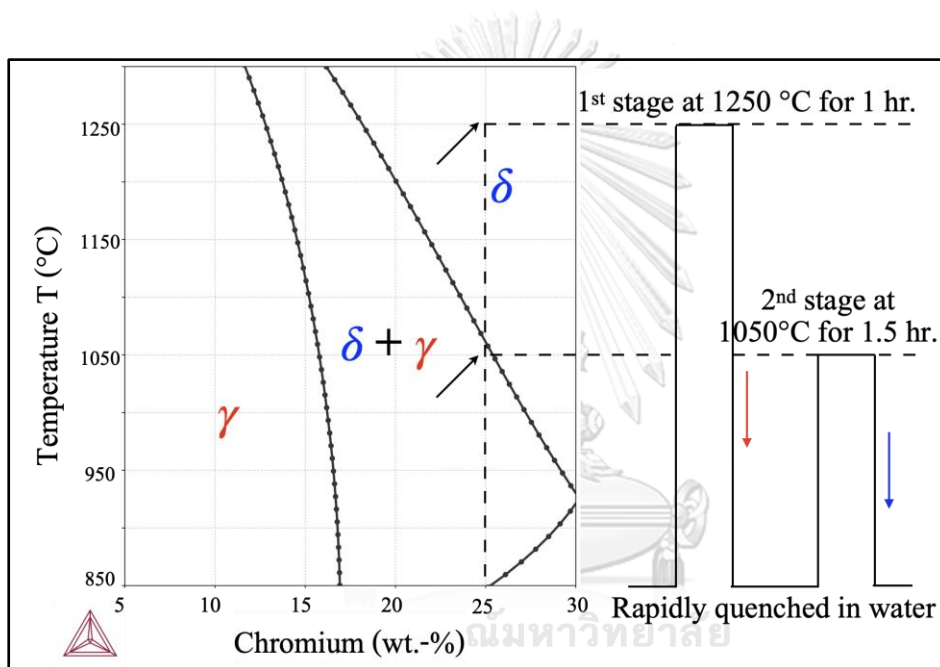
Figure 3-4 Cross-section of the calculated phase diagram of the new duplex sample via Thermo-Calc software (SSLO8 database) and the heat-treatment steps.

3.2 Material characterisations

3.2.1 Spark optical emission spectroscopy (OES) and Nitrogen analysis

The as-forged samples were analysed the nominal chemical composition (wt.-%) using optical emission spectroscopy (Spectrolab LAVM12) and oxygen/nitrogen analyser (EMGA-620W), see Figure 3-5.

Figure 3-5 Optical emission spectroscopy (Spectrolab LAVM12) (left) and oxygen/nitrogen analyzer (EMGA-620W) (right)

3.2.2 Optical microstructure (OM) and volume fraction of phase

All samples were ground by the silicon carbide paper #180 to #2000. Then, they were polished by the polishing cloth using 1-μm and 3-μm diamond abrasive pastes (Struer®). The duplex microstructure was differentiated by the Beraha's etchant [82], which the ferrite matrix phase was dark, but the austenite phase was white. The microstructures were observed under optical microscopy (OM, Canon EOS 350D). The volume fraction of phases was determined by systematic manual point count method following ASTM E562 standard [81] via image analysis Solution DT® commercial software (see Appendix B).

3.2.3   X-ray diffractometer (XRD)

Confirming no formation of the precipitation of intermetallic phases, the X-ray diffraction (XRD) analyser was conducted in D8 Advance diffractometer (Bruker) with Cu Kα radiation (λ = 1.5406 Å) using 0.01 step rate, see Figure 3-6. For the identification of crystallographic phases, the inorganic crystal structure database (ICSD) was used for phase acquisition (01-085-1410 for δ phase and 01-074-552 for γ phase reference numbers).
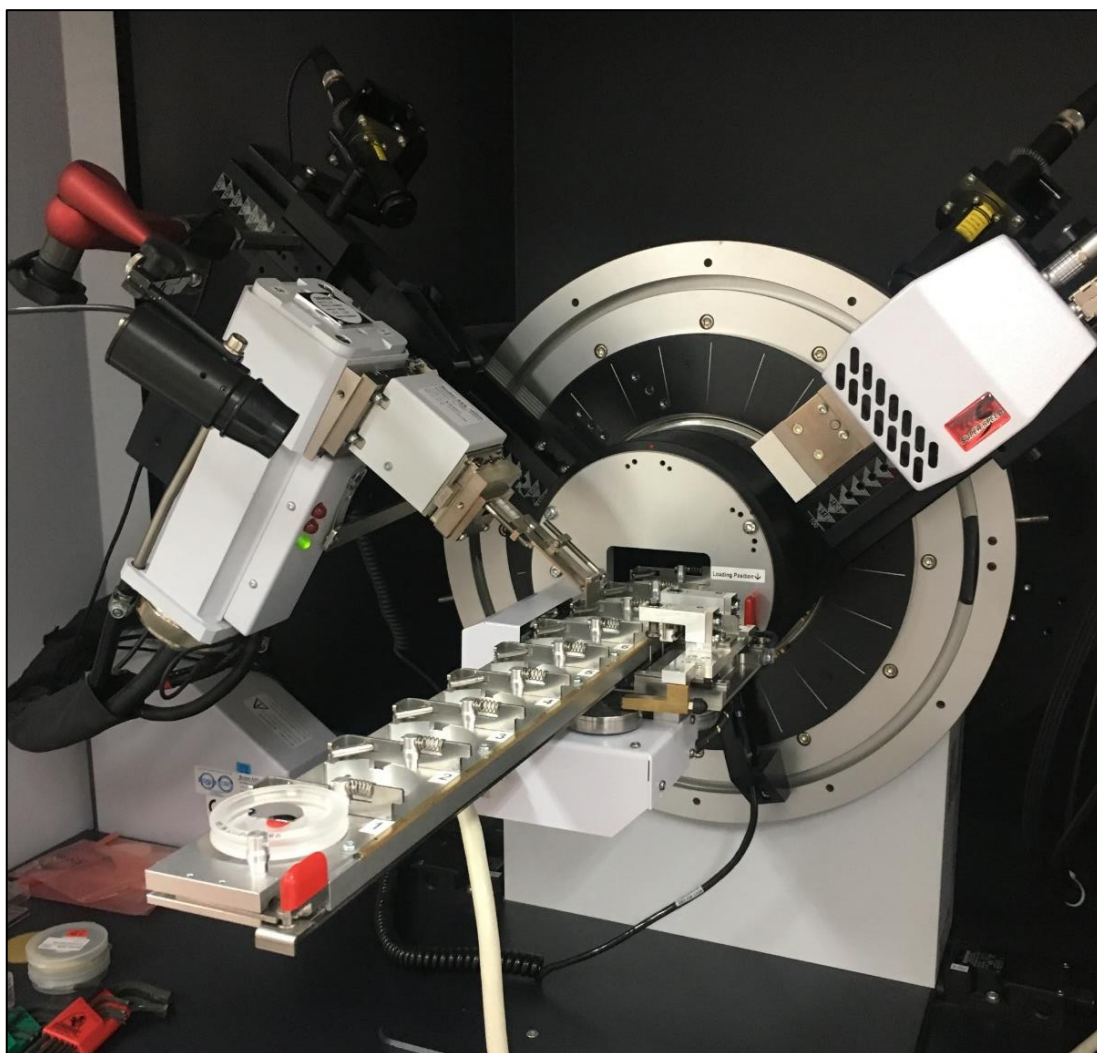
Figure 3-6 D8 Advance diffractometer (Bruker)

3.2.4   Electron probe microanalysis (EPMA)

The electron probe micro-analyser equipped with 5-channel wavelength-dispersive spectrometer (EPMA-WDS-1720, SHIMADZU), was used to analyse the chemical concentration (wt.-%) of alloying element in each phase, see Figure 3-7. In this work, the EPMA used 15 kV bias voltage.
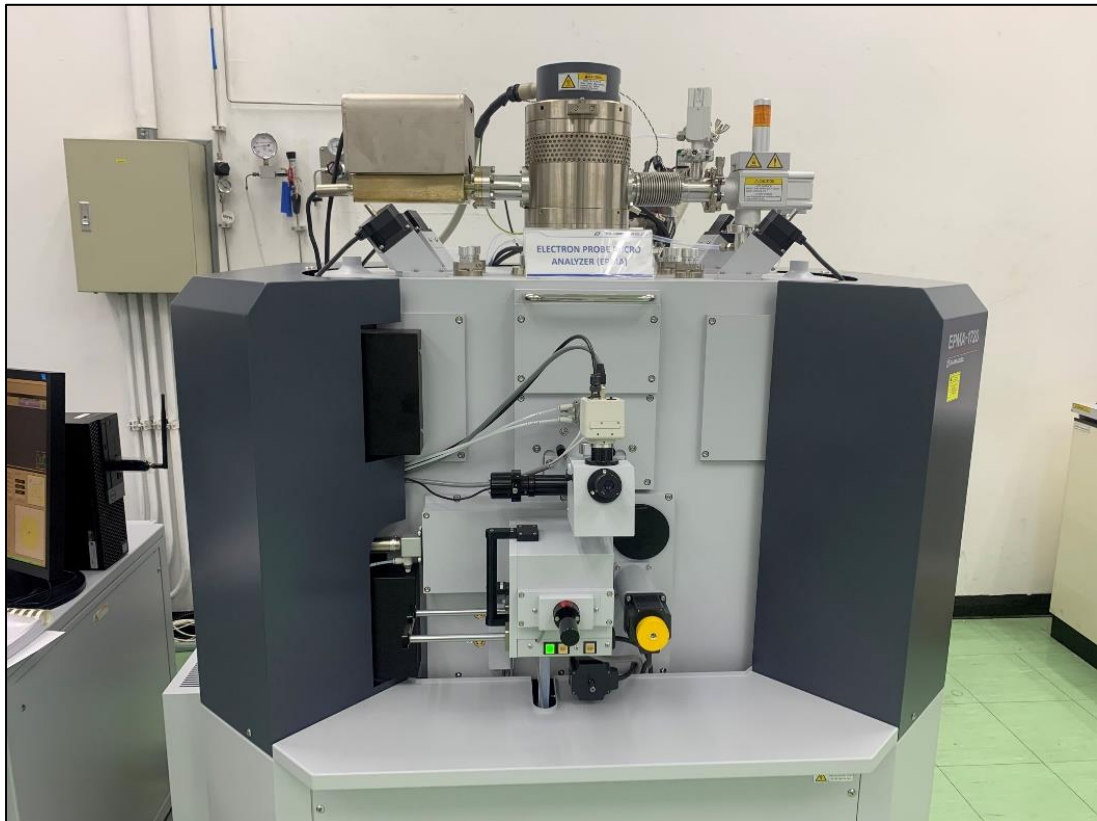
Figure 3-7 The electron probe micro-analyser equipped with 5-channel wavelength-dispersive spectrometer (EPMA-WDS-1720, SHIMADZU)

3.2.5   Scanning electron microscopy (SEM) equipped with energy dispersive spectroscopy (EDS) detector

The chemical composition (wt.-%) in δ and γ phases were examined by EDX detector (point scan). To investigate the selective dissolution of phase or pit attack after the transpassive began, the samples were polished by the polishing cloth using 1‑μm and 3‑μm diamond abrasive pastes (Struer®). Then, the mirror surface sample as the cathode side were electrochemical etched at 2.5 V in the solution of 20% KOH [82]. Pit occurrences were investigated by scanning electron microscopy (SEM, SU3500, HITACHI), see Figure 3-8. In this work, the SEM/EDX used 10 kV bias voltage.
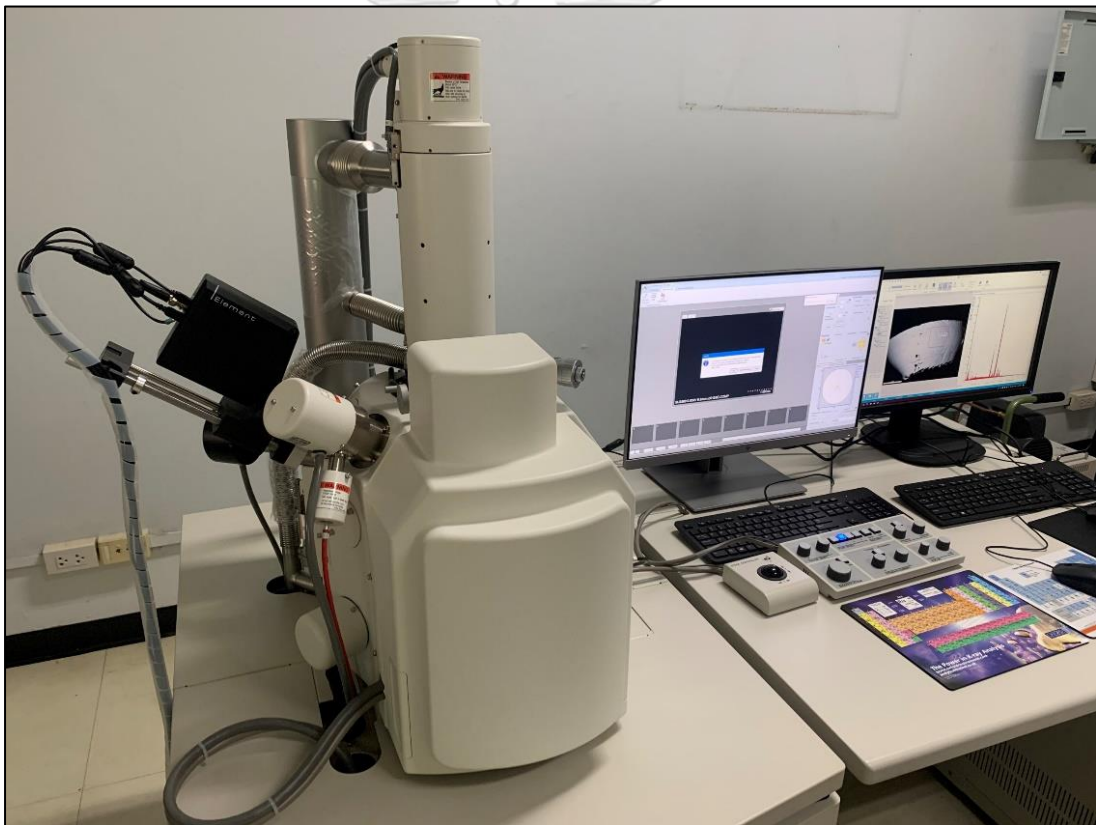
Figure 3‑8 Scanning electron microscopy (SEM, SU3500, HITACHI)

3.3 Electrochemical tests
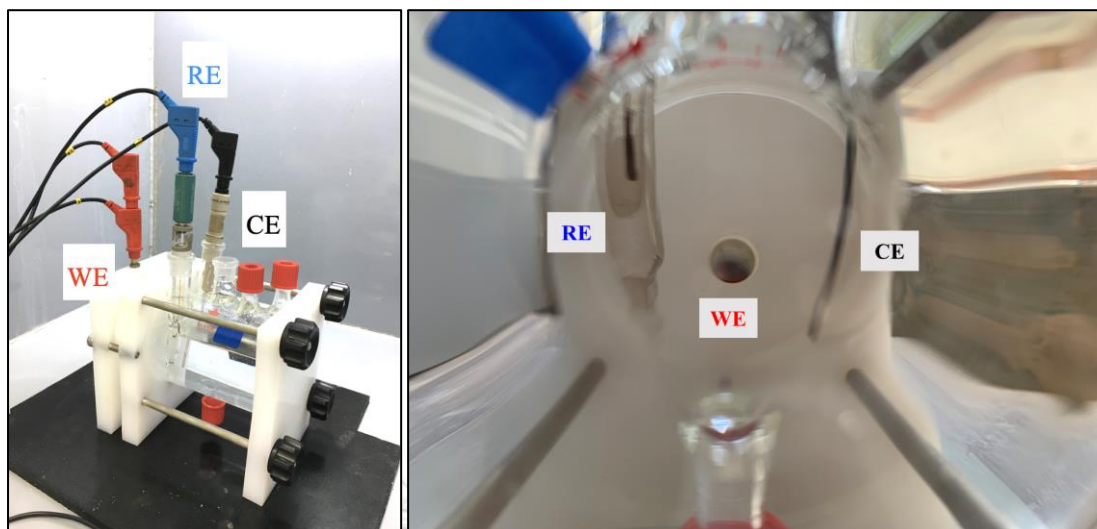
Figure 3-9 The 250-mL electrochemical flat cell set up with three electrodes configuration

The electrochemical tests were carried out in a conventional three-electrode system by using the potentiostat/galvanostat (Autolab PGSTAT 302N, Metrohm) electrochemical workstation. The NOVA version 2.1.4 is the main software to perform the signal record. The counter electrode (CE) was a platinum (Pt) rod, and potentials were measured against the 3-M KCl Ag/AgCl reference electrode (RE). In this work, all potential would be converted from Ag/AgCl to standard hydrogen electrode (SHE) by +0.206 V. The 250-ml electrochemical stationary flat cell were employed (see Figure 3-9). The working electrode (WE) or sample was sealed with the O-ring at the bottom of cell construction. The WE or sample was exposed in the stagnant electrolyte at room temperature. The exposed area was ∼1.15 cm^2. For the validation of electrochemical results, all experiments were triplicated for acceptable reproducibility and good accuracy. The heat-treated samples were progressively wet ground by sandpapers #2000, then well rinsed in distilled water, and degreased with analytical ethanol absolute, blown with hot air and install in the electrochemical cell.

3.3.1 Electrolyte preparations

Table 3-2 shows all five artificial seawaters (ASW) with varying $Na_2S_2O_3$ concentrations (10^{-4} to 10^{-1} mol/L). The electrolyte in electrochemical cell (Figure 3-9) contained the 250 mL volume. All ASW were freshly prepared with deionised water (DI, Vunique®). All used chemicals were Analytical Reagent grades (AR grades).

Table 3-2 Summary of ASW with the varying the $Na_2S_2O_3$ concentration (mol/L)

No.	Electrolytes	Total $[S_2O_3^{2-}]$ (mol/L)
1	ASW	0
2	ASW + 10^{-4} M $Na_2S_2O_3$	0.0001
3	ASW + 10^{-3} M $Na_2S_2O_3$	0.001
4	ASW + 10^{-2} M $Na_2S_2O_3$	0.01
5	ASW + 10^{-1} M $Na_2S_2O_3$	0.1

Initially, the ASW (electrolyte No.1) was prepared according to ASTM D1141 [83]. The ASW was mixed by three stock solutions consisting of base solution, stock solution no.1 and stock solution no.2. Table 3-3 shows the chemical concentrations for all three stock solutions. The desired pH~8 was buffered by sodium hydroxide (NaOH).

Next, the ASW (electrolyte No.1) was mixed with sodium thiosulfate powder. Table 3-4 shows the weights of $Na_2S_2O_3$ (grams) in 250 mL. The electrolytes No.2 to No.5 were buffered to pH~3 by glacial acetic acid (CH_3COOH). The acidified ASW mixing with thiosulfate can be turned to white when the thiosulfate concentration was higher than 0.1 mol/L. The author expected that the thiosulfate might be decomposed to sulphide ions (S^{2-}) and/or hydrogen sulphide (H_2S) regarding the S-H_2O Pourbaix diagram (see Figure 2-18).

Table 3-3 Chemical composition of artificial seawater following ASTM D1141 standard [83]

	Compounds	g/L	g/mol
	Magnesium chloride (MgCl$_2 \cdot$ 6H$_2$O)	5.2	203.31
Stock solution no.1	Calcium chloride (CaCl$_2$)	1.16	110.98
	Strontium chloride (SrCl$_2 \cdot$ 6H$_2$O)	0.025	266.61
	Potassium chloride (KCl)	1.16	74.55
	Sodium hydrogen carbonate (NaHCO$_3$)	0.201	84.01
Stock solution no.2	Potassium bromide (KBr)	0.101	119.00
	Boric acid (H$_3$BO$_3$)	0.027	61.83
	Sodium fluoride (NaF)	0.003	41.99
Base solution	Sodium chloride (NaCl)	24.53	58.44
	Sodium sulphate (Na$_2$SO$_4$)	4.09	142.04

Table 3-4 Amounts of Sodium Thiosulfate salt in each condition

No.	Electrolytes	g/250 mL
1	ASW	0
2	ASW + 10^{-4} M Na$_2$S$_2$O$_3$	0.006
3	ASW + 10^{-3} M Na$_2$S$_2$O$_3$	0.062
4	ASW + 10^{-2} M Na$_2$S$_2$O$_3$	0.620
5	ASW + 10^{-1} M Na$_2$S$_2$O$_3$	6.205

3.3.2 Parameters in electrochemical techniques

Table 3-5 shows the summary for electrochemical parameters of each technique commanding in potentiostat. To verity the equilibrium state of surface sample, the WE were conducted by open-circuit potential measurement for 1 hr in every test. Each technique was run at room temperature.

Open Circuit Potential measurements

They were recorded for 1 hr to reach a steady-state free corroding condition. We assumed the passive film growth on the surface substrate when immersed in electrolyte.

Table 3-5 Summary electrochemical parameters of each technique commanding in potentiostat

Techniques	Time (s)	$E_{applied}$ (V_{SHE})	Step rate (V/s)	Frequency (Hz)	Amplitude (mV_{rms})
E_{ocp}	3,600	-	0.1	-	-
Potentiodynamic	-	-0.4 to 1.6	0.001	-	-
EIS	-	Fixed at E_{ocp}	-	0.01 to 10,000	10 mV_{rms}
Potentiostatic	3,600	1.3 (Transpassive)	0.1	-	
M-S	-	-0.6 to 1.4	0.1	Fixed at 1,000	-

Potentiodyanamic polarisation tests

They were carried out from potential range -0.2 V to 1.4 V with respect to E_{ocp} until the current density exceeded 1 mA with 0.5 mV/s sweep rate. When the experiment was done, collected the Tafel slope with Nova 2.1.4 software and plot the cathodic/anodic Tafel slope to compute the corrosion rate (mm/y)

Electrochemical Impedance Spectroscopy

EIS were conducted in the frequency from 10 kHz to 0.01 Hz with 7 points per decade using 10 mV_{rms} amplitude. The ZView® software were used for evaluating EIS records.

Potentiostic polarisation tests

They were conducted at the constantly applied at the 1.12 V_{SCE} (tranpassive region) for 1 hr. The recorded interval was 0.1 V/s (36,000 points). The steady-state current density was selected at the last point in the measurements.

Mott-Schottky analysis

The capacitance measurements were performed on the equilibrium state of passive film (ran after 1 hr stabilisation at E_{ocp}) at a fixed frequency of 1 kHz using 10 mV ac signal and a step rate of 0.1 V/s, in the cathodic direction. The step rate employed here was sufficient fast to satisfy the assumption of "frozen-in defect structure" for the Mott-Schottky theory.

CHAPTER 4

RESULTS AND DISCUSSION

This chapter is followed as described in Figure 1.1, consisting of six parts. The first part is the new duplex characterisations discussing with microstructure correlated with the Thermo-Calc diagram. The following parts discuss corrosion behaviours in the ASW and the acidified ASW mixing with thiosulfate at 25°C. Two types of duplex grades, the new duplex and 2205 DSS grades, were experimented with by various electrochemical tests: potentiodynamic polarisation test, Electrochemical Impedance Spectroscopy (EIS), potentiostatic polarisation test, and the Mott-Schottky (M-S) analysis. The pit initiation in the transpassive region of the polarisation curve was also investigated.

4.1   Sample characterisations

Table 4-1 shows the vol.-% averages of δ (ferrite) and γ (austenite) phases, the bulk chemical composition and $PREN_{16}$ of new duplex and 2205 DSS, respectively. The phase volume fraction of δ and γ phases in the new duplex were 0.60 and 0.40, respectively, in good agreement with the Thermo-Calc diagram (see Figure 3-4).

Table 4-1 The vol.% of phases, chemical composition (wt.%) and the $PREN_{16}$ values of the tested samples

Samples	Vol.%		Nominal chemical composition (wt.-%)							$PREN_{16}$
	δ	γ	C	Si	Cr	Ni	Mn	Mo	N	
New duplex	59	41	0.02	0.22	25.77	3.11	7.01	0.68	0.66	39
2205 DSS	55	45	0.02	0.34	22.18	5.68	1.37	3.15	0.18	36

Figures 4-1 and 4-2 display the example microstructures and XRD patterns of new duplex and 2205 DSS samples. Those shreds of evidence showed no existences of χ-phase and σ-phase and other deleterious compounds such as Cr_2N and carbide. Note that the rapidly quenching at 1050°C of the new duplex sample suppressed the precipitation of intermetallic phases.
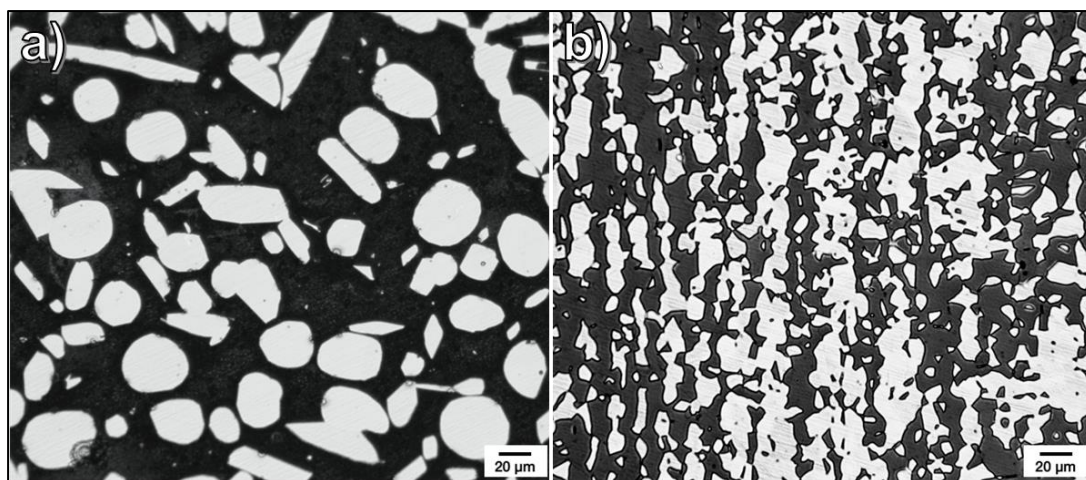
Figure 4-1 Optical microstructures of a) new duplex and b) 2205 DSS samples. The dark and bright areas represent δ and γ phases, respectively. The etchant was Beraha's solution [82].
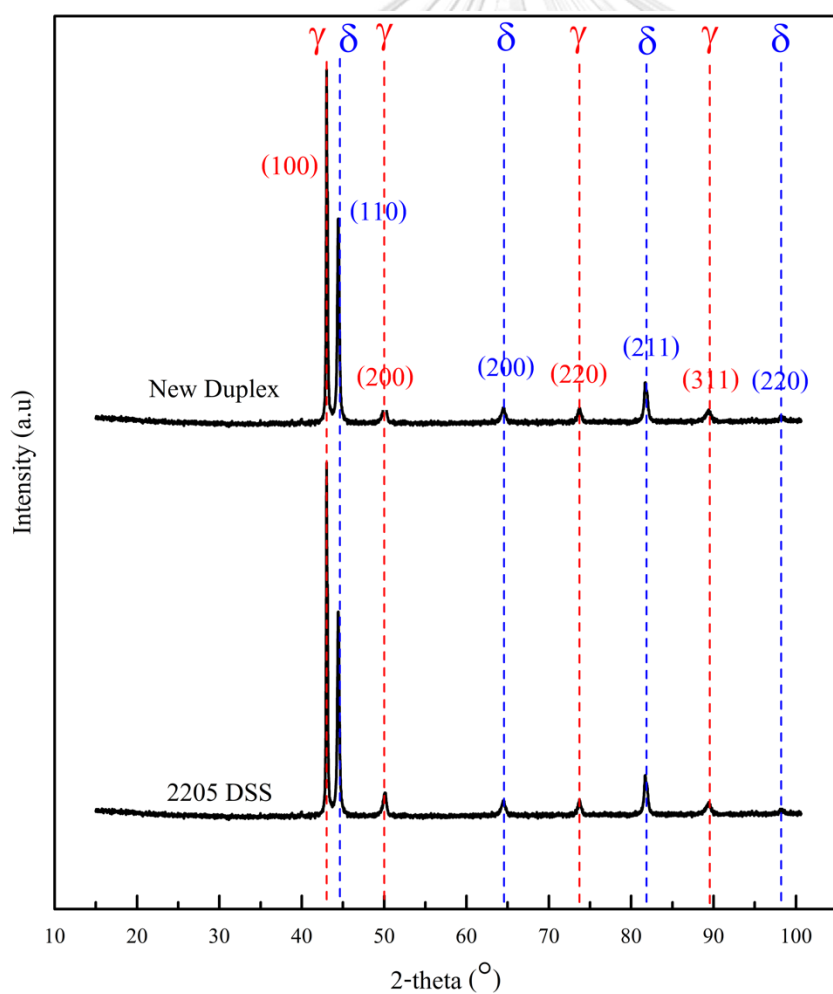
Figure 4-2 XRD patterns with indexing δ and γ phases.

According to the $PREN_{16}$ calculated from Equation 2.1, the value is the basic assessment of pitting corrosion resistance of stainless steels estimating from the Cr, Mo, and N contents. The $PREN_{16}$ of the new duplex was higher than that of 2205 DSS. It implied that the pitting corrosion resistance of the new duplex is higher than that of 2205 DSS.

Table 4-2 Chemical composition (wt.-%) and the values of $PREN_{16}$ of the γ and δ phases in new duplex, and 2205 DSS samples by the EPMA, EDS analyses, and Thermo-Calc calculation (SSLO5 database)

Samples	Phases	Chemical composition (wt.-%)					$PREN_{16}$
		Cr	Mo	Ni	Mn	N	
New duplex	δ (EPMA)	26.35	0.64	3.35	7.52	0.90	43
	δ (EDS)	26.84	0.63	3.16	7.01	0.35	35
	δ (Thermo-Calc)	27.6	0.96	2.16	6.24	0.04	31
	γ (EPMA)	24.08	0.39	3.98	9.56	2.61	67
	γ (EDS)	25.62	0.40	3.89	9.45	0.82	40
	γ (Thermo-Calc)	25.3	0.61	3.45	7.31	0.81	40
2205 DSS	δ (EPMA)	23.52	3.10	4.53	1.27	0.61	44
	δ (EDS)	22.59	3.05	4.37	1.22	0.06	34
	δ (Thermo-Calc)	23.4	3.70	4.10	1.21	0.003	36
	γ (EPMA)	20.79	1.95	6.86	1.29	1.30	48
	γ (EDS)	20.68	1.88	6.50	1.22	0.32	32
	γ (Thermo-Calc)	20.5	2.32	6.40	1.66	0.40	35

Table 4-2 shows the chemical compositions and the $PREN_{16}$ values of δ and γ phases according to the EPMA and EDS analyses compared to the Thermo-Calc calculation. From EPMA and EDS analyses, the δ phase contained higher contents of Cr and Mo, which are ferrite stabilisers, but the γ phase had larger amounts of Ni, Mn, and N, which are austenite stabilisers. However, the N contents from EPMA analysis in both phases were too high to be acceptable. On the other hand, the concentrations of N in both phases obtained by SEM/EDS were drastically lower than those

obtained by EPMA. It may be due to the different bias voltage of those electron probe equipment. The used voltage in EPMA and SEM/EDS analyses were 15 kV and 10 kV, respectively. From both techniques, the compositions of Cr, Mo, Ni, and Mn in both phases were not significantly different and closely matched with those obtained by Thermo-Calc calculations. Especially, the N contents in both phases are acceptable by Thermo-Calc calculations since they are not exceeded than the solubility limit in Fe-N phase diagram. The solubility limits of N in the δ-Fe and γ-Fe at 590°C are 0.10 wt.-% and 2.35 wt.-%, respectively) [84]. However, the $PREN_{16}$ values from EPMA and Thermo-Calc results showed the higher pitting resistance of γ phase than that of δ phase in both new duplex and 2205 DSS. These $PREN_{16}$ estimations will be discussed in the section of pit morphology investigation.

4.2   Potentiodynamic polarisation tests

Figure 4-3 shows the potentiodynamic polarisation curves of the new duplex and 2205 DSS in ASW and the acidified ASW mixing with thiosulfate at 25°C. The polarisation curves of the two samples exhibited similar shapes for all test conditions. Table 4-3 summarises the corrosion parameters obtained from the potentiodynamic polarisation curves for all test conditions.
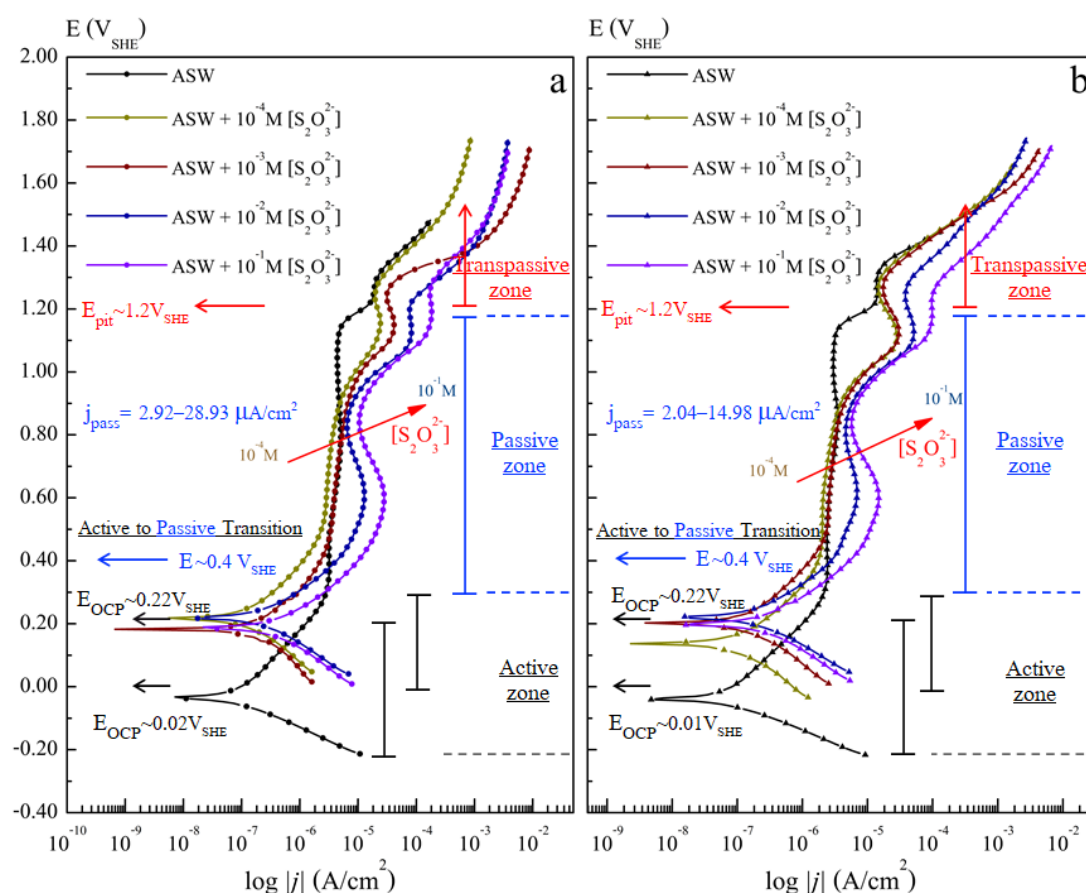
Figure 4-3 Representative of potentiodynamic polarisation curves for two samples; new duplex (a), and 2205 DSS (b), respectively.

When the WE or samples are immersed in the solution, the passive film can grow to reach the equilibrium state in the active region. In the active region, the sample usually in the state of general corrosion behaviour. From Figure 4-3, the cathodic and anodic curves look similar for all test conditions. It can be said that both cathodic and anodic curves of all samples obey the same Tafel's behaviour or electrochemical mechanism. The same corrosion potentials (E_{corr}) are -0.01 V_{SHE} in ASW, and nearly the same corrosion potentials are 0.20 V_{SHE} in acidified ASW mixing

with thiosulfate. The passive layers have higher current densities in the acidified ASW mixing with thiosulfate than in ASW. The thiosulfate may involve passive film structure such as higher defect density resulting in lesser passive film stability. The Mott-Schottky (M-S) analysis will further be discussed on the defect of the passive film of both samples in both ASW and the acidified ASW mixing with thiosulfate solutions. The corrosion current density (j_{corr}) values shifted slightly toward a positive direction or higher values with increasing thiosulfate concentration. This means a higher corrosion rate. The cathodic and anodic branches of each polarisation curves almost overlapped with those of other polarisation curves in all acidified ASW mixing with thiosulfate. The Tafel slopes of all cathodic and anodic branches are about 0.150 and 0.159 V/decade, respectively. It is indicated that the electrochemical mechanism in the active region is similar for all cases. The anodic dissolution rate may be responsible for the increase of corrosion current density and passive current density (j_{pass}). The active-passive transition implying the start of the passivation process on the surface sample appears at the anodic curves around 0.4 V_{SHE} in ASW. This behaviour is consistent with those reported in the literature [16].

Figure 4-4 shows the E-pH diagram (Pourbaix) of Cr-S-H$_2$O containing chloride solution [6, 85]. This diagram predicts the tendency of dealloying and evaluates the effect of environmental variables such as electrolyte composition, gas concentration, and ionic species as a function of potential and pH [85]. The diagram also presents that sulphur is likely to adsorb in the active region and may modify the kinetic dissolution into Cr^{2+}, Cr^{3+}, or $CrOH^{2+}$ and CrO_2^-. We will now discuss the polarisation behaviours based on the E-pH diagram and the defect generation along with the point defect model (PDM) [19].

Regarding passive film growth at the metal/film interface (see Figure 2-10), the E-pH diagram guides what the forward reaction occurs at the interested pH. The passive region is in the anodic potential range of 0.4 to 1.1 V_{SHE}. The additions of thiosulfate from 0 to 10^{-3} M in ASW electrolyte cause the slight difference in j_{pass} values of both samples about 2–5 μA/cm^2. According to the PDM [19], the oxygen vacancy ($V_O^{\bullet\bullet}$) and cation vacancy ($V_M^{\chi'}$) are generated at metal/film and film/solution interfaces, respectively (Figure 2-16). The $V_O^{\bullet\bullet}$ and $V_M^{\chi'}$ diffuse

outward and inward through the passive film, respectively. The formations of $V_O^{\bullet\bullet}$ at metal/film interface, and the passive film $(Cr(OH)_2^+)$ growth could be expressed as in Equations 4-1 to 4-3.

$$Cr^0 \longrightarrow Cr^{2+} + 2e^- \qquad\qquad \text{in neutral ASW} \qquad \text{Equation 4-1}$$

$$2Cr^{2+} + 3H_2O \longrightarrow Cr_2O_3 + V_O^{\bullet\bullet} + 6H^+ + 4e^- \qquad \text{in neutral ASW} \qquad \text{Equation 4-2}$$

$$Cr^{2+} + 2H_2O \longrightarrow Cr(OH)_2^+ + V_O^{\bullet\bullet} + 2H^+ + e^- \qquad \text{in neutral ASW} \qquad \text{Equation 4-3}$$
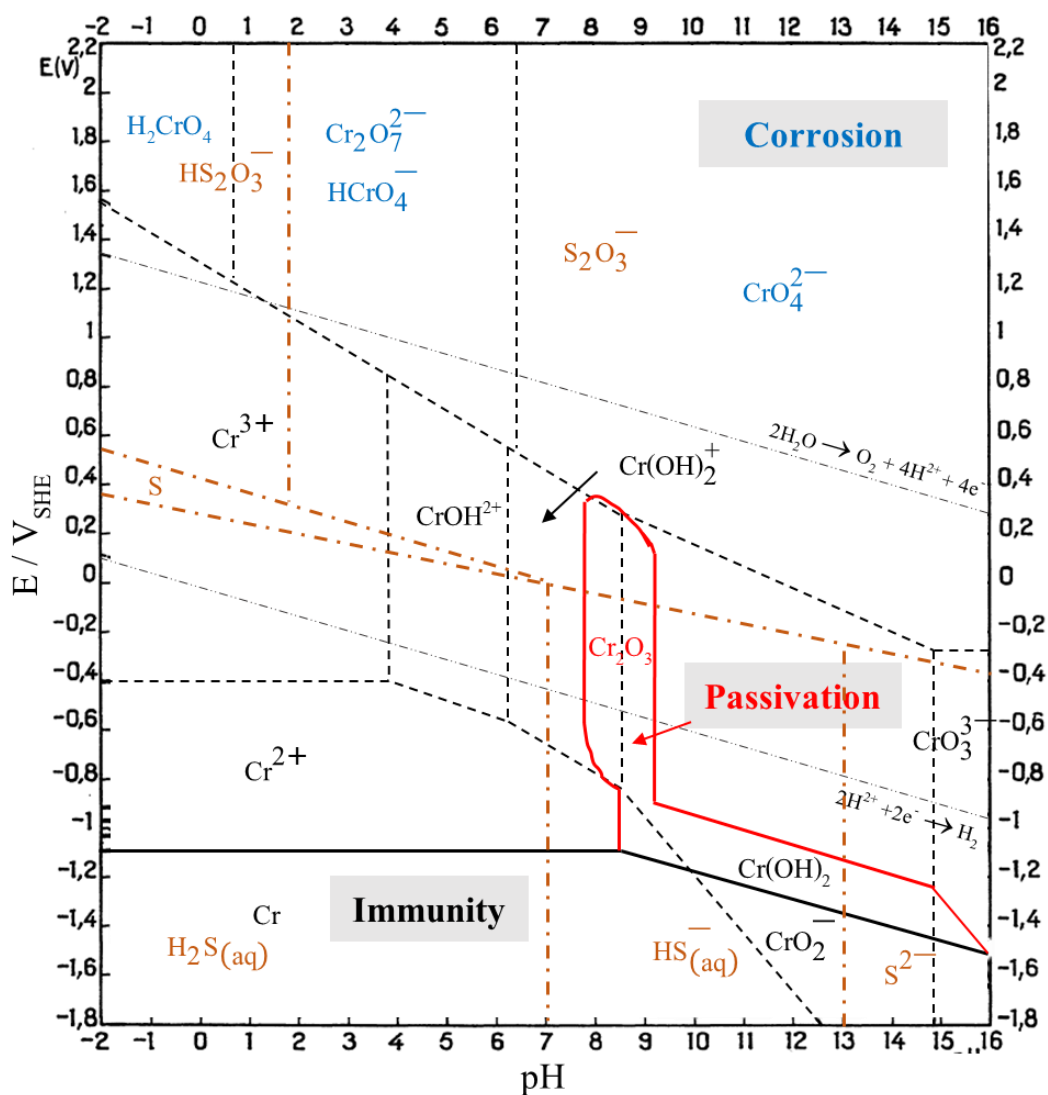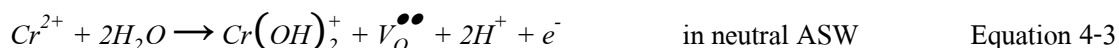
Figure 4-4 Superimposition of the two types E-pH equilibrium diagram for the system Cr-S-H$_2$O in a solution containing chloride at 25°C [85]. The lines limit the stability domains: ($—\cdot\cdot—$) H$_2$O systems; ($—\ —\ —$) Cr-H$_2$O systems; ($—\cdot—\cdot—$) S-H$_2$O systems. In this study, the pH solutions were about 3 and 8 in neutral and acidified ASW.

On the other hand, when the thiosulfate concentration exceeded 10^{-2} M, the anodic peak in the passive region was found at 0.6 V_{SHE} in the passive region, which was attributed to the passive dissolution. The reaction can be expressed as Equation 4-4.

$$Cr^{2+} \longrightarrow Cr^{3+} + e^{-}$$
in acidified ASW $\qquad$ Equation 4-4

Many articles proved bi-layer structures of the passive film when sample immersed in the aggressive anion or chloride ion solutions [14, 71, 86-91]. It is generally accepted that chromium oxide forms in the inner layer and chromium hydroxide forms in the outer layer of the passive film, respectively. This argument will be further discussed in the M-S analysis section.

When the passive layer dissolves or passive dissolution, it is proposed that the transpassive reaction begin. This can be observed by the increase of passive current density. In this sense, the cation vacancy ($V_M^{\chi'}$) is generated at the film/solution interface. Previously, the $Cr(OH)_2^{+}$ cation and Cr^{3+} cation are formed at the metal/film interface as Equations 4-2 and 4-3. They migrate across the passive film to the film/solution interface and dissolve into the solution as complex ions. The reaction at the film/solution interface can occur as Equations 4-5 and 4-6.

$$Cr(OH)_2^{+} + 2H_2O \longrightarrow CrO_4^{2-} + V_M^{\chi'} + 6H^{+} + 3e^{-}$$
in neutral ASW $\qquad$ Equation 4-5
$$Cr^{3+} + 7H_2O \longrightarrow Cr_2O_7^{2-} + V_M^{\chi'} + 14H^{+} + 6e^{-}$$
in acidified ASW $\qquad$ Equation 4-6
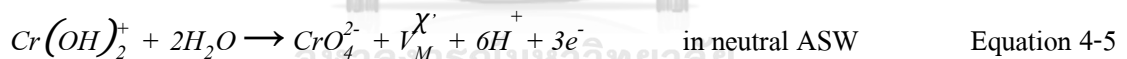
Those Equations result in the soluble formations of chromate (CrO_4^{2-} and $Cr_2O_7^{2-}$) or chromium hexavalent (VI) related to the E-pH diagram (Figure 4-4). This usually leads to pitting corrosion in the metal sample due to the nonuniform microstructure. The potential at pit occurrence is called pitting potential (E_{pit}). The average pitting potential values of two samples for all cases were about the same ~1.2 V_{SHE}. The thiosulfate in seawater has no influence on the pitting corrosion of samples. Finally, the current density increased suddenly when the applied potential reached ~1.60 V_{SHE}, indicating an oxygen evolution reaction.

However, the narrower passive region of the new duplex and 2205 DSS were found in the presence of thiosulfate in acidified ASW. This can be because the corrosion potential increase, but the pitting potential does not change. Thiosulfate may retard the passivation process, which is confirmed in the report of [15-17, 76, 78, 91]. The higher j_{pass} value is related to the higher ion exchange rate of passive film in acidified ASW mixing with thiosulfate (Table 4-3). This degradation was mainly attributed to the catalytic effect of the species from thiosulfate decomposition (Equations 2-16 and 2-17), leading to H_2S and/or HSO_4^-. The adsorbed H_2S and/or HSO_4^- accelerated the metal dissolution and thus increased the anodic current density [9, 13, 16, 17, 76, 78, 91]. Philippe Marcus et al. [10] implied that a sulphur monolayer (S) could be formed on Cr and prevent passivation. In the potentiodynamic polarisation results (Figure 4-3), the passive behaviours of the two samples are similar, which is in good agreement with the prediction of $PREN_{16}$ values (Table 4-1).
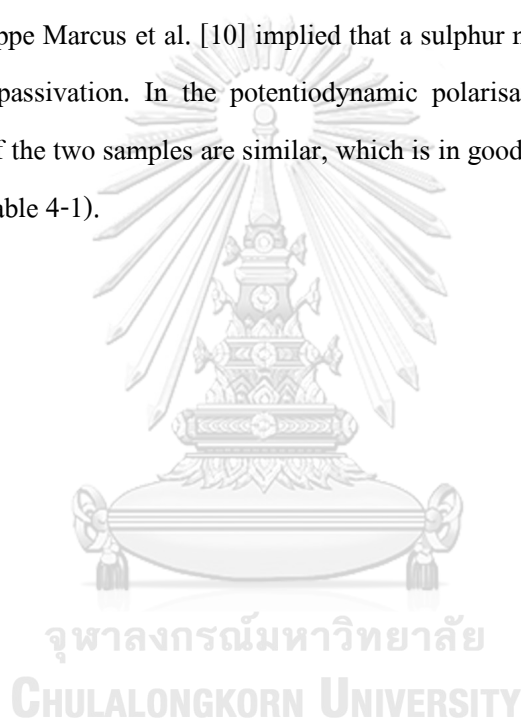
Table 4-3 Summary corrosion parameters obtained from potentiodynamic polarisation curves calculated by the NOVA 2.1.4 software

Samples	Corrosion Parameters	Solution conditions				
		1: ASW	2: ASW+10^{-4}M [$S_2O_3^{2-}$]	3: ASW+10^{-3}M [$S_2O_3^{2-}$]	4: ASW+10^{-2}M [$S_2O_3^{2-}$]	5: ASW+10^{-1}M [$S_2O_3^{2-}$]
New Duplex	E_{ocp} (V$_{SHE}$)	0.020 ± 0.001	0.176 ± 0.002	0.192 ± 0.002	0.256 ± 0.001	0.221 ± 0.002
	E_{corr} (V$_{SHE}$)	-0.035 ± 0.001	0.215 ± 0.003	0.180 ± 0.003	0.217 ± 0.001	0.223 ± 0.001
	j_{corr} (μA/cm^2)	0.082 ± 0.002	0.168 ± 0.001	0.246 ± 0.001	0.371 ± 0.001	0.459 ± 0.001
	j_{pass} (μA/cm^2)	2.917 ± 0.002	3.678 ± 0.003	3.977 ± 0.003	12.654 ± 0.002	28.927 ± 0.001
	E_{pit} (V$_{SHE}$)			~1.2		
	Corrosion rate (mm/y)	0.001 ± 0.001	0.002 ± 0.001	0.003 ± 0.001	0.004 ± 0.001	0.005 ± 0.002
2205 DSS	E_{ocp} (V$_{SHE}$)	0.006 ± 0.001	0.166 ± 0.002	0.209 ± 0.003	0.211 ± 0.003	0.219 ± 0.003
	E_{corr} (V$_{SHE}$)	-0.036 ± 0.003	0.122 ± 0.003	0.209 ± 0.002	0.222 ± 0.001	0.205 ± 0.001
	j_{corr} (μA/cm^2)	0.073 ± 0.002	0.163 ± 0.003	0.204 ± 0.004	0.222 ± 0.003	0.312 ± 0.002
	j_{pass} (μA/cm^2)	2.041 ± 0.002	2.381 ± 0.001	2.481 ± 0.001	6.639 ± 0.001	14.98 ± 0.002
	E_{pit} (V$_{SHE}$)			~1.2		
	Corrosion rate (mm/y)	0.001 ± 0.002	0.002 ± 0.002	0.002 ± 0.001	0.003 ± 0.001	0.004 ± 0.001

4.3   Pit morphology on weaker phase

Figure 4-5 shows the SEM images of pit morphology in the new duplex and 2205 DSS after the potentiodynamic polarisation test in ASW and acidified ASW mixing with 10^{-1} M thiosulfate. The micrographs displayed the pits mostly established in the δ phase in all cases. That is to say, the γ phase has a higher pitting resistance than the δ phase correlating with the $PREN_{16}$ values from the EPMA results and Thermo-Calc calculation (Table 4-2). The presence of thiosulfate in ASW can influence the degradation of the passive layer of δ phase more than that of γ phase.

Many articles [4, 5, 92] proved that the pit took place where the effect of alloying element in the parent phase led to lower pitting susceptibility resulting in the precursor site of pit initiation. Yang et al. [92] and G. Lothongkum et al. [5] showed the evidence of N as the key-alloying element to increase the corrosion resistance of the γ phase by revealing the pit locations at δ phase. N was richer in the γ phase resulting in higher pitting corrosion resistance than the δ phase, richer in Cr and Mo. The investigation in this work is in good agreement with other studies [4, 5, 92]. However, the polarisation results of the two duplex grades were not significantly different. It possibly due to the mix effect of all elements in alloys, as shown in Table 4-1.

In neutral ASW

In acidified ASW + 10^{-1} M $Na_2S_2O_3$
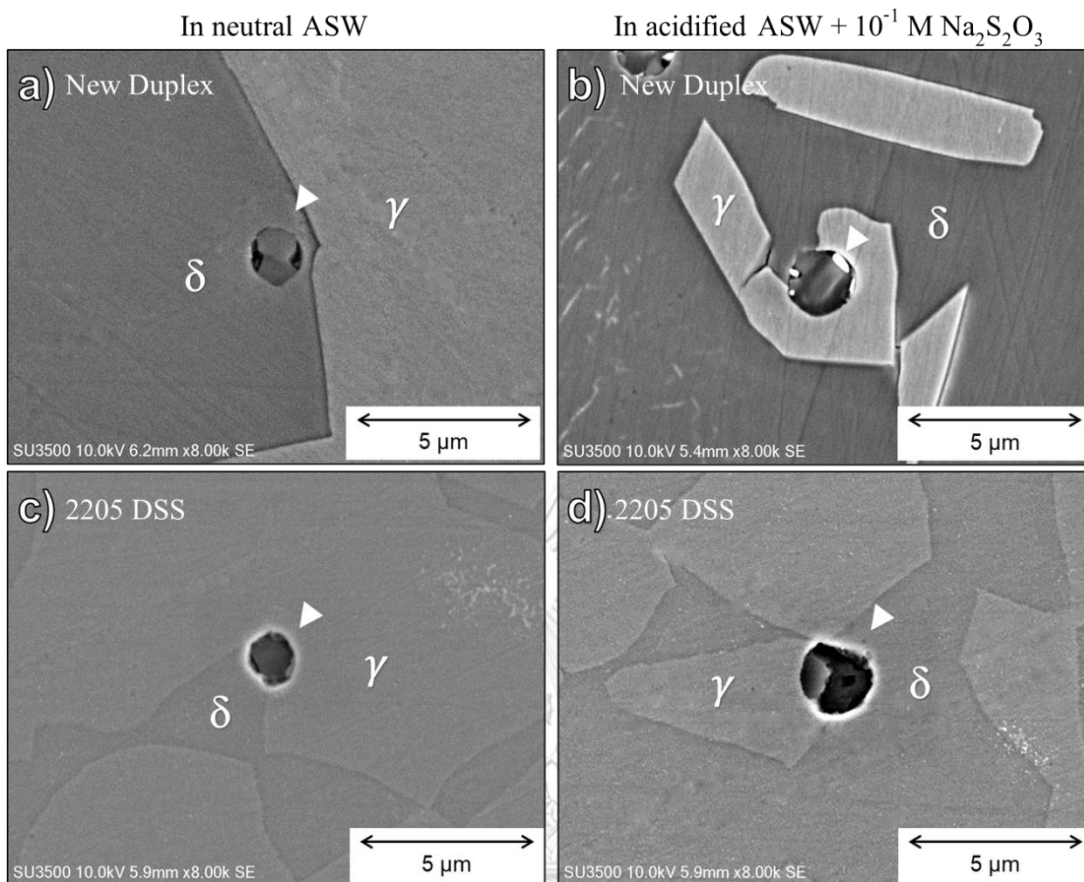
Figure 4-5 SEM images of pit morphology observation after potentiodynamic polarisation tests of new duplex and 2205 DSS samples in neutral ASW (condition No. 1) and acidified ASW + 10^{-1} M $Na_2S_2O_3$ (condition No. 5).

4.4 Electrochemical impedance spectroscopy (EIS) analysis

To investigate the effects of thiosulfate in ASW related to the stability of passive film formed on different duplex grades, EIS was carried out at the open circuit potential (Table 4-3). Figure 4-6 shows the Nyquist and Bode modulus/phase plots of new duplex and 2205 DSS samples in ASW and acidified ASW mixing with thiosulfate. Table 4-4 summarises the impedance parameters obtained by the Equivalent Electrochemical Circuit (EEC) fitting curve, which are acceptable according to the low chi-squared (χ^2) values.

From Figures 4-6 a) and b), the impedance spectra of two samples or Nyquist plots show an incomplete semicircles curve but similar semicircles after curve fitting. A similar passive film composing both resistance and capacitance is expected because of a single semicircle. Figure 4-6 c) and d), the Bode modulus shows the solution resistance (R_s) behaviour in the high-frequency domain. The medium to low-frequency domains (1-0.01 Hz) showed the slanted slope representing the charge transfer resistance and conductance of passive film. Figure 4-6 e) and f) exhibit a single loop of the Bode phase vs frequency plot confirming a single semicircle plot after curve fitting in the Nyquist diagram [93]. The angle maxima of the Bode phase of all curves was smaller than $90°$, suggesting a deviation from ideal capacitor behaviour at high frequency (low time constant). The impedance (Z) response in the electrochemical impedance system should be the constant phase element (Q_{CPE}) because it is not a pure capacitor or non-ideal behaviour of a capacitive element [94]. Note that Z = $1/Q_{CPE}$, when the values of Q_{CPE} increased and R_p decreased, the stability of passive film behaves more difficult charge transfer path, resulting in the higher corrosion susceptibility. The diameter of the capacitive arc exhibited a significant change with the thiosulfate content (Figure 4-6 a and b), indicating the degradation of passive film. Accordingly, it can be deduced that the addition of thiosulfate deteriorates the passive film in the passive region. The EIS result was in good agreement with the potentiodynamic polarisation test (Figure 4-3).
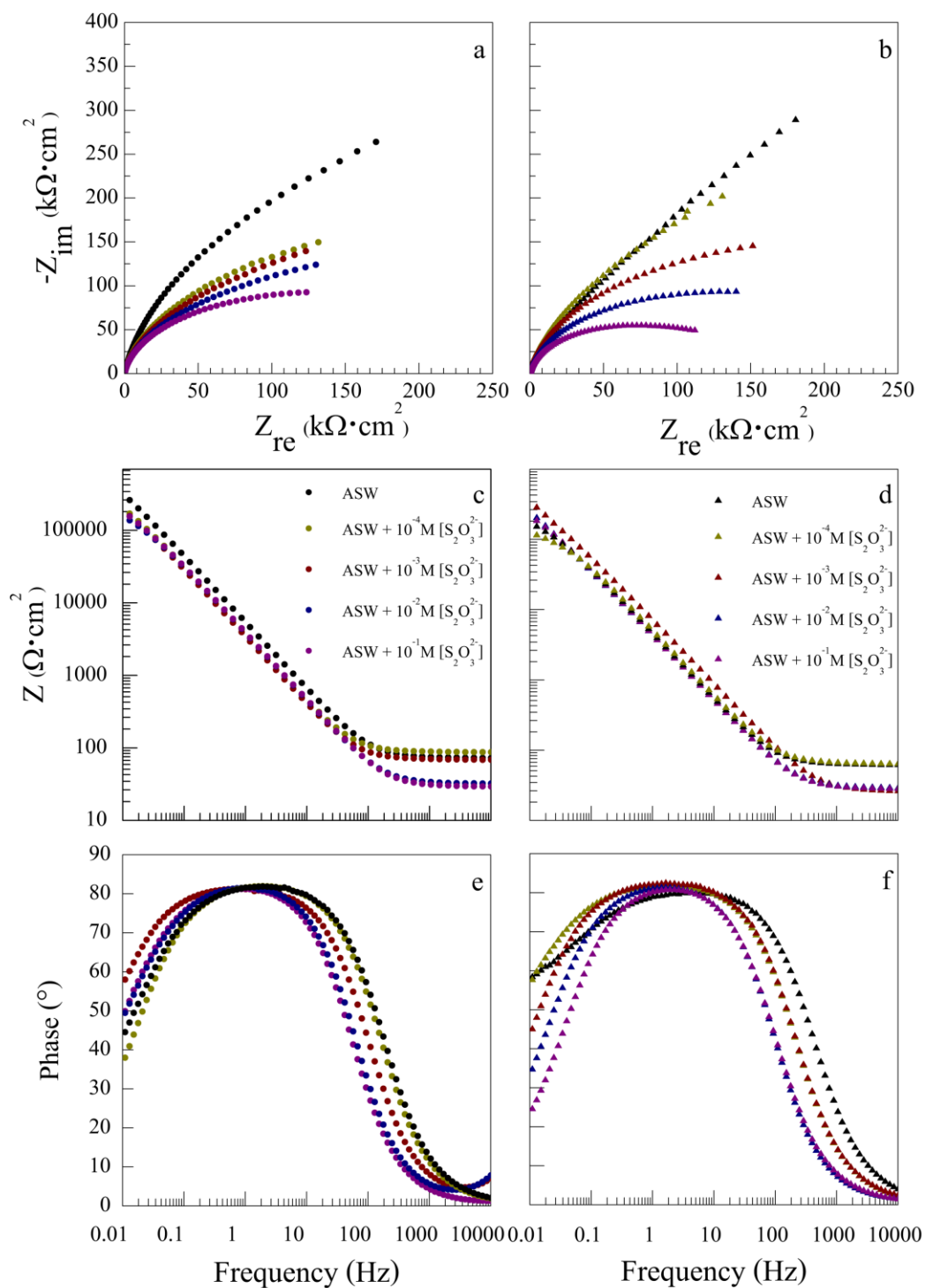
Figure 4-6 Representative of the Nyquist plots (a,b) and Bode modulus (c,d) and Bode phase (e,f) for two samples; new duplex (a,c,e), and 2205 DSS (b,d,f), respectively. The impedance results were recorded after 1 hr stabilisation at E_{ocp} in every conditions.
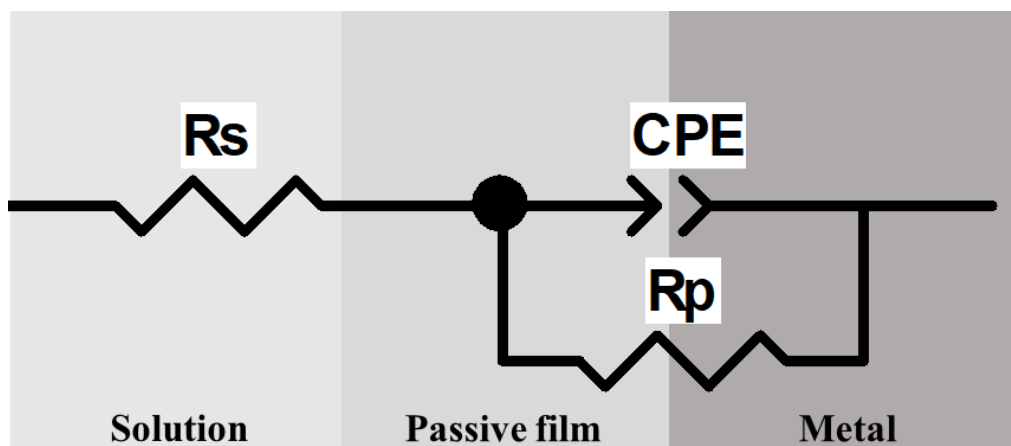
Figure 4-7 The equivalent electrochemical circuit (EEC) for EIS fitting

Figure 4-7 shows the $R_S(Q_{CPE}R_p)$ EEC in this study. The element of solution resistance (R_S) is in series to the parallel combination of Q_{CPE} and polarisation resistance (R_p), which is the corrosion resistance of the sample. Figure 4-8 shows the values of R_p as a function of thiosulfate concentration calculated from EIS data. The R_p values are coincident with the corrosion rate and passive current density from the potentiodynamic polarisation results. The higher R_p is the better the corrosion resistance. From R_p results, it can say that the passive film stability of the new duplex is better than 2205 DSS in ASW, but it is reverse in the acidified ASW mixing with thiosulfate. It is possibly due to the different chemical composition in the passive films of δ and γ phases relating to the elemental content in each phase obtained by EPMA results (Table 4-2). The dissolution was found in the δ phase, as shown in Figure 4-5. It is expected that the γ phase performs a thinner and denser passive layer than the δ phase because of higher $PREN_{16}$. The thinner passive film layer was shown to perform higher pitting corrosion resistance in Fe-Cr alloys [46, 86] and Fe-Cr-Ni alloys [80]. The XPS results showed that the higher pitting corrosion resistance was related to the denser layer of the mixed chromium and iron oxides in the passive film [80]. The denser layer may involve alloying elements and a degree of defects, which may suppress the charge transfer process in the passive layer. Yet, the EIS analysis was unable to confirm how disordered structure of the passive film. A better passive property of the 2205 DSS sample in acidified ASW mixing with thiosulfate further discusses the Mott-Schottky analysis.
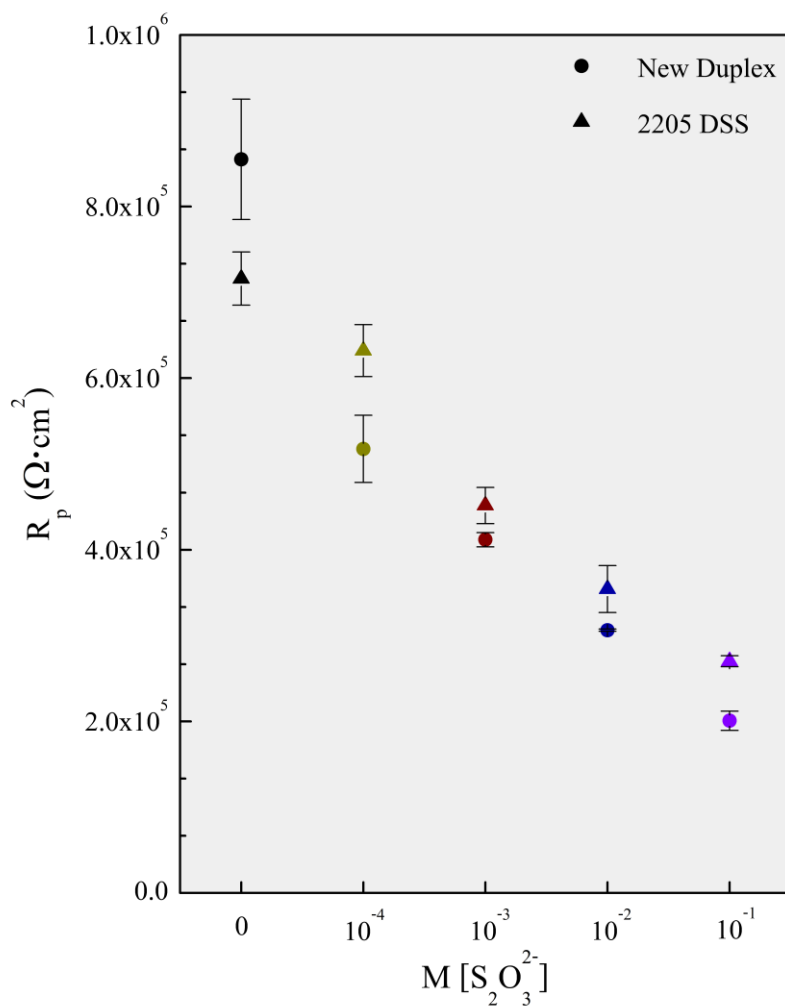
Figure 4-8 Summary of the polarisation resistance (R_p) as a function of thiosulfate concentration of new duplex and 2205 DSS samples

4.5   Potentiostatic polarisation tests

To verify the cation vacancy condensation at the metal/film interface leads to the detachment of passive film at this interface, causing the effects of addition thiosulfate in chloride solution (Figure 2-17). The potentiostatic technique is constantly fixed potential and measured the current signal with respect to time. Thereby, the obtained steady-state current density (j_{ss}) values verify how passive behaviours in an interesting solution. The steady-state dependence of the passive current density (j_{pass}) on the formation potential may be related to the change in the structures and properties of the passive film, i.e., degree of defect density.
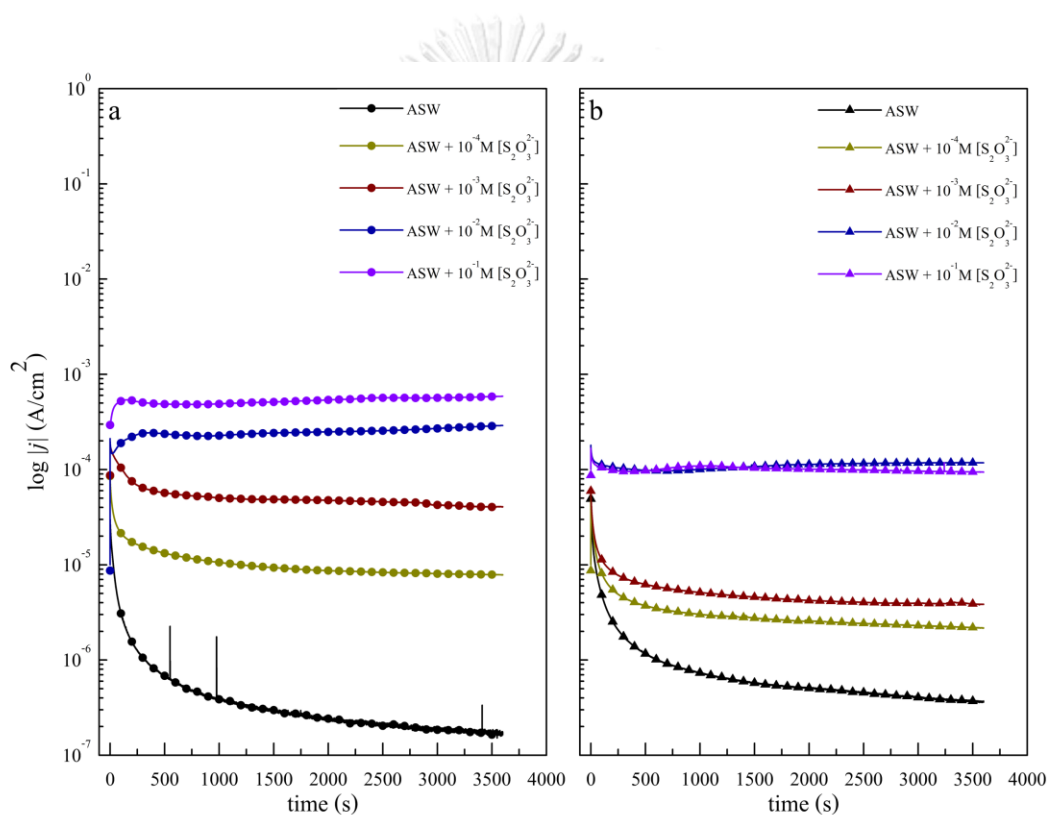
Figure 4-9 Representative of current density versus time plots for two samples; new duplex (a) and 2205 DSS (b), respectively. For the 1 hr measurements of record current signal, the potential was constantly applied at 1.3 V_{SHE} in every condition.

Figure 4-9 shows the current density versus time transient curves, applying the potential at the tranpassive region (~1.3 V_{SHE}) for new duplex and 2205 DSS samples in the ASW and acidified ASW mixing with thiosulfate. Initially, the current was rapidly decreased with time and maintained relatively stable values with a further increase of time. Note that this behaviour

represented characteristics of the balance of film formation and dissolution [16]. Furthermore, the metastable pitting occurred, which illustrated by the small current peaks spike, and then the re-passivation process occurred rapidly. All the current curves exhibited similar variation tendencies, demonstrating that forming process of the passive film. The steady-state current density of two duplex grades was substantially higher when increasing thiosulfate concentrations, indicating that the additional thiosulfate catalysed the cation vacancy generation in the presence of chloride, resulting in the deteriorated passive film property. These results were in good agreement with the values of j_{pass} and corrosion rate obtained by potentiodynamic polarisation curves (Figure 4-3 and Table 4-3).

Figure 4-10 and Table 4-5 show the j_{ss} values as a function of the thiosulfate concentration of the new duplex and 2205 DSS. The current density value was obtained from the average value at the end of the j_{ss} - time decay curves in Figure 4-9. The j_{ss} of the new duplex was lower than that of 2205 DSS in the ASW but higher in acidified ASW. According to the transpassive reaction in acidified condition (Reaction 4-6), these results imply that the passive film of 2205 DSS may be stabilised by the formation of Molybdenum hexavalent (Mo(IV)) during transpassive dissolution because of the higher Mo content in the bulk composition. Mo(IV) doping in the oxide film interacts with the point defects leading to lower cation vacancy condensation [95-97]. These results coincide well with the EIS results. However, the defect density on both duplex grades should be elucidated in the following Mott-Schottky analysis.
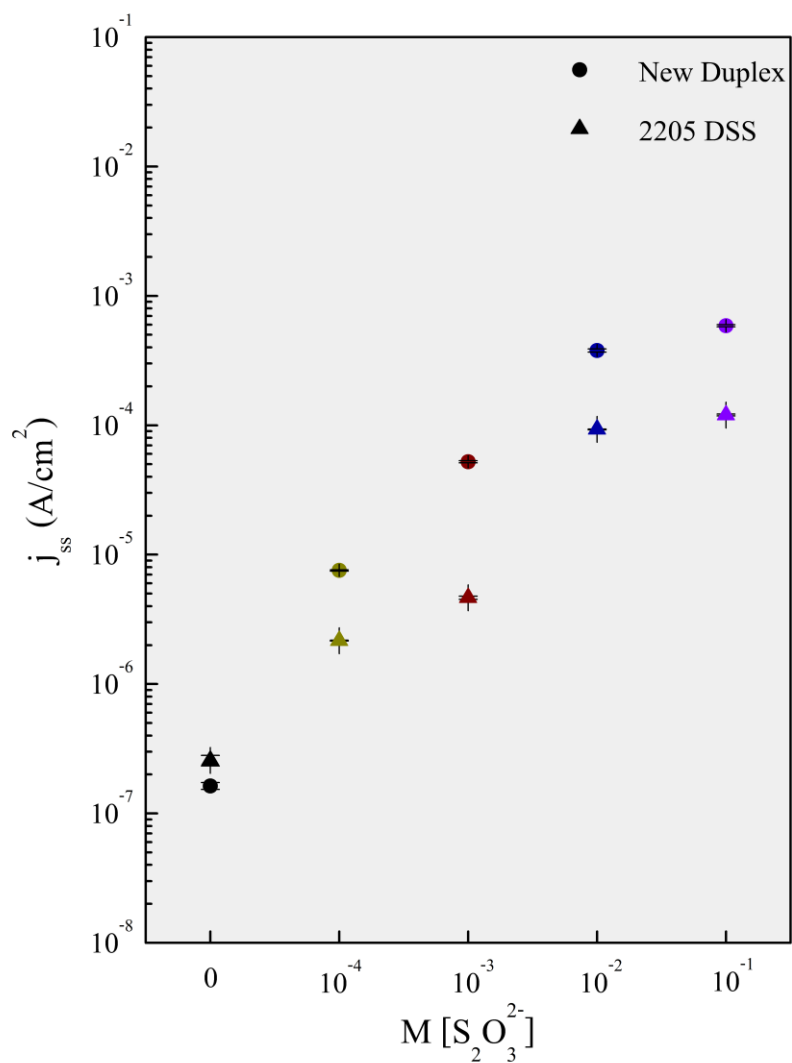
Figure 4-10 Summary of the steady-state current density (j_{ss}) as a function of thiosulfate concentration of new duplex and 2205 DSS samples

Table 4-4 Summary fitting parameters of the $R_S(Q_{CPE}R_P)$ EEC calculated by ZView software

Samples	Parameters	Solution conditions				
		1: ASW	2: ASW+10^{-4}M [S$_2$O$_3^{2-}$]	3: ASW+10^{-3}M [S$_2$O$_3^{2-}$]	4: ASW+10^{-2}M [S$_2$O$_3^{2-}$]	5: ASW+10^{-1}M [S$_2$O$_3^{2-}$]
New Duplex	R_S (Ω·cm^2)	86.12±14.20	90.33±11.01	89.33±15.89	88.25±17.89	89.74±14.76
	R_P (kΩ·cm^2)	855±70.01	518±39.01	412±8.23	306±1.23	201±11.21
	Q_{CPE} (μF/cm^{2}s$^{\alpha-1}$)	25.46±4.95	33.38±2.52	41.34±10.85	43.17±7.39	42.03±5.06
	α	0.92±0.002	0.92±0.007	0.93±0.001	0.92±0.003	0.92±0.002
	χ^2 (×10^{-4})	1.51	1.25	1.66	1.87	1.56
2205 DSS	R_S (Ω·cm^2)	90.22±13.44	87.56±14.66	89.45±12.45	87.56±19.21	89.45±14.22
	R_P (kΩ·cm^2)	716±25.3	632±21.4	452±17.3	354±19.3	270±5.2
	Q_{CPE} (μF/cm^{2}s$^{\alpha-1}$)	25.20±0.96	30.24±3.79	40.80±2.52	42.20±4.22	44.05±8.68
	α	0.92±0.004	0.92±0.001	0.92±0.006	0.93±0.001	0.92±0.009
	χ^2 (×10^{-4})	1.45	1.68	1.27	1.78	1.69

Table 4-5 Summary parameters of steady-state current density obtained by potentiostatic polarisation tests under the constant potential applied at 1.3 V$_{SHE}$

Samples	Parameters	Solution conditions				
		1: ASW	2: ASW+10^{-4}M [S$_2$O$_3^{2-}$]	3: ASW+10^{-3}M [S$_2$O$_3^{2-}$]	4: ASW+10^{-2}M [S$_2$O$_3^{2-}$]	5: ASW+10^{-1}M [S$_2$O$_3^{2-}$]
New Duplex	j_{ss} (μA/cm^2)	0.2±0.01	7.5±0.1	52.3±0.9	377.9±10.8	588.3±10.4
2205 DSS	j_{ss} (μA/cm^2)	0.3±0.02	4.6±0.02	4.6±0.13	93.0±0.67	120.0±2

4.6   Mott-Schottky (M-S) analysis

The defects and electrical property of a semiconductive passive film can be explained by the fundamental of Mott-Schottky theory [19, 63]. The M-S explanation provides the correlation between the square of reciprocal capacitance ($1/C^2$) as a function of applied potential (E) obtained by Equation 2-12.

Figure 4-11 shows the M-S plots of new duplex and 2205 DSS samples in ASW and acidified ASW mixing with thiosulfate after 1 hr stabilisation at E_{ocp}. The range of applied potential (-0.6 to 1.4 V_{SHE}) was in the passive region to transpassive regions regarding the potentiodynamic polarisation test. The results show a similar capacitive character of the formed passive film in all ASW on both duplex grades, consisting of four regions. The bi-layer structures of the passive film consist of the p-type semiconductor (inner layer) in Region I and n-type semiconductor (outer layer) in Region II. Those two linear curves are separated by a flat band condition in the narrow zone. The flat band potential (E_{fb}) of both duplex grades in ASW was -0.15 V_{SHE}, and acidified ASW mixing with thiosulfate was 0.0 V_{SHE}. The presence of *HS* and/or *H₂S* by thiosulfate dissociation in aqueous changed the electronic property of the passive layer by shifting the flat band potential (E_{fb}) to more positive values. It means that the nobler passive layer and the higher E_{ocp} values on both duplex grades, compared to the ASW case (Table 4-3). The M-S result was in good agreement with many works [16, 18, 71, 76, 78, 90, 91] and the passive domain in the Pourbaix diagram (Figure 4-4).

In Region III, the semiconductive character acts as a p-type semiconductor because there is a generation of the cation vacancy from the transpassive dissolution at the film/solution interface (Equation 4-5 and Equation 4-6). In Region IV, it exploits n-type character, probably due to the presence of additional electron charges from an oxidation reaction, for example, *S²⁻* to *S*, or due to the variation of the chemical composition of passive film during the polarisation process. However, these last two stages are not discussed in this work.
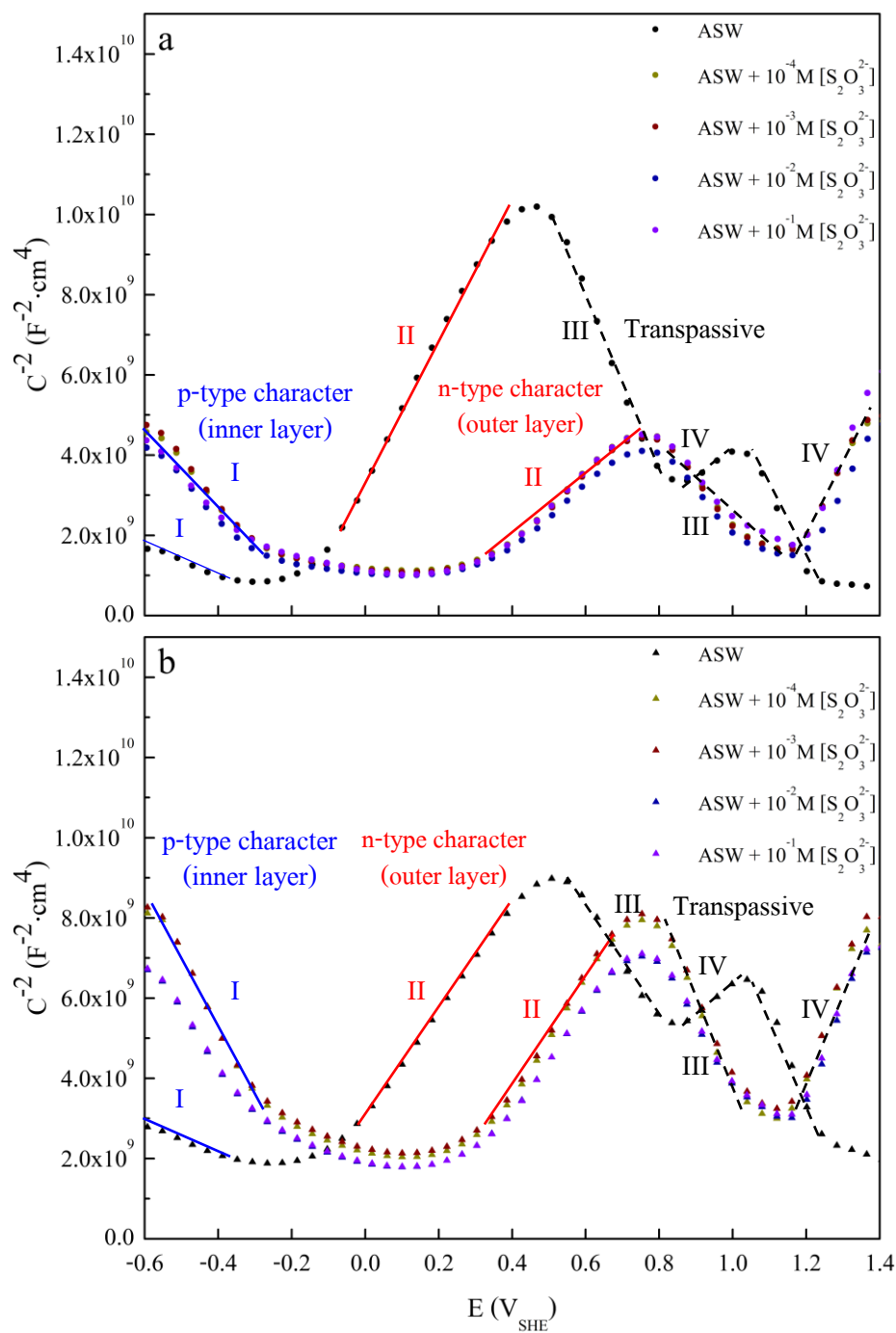
Figure 4-11 Representative of Mott-Schottky plots for two samples; new duplex (a), and 2205 DSS (b), respectively.

Table 4-6 and Figure 4-12 show the values of acceptor density (N_A) and donor density (N_D) of new duplex and 2205 DSS samples in all ASW solutions calculated by Equation 2-12 using the

negative and positive slope, respectively. The density values were in order of $10^{20}/cm^3$, which are acceptable in a similar potential range reported for oxide films of stainless steels [16, 18, 71, 91].

It is apparent that the higher thiosulfate concentration increases the higher densities of defects. In this work, the acceptor density (N_A) and donor density (N_D) increase with the increased conductivity of passive film, implying that higher defect density will lead to higher j_{pass} and ion exchange rates in passive film. These results coincided well with the potentiodynamic polarisation test (Figure 4-3 and Table 4-3). The passive film was composed of the inner p-type and outer n-type semiconductors in all conditions from the M-S analysis. We will now separately discuss the semiconductive behaviours in ASW and acidified ASW mixing with thiosulfate.
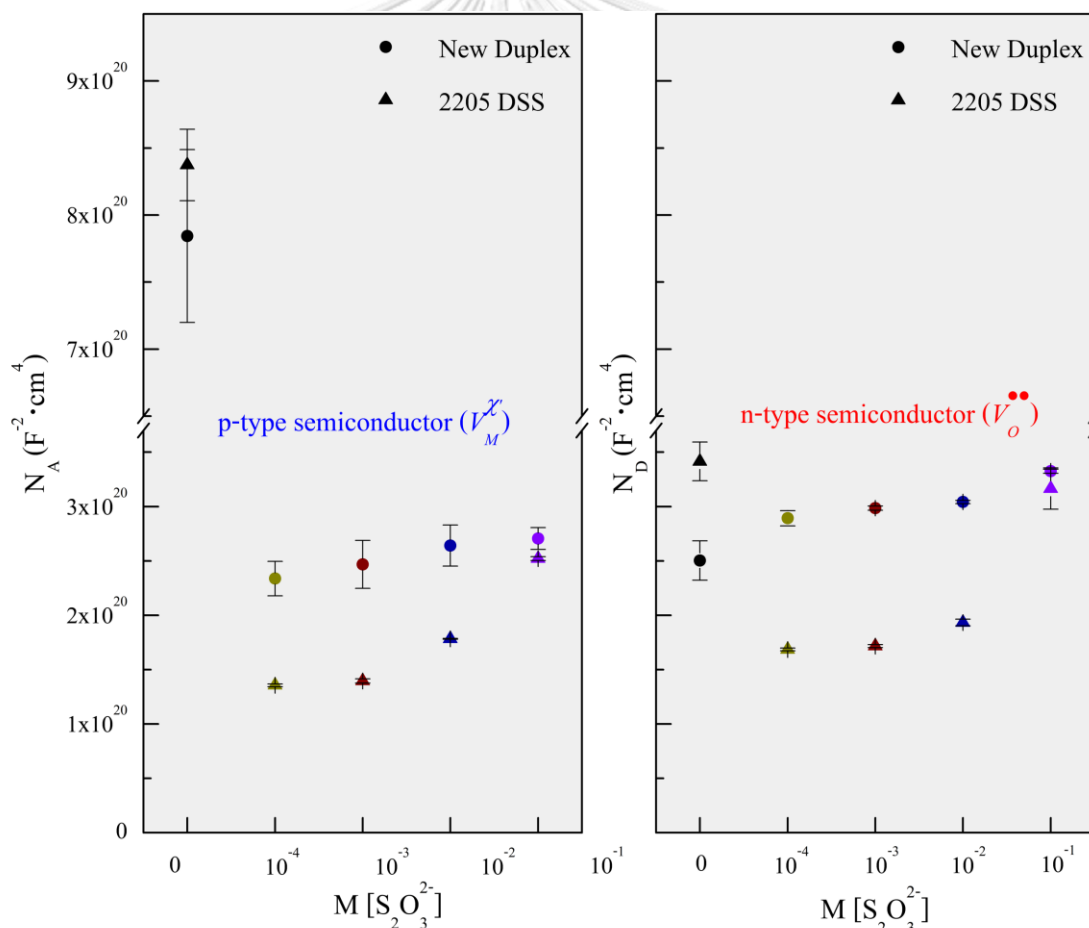
Figure 4-12 Summary of calculated an acceptor density (N_A) in the inner layer (left) and a donor density (N_D) in the outer layer (right) as a function of thiosulfate concentration of new duplex and 2205 DSS samples

In ASW, we imply that the formed passive film is denser than acidified ASW, resulting in more corrosion resistance. It is seen that the N_A is higher than the N_D for all duplex samples. So, the N_A should represent the predominant of $V_M^{\chi'}$ and the N_D should represent the predominant of $V_O^{\bullet\bullet}$. In this work, the passive films of all duplex samples performed higher cation vacancy density than oxygen or anion vacancy density (Figure 4-12). It is possibly due to the generation of absorbed chloride anion ($Cl_O^{\bullet}$) at film/solution interface (Equation 2-13). However, both types of defect density of the new duplex sample were lower than that of 2205 DSS, indicating that the passive property of the new duplex grade is better than the latter when exposed in the ASW. This result was in good agreement with polarisation and EIS experiments. The author expected that the benefit of high Nitrogen content might decrease N_D or $V_O^{\bullet\bullet}$ but increased N_A or $V_M^{\chi'}$ of the passive film. Grabke [25] and Ha [88] postulated the presence of negatively charged $N^{\delta-}$ at the metal/film interface, which was possibly occupied with $V_O^{\bullet\bullet}$, this results in a decrease of N_A and an increase N_D by alleviating the defectiveness of passive film in the outer layer, according to Equation 4-7.

$$N^{\delta-} + V_O^{\bullet\bullet} \longrightarrow N_O \hspace{4cm} \text{Equation 4-7}$$

Wang et al. [71] presented the decrease of N_A caused by the excess negative charged Nitrogen atom replacing the oxygen atom in the Cr_2O_3 inner layer to become Cr_2O_2N. Afterwards, the Cr_2O_2N annihilated the $V_O^{\bullet\bullet}$ at the metal/film interface according to Equation 4-8. These two annihilation reactions of anion vacancy have been still needed direct evidence to confirm this.

$$Cr_2O_2N + V_O^{\bullet\bullet} \longrightarrow Cr_2O_3 + 2CrN \hspace{3cm} \text{Equation 4-8}$$

Nevertheless, the highest cation vacancy accumulation (inner layer) on both duplex grades in ASW is still unclear compared to the acidified ASW with the additional thiosulfate. We expected a higher accumulation of defects in the inner layer because of the lower E_{ocp} values at the equilibrium state. The passive film may contain more disordered structures and higher defect densities than those formed at higher E_{ocp} [98, 99]. This evidence is needed to be confirmed by other passive film characterisation techniques. Accordingly, the new duplex's passive film property is more pronounced than 2205 DSS. The synergistic effects of Chromium and Nitrogen

should lead to a lower accumulation of defects at the inner layer and outer layer. These results are in good agreement with potentiodynamic, potentiostatic polarisation tests and EIS measurement.

In the acidified ASW with varying thiosulfate concentrations, the presence of the HS^- and/or H_2S probably increases both N_A and N_D values of both duplex grades (Table 4-6). The less-dense and more defect density in the passive layer of the new duplex sample resulting in higher corrosion susceptibility and higher conductivity than 2205 DSS.

All previous results could be attributed to the different chemical compositions of the passive film, resulting in the different defect densities. Mo containing in bulk composition and enriching in δ-phase is much difference between both duplex grades (Table 4-1 and Table 4-2). This Mo possibly could deduce the vacancy condensation (cation vacancy) by compensating the voids and providing a more rapid re-passivation process in a thiosulfate-containing environment. However, this temporary hypothesis suggests that the release mechanism of Mo could play a critical role in the more corrosion resistance of 2205 DSS than the new duplex sample. However, it is still less well understood and needed more evidence.

Figure 4-13 shows the Mo-S-H_2O Pourbaix diagram at room temperature [85]. At equilibrium state, the higher E_{ocp} values (0.0 to 0.2 V_{SHE}) confirm the formation of MoO_2 on the passive layer [95-97]. The diagram shows that Mo can be dissolved at a relatively low potential under an acid environment to form a stable MoO_2. At higher anodic potential, the formation of MoO_3 is proposed. Many articles reported about the actions of Mo^{6+} and Mo^{4+} species [97, 100, 101]. The Mo^{6+} absorbs at the film/solution interface to be a barrier layer inhibiting the larger pit nucleation, resulting in a small dissolution. The Mo^{4+} absorbs at metal/film interface to limit the dissolution rates of Fe and Cr. The role of MoO_3 (Mo^{6+}) is film dissolution inhibition and enhances the dissolving rate of metal cation from the film at a high potential range. The smaller N_D values of passive film of 2205 DSS sample also indicate the denser of the passive film. The MoO_2 may be formed and stabilised in the passive film of 2205 DSS in acidified ASW mixing with thiosulfate to provide a higher corrosion resistance than the new duplex sample. These M-S results coincide well with the earlier ones.
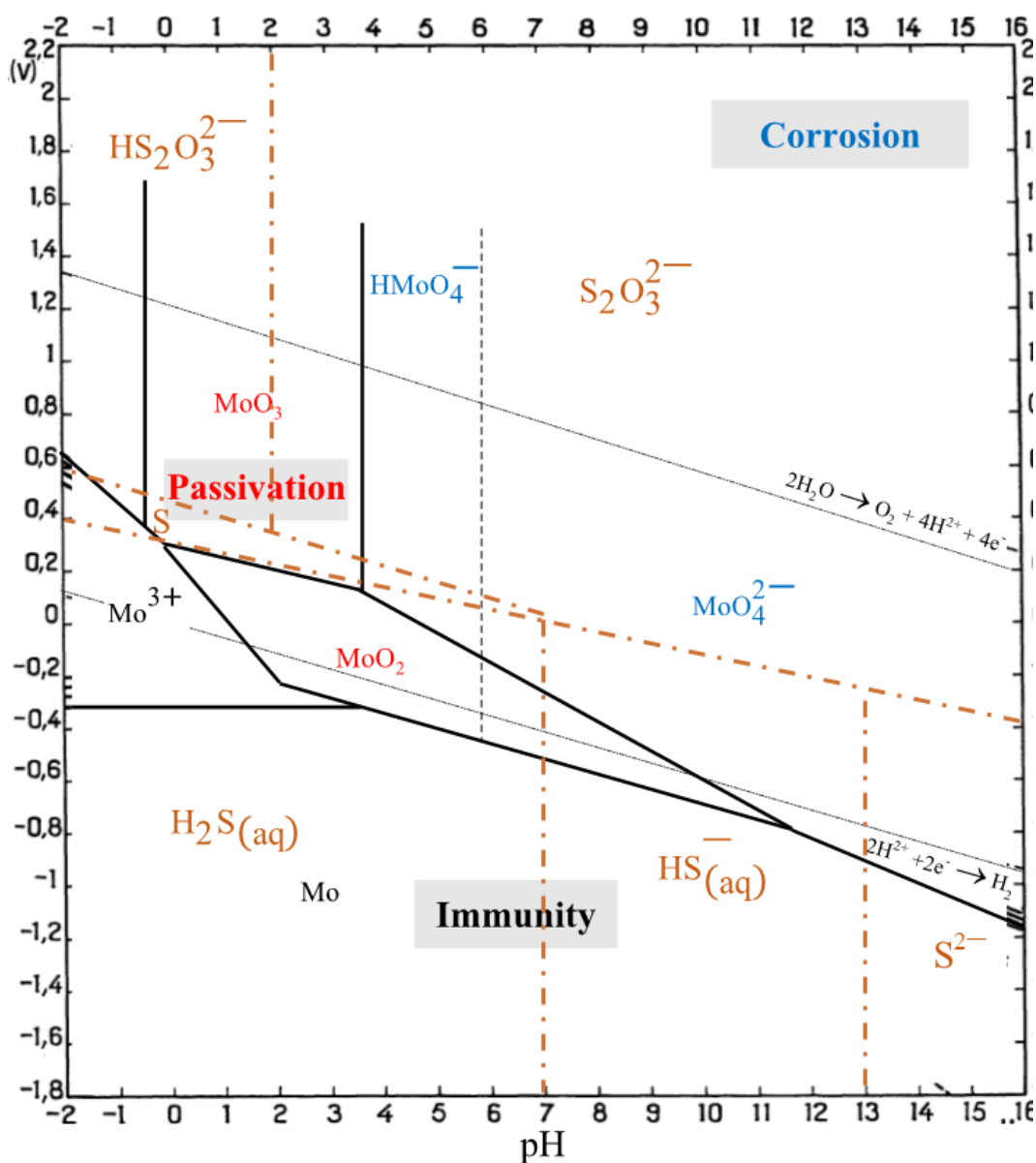
Figure 4-13 Superimposition of the two types E-pH equilibrium diagram for the system Mo-S-H_2O at 25°C [85]. The stability domains are limited by the lines: (_ .. _) H_2O systems; (_____) Mo-H_2O systems.

To consolidate all comparative results, the thiosulfate enhances the chloride effect on the passivity degradation of two duplex grades. The chloride absorption in the film may be a step of the degradation process. Adding 0.0001 to 0.1 mol/L thiosulfate in acidified ASW did not much increase the passive current density. The chloride effect on passive film is dominant in ASW.

Therefore, the cation vacancies are major defects in the passive film. On the other hand, the major defects are anion vacancy (S_O^{2-}) in the thiosulfate containing environment. The experimental results showed that the thiosulfate enhanced the corrosion rate or anodic dissolution and increased passive current density, implying it retards passive film growth in ASW. This may be the enrichment of the sulphide (S^{2-}) at the metal/film interface. At the film/solution interface, the adsorbed sulphur (S^{0}) can accept the electron to form S^{2-} by occupying the oxygen vacancy $V_O^{\bullet\bullet}$, as shown in Equation 4-9 [..]. This postulation needs evidence to be confirmed.

$$V_O^{\bullet\bullet} + S^{0} + 2e^- \longrightarrow S_O^{2-} \qquad\qquad \text{Equation 4-9}$$

The retarding effect of sulphur on the re-passivation may be caused by blocking the adsorption sites of the hydroxyl group, e.g., chromium hydroxide and increasing the anion vacancy.

In summary, the association of N and Cr in the new duplex decreased the vacancy in ASW compared with 2205 DSS. However, both may be inadequate to consume H^{+} in acidified ASW mixing with thiosulfate. The formation of stable MoO_2 in the 2205 standard duplex grade may provide less pitting susceptibility in the thiosulfate containing environment.

จุฬาลงกรณ์มหาวิทยาลัย

CHULALONGKORN UNIVERSITY

Table 4-6 The degree of defects calculated by the negative and positive slopes in capacitive measurements

Samples	Parameters	Solution conditions				
		1: ASW	2: ASW+10^{-4}M [$S_2O_3^{2-}$]	3: ASW+10^{-3}M [$S_2O_3^{2-}$]	4: ASW+10^{-2}M [$S_2O_3^{2-}$]	5: ASW+10^{-1}M [$S_2O_3^{2-}$]
New	Inner: N_A (10^{20}/cm^3)	7.844 ± 0.64	2.337 ± 0.158	2.467 ± 0.220	2.640 ± 0.189	2.705 ± 0.100
Duplex	Outer: N_D (10^{20}/cm^3)	2.503 ± 0.184	2.892 ± 0.070	2.985 ± 0.002	3.041 ± 0.002	3.325 ± 0.002
2205	Inner: N_A (10^{20}/cm^3)	8.373 ± 0.266	1.355 ± 0.001	1.395 ± 0.002	1.783 ± 0.001	2.521 ± 0.001
DSS	Outer: N_D (10^{20}/cm^3)	3.415 ± 0.018	1.685 ± 0.001	1.716 ± 0.001	1.933 ± 0.003	3.165 ± 0.020

CHAPTER 5

CONCLUSION

The new 25Cr-3Ni-7Mn-0.66N duplex stainless steel (DSS) was fabricated by the vacuum arc re-melting (VAR) process, deformed by hot-forging process, and subsequently, heat-treated at 1250°C for 1 hr + water quenched + 1050°C for 1.5 hr + water quenched. The material characterisations and chemical compositions were examined by OES, N analysis, SEM/EDX, EPMA, and XRD. The corrosion behaviours of the new duplex in artificial seawater (ASW) regarding ASTM D1141 and in ASW mixing with thiosulfate were studied at 25°C and compared with that of the standard 2205 DSS by potentiodynamic polarisation, EIS, potentiostatic polarisation and Mott-Schottky analysis. The following conclusions can be drawn:

1. The final microstructures of the new duplex are ferrite and austenite. The phase ratio of ferrite to austenite is 59:41, which were in good agreement with the Thermo-Calc diagram. There was not any intermetallic phase precipitation in the new duplex sample. The $PREN_{16}$ of ferrite is lower than austenite.

2. The electrochemical test results show that the corrosion behaviours of the new duplex grade were better than that of 2205 DSS in the ASW, but it was reversed in the acidified ASW mixing with thiosulfate.

3. The polarisation results, e.g., potentiodynamic and potentiostatic tests, showed that the values of corrosion current density (j_{corr}), passive current density (j_{pass}), steady-state current density (j_{ss}), and corrosion rate increased when thiosulfate concentrations increased.

4. The pitting resistance of ferrite is lower than that of austenite since the pit exhibits in ferrite. It is confirmed by the $PREN_{16}$ calculation results of ferrite and austenite.

5. The lower polarisation resistance (R_p) values obtained by EEC fitting in EIS analysis indicated the lesser passive film stability when thiosulfate concentrations increased.

6. The Mott-Schottky analysis confirmed the bi-layer structures of passive film in both the ASW and the acidified ASW mixing with thiosulfate. The passive film structure consists of the *p-type* semiconductor inner layer and the *n-type* semiconductor outer layer. In the ASW, the densities of cation and anion vacancies in the inner and outer layer of new duplex steel are lower than that of 2205 DSS. However, in the acidified ASW mixing with thiosulfate, the densities of cation and anion vacancies in the inner and outer layer of new duplex steel are higher than that of 2205 DSS.

APPENDIX

A. An example microstructures of new duplex and 2205 DSS samples
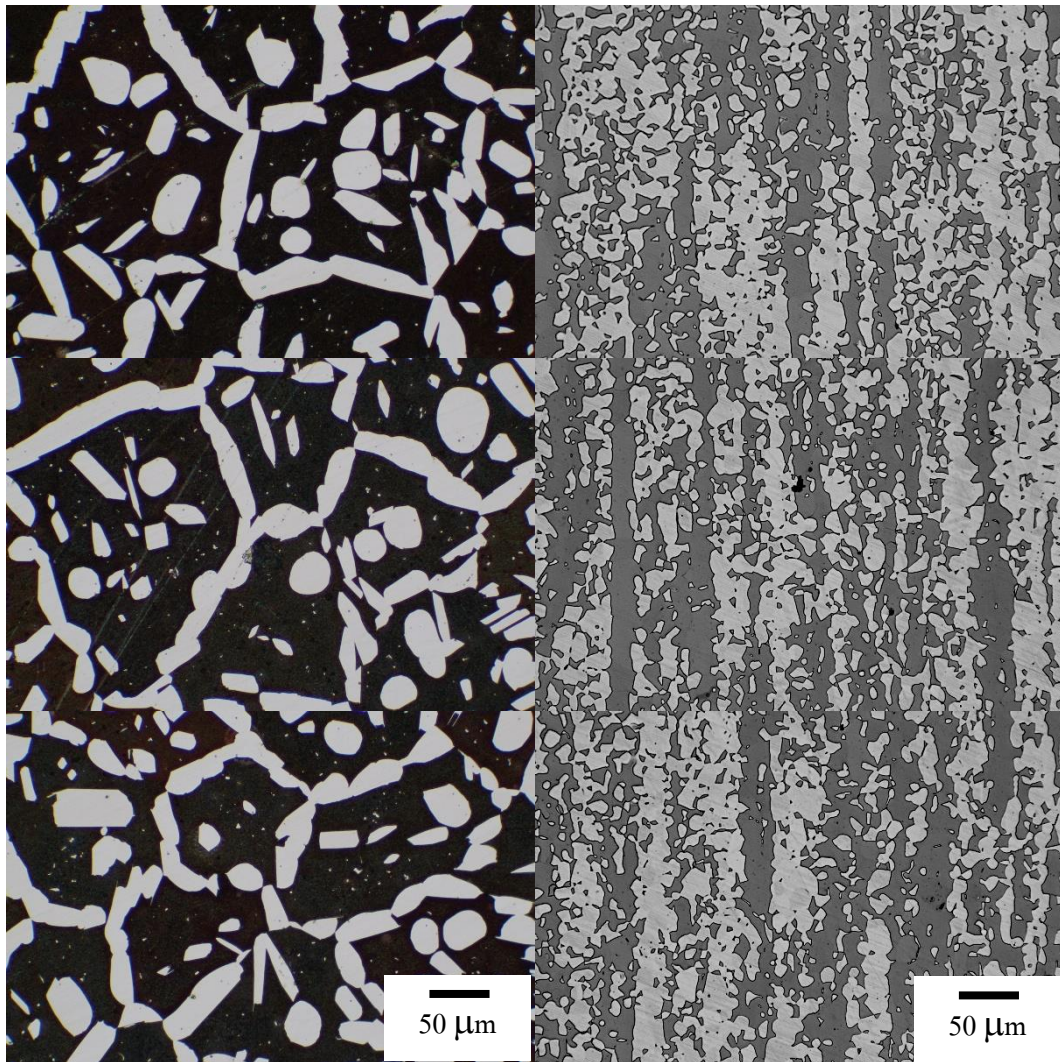
Optical microstructures of new duplex (left) and 2205 DSS (right). The dark and bright areas represent δ-ferrite and γ-austenite phases, respectively. The etchant was Beraha's solution [82].

B. Determining volume fraction by point count method (ASTM E562) [81]

Superimpose the 100 points grit upon an optical microstructure. Count and record the number of grid points, falling within the austenite phase. The below figure shows the 10×10 points grit overlaid on new duplex's microstructure simulated by Solution DT® software.
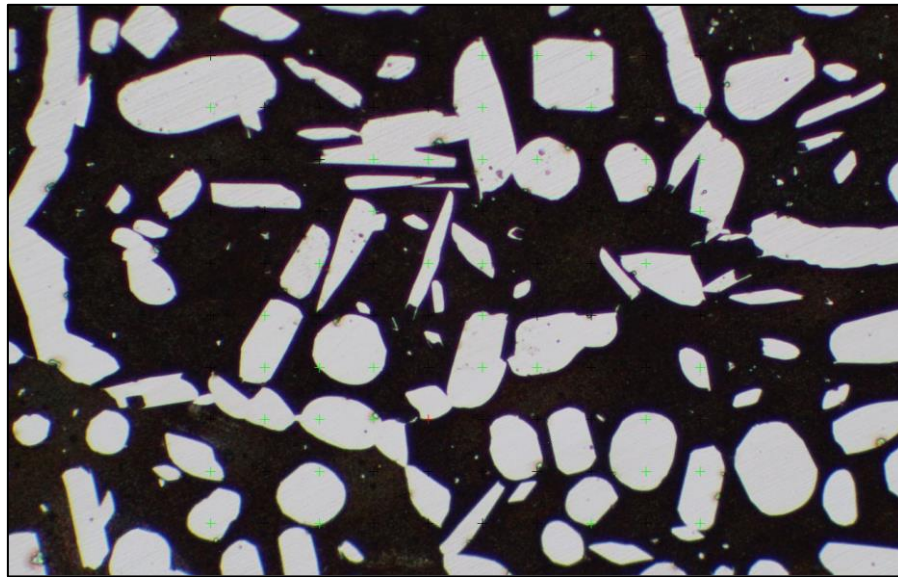
Table A1 Volume fraction of austenite phase determined by point count method

Image No.	New Duplex	2205 DSS
1	38	38
2	38	38
3	38	50
4	50	44
5	38	56
6	38	44
7	44	45
8	44	45
9	46	45
10	42	45
Averages	41	45
S.D.	4	5

REFERENCES

1. Gunn, R.N., *1 - Developments, grades and specifications*, in *Duplex Stainless Steels*, R.N. Gunn, Editor. 1997, Woodhead Publishing. p. 1-13.

2. Schulz, Z., P. Whitcraft, and D. Wachowiak, *Availability and economics of using duplex stainless steels.* NACE Corrosion, 2014.

3. Whitcraft, P., et al., *Impact of Availability and Economics on Alloy Selection.* 2014.

4. Hans, H. and G. Lothongkum, *Effects of chemical composition of duplex stainless steel on microstructure and pitting corrosion after solution heat treatment and various weld simulation cooling cycles.* Welding in the World, Le Soudage Dans Le Monde, 1994. **33**: p. 91-96.

5. Lothongkum, G., et al., *Effect of nitrogen on corrosion behavior of 28Cr-7Ni duplex and microduplex stainless steels in air-saturated 3.5 wt% NaCl solution.* Corrosion Science, 2006. **48**(1): p. 137-153.

6. Choudhary, L., D.D. Macdonald, and A. Alfantazi, *Role of thiosulfate in the corrosion of steels: a review.* Corrosion, 2015. **71**(9): p. 1147-1168.

7. Dhawale, S., *Thiosulfate: an interesting sulfur oxoanion that is useful in both medicine and industry-but is implicated in corrosion.* Journal of chemical education, 1993. **70**(1): p. 12.

8. Xia, D.-H. and J.-L. Luo, *Effects of reduced sulfur on passive film properties of steam generator (SG) tubing: an overview.* Anti-Corrosion Methods and Materials, 2019.

9. Tromans, D. and L. Frederick, *Effect of thiosulfate on crevice corrosion of stainless steels.* Corrosion, 1984. **40**(12): p. 633-639.

10. Marcus, P. and E. Protopopoff, *Thermodynamics of thiosulfate reduction on surfaces of iron, nickel and chromium in water at 25 and 300 °C.* Corrosion Science, 1997. **39**(9): p. 1741-1752.

11. Ezuber, H.M., *Influence of temperature and thiosulfate on the corrosion behavior of steel in chloride solutions saturated in CO2.* Materials & Design, 2009. **30**(9): p. 3420-3427.

12. Luo, H., et al., *Characterization of passive film on 2205 duplex stainless steel in sodium thiosulphate solution.* Applied Surface Science, 2011. **258**(1): p. 631-639.

13. Wang, Y. and P.M. Singh, *Corrosion behavior of austenitic and duplex stainless steels in*

thiosulfate-and chloride-containing environments. Corrosion, 2015. **71**(8): p. 937-944.

14. Wang, Y., et al., *Effect of thiosulfate on metastable pitting of 304L and S32101 in chloride-and thiosulfate-containing environment.* Corrosion, 2016. **72**(5): p. 628-635.

15. Zakeri, M., et al., *Pit transition potential and repassivation potential of stainless steel in thiosulfate solution.* Journal of The Electrochemical Society, 2016. **163**(6): p. C275.

16. Cui, Z., et al., *Passivation Behavior and Surface Chemistry of 2507 Super Duplex Stainless Steel in Acidified Artificial Seawater Containing Thiosulfate.* Journal of The Electrochemical Society, 2017. **164**(13): p. C856-C868.

17. He, L., Y. Wang, and P.M. Singh, *Role of Ferrite and Austenite Phases on the Overall Pitting Behavior of Lean Duplex Stainless Steels in Thiosulfate-Containing Environments.* Journal of The Electrochemical Society, 2020. **167**(4): p. 041502.

18. Zhu, M., et al., *Study on the correlation between passive film and AC corrosion behavior of 2507 super duplex stainless steel in simulated marine environment.* Journal of Electroanalytical Chemistry, 2020. **864**: p. 114072-114072.

19. Macdonald, D.D., *The Point Defect Model for the Passive State.* Journal of The Electrochemical Society, 1992. **139**(12): p. 3434-3449.

20. Liljas, M., et al., *Development of a Lean Duplex Stainless Steel.* steel research international, 2008. **79**(6): p. 466-473.

21. Knyazeva, M. and M. Pohl, *Duplex steels: Part I: Genesis, formation, structure.* Metallography, Microstructure, and Analysis, 2013. **2**(2): p. 113-121.

22. Lo, K.H., C.H. Shek, and J.K.L. Lai, *Recent developments in stainless steels*. 2009, Elsevier BV. p. 39-104.

23. Phakpeetinan, P., et al., *Effects of nitrogen and hydrogen in argon shielding gas on bead profile, delta-ferrite and nitrogen contents of the pulsed GTAW welds of AISI 316L stainless steel.* Materials Testing, 2016. **58**(6): p. 489-494.

24. Maki, T., T. Furuhara, and K. Tsuzaki, *Advances in Physical Metallurgy and Processing of Steels. Microstructure Development by Thermomechanical Processing in Duplex Stainless Steel.* ISIJ International, 2001. **41**(6): p. 571-579.

25. Grabke, H.J., *High Nitrogen Steels. The Role of Nitrogen in the Corrosion of Iron and Steels.* ISIJ International, 1996. **36**(7): p. 777-786.

26. Simmons, J.W., *Overview: High-nitrogen alloying of stainless steels.* Materials Science and Engineering A, 1996. **207**(2): p. 159-169.

27. Jiang, L.Z., W. Zhang, and Z.Y. Wang, *Research and development of lean duplex stainless steels.* Journal of Iron and Steel Research, 2013. **25**: p. 1-8+14.

28. Baddoo, N.R., *Stainless steel in construction: A review of research, applications, challenges and opportunities.* Journal of Constructional Steel Research, 2008. **64**(11): p. 1199-1206.

29. Khatami-Hamedani, H., et al., *Toward Unraveling the High Temperature Microstructure Processing Properties Relationship in a Ni-Free High Nitrogen Bearing Duplex Stainless Steel.* steel research international, 2018. **89**(6): p. 1700532-1700532.

30. Zhao, Y., et al., *Development of an easy-deformable Cr21 lean duplex stainless steel and the effect of heat treatment on its deformation mechanism.* Materials Science and Engineering A, 2017. **702**: p. 279-288.

31. David, C., et al., *Effect of grain size on the anodic dissolution of lean duplex UNS S32202 austenitic-ferritic stainless steel.* Corrosion, 2019. **75**(12): p. 1450-1460.

32. Karlsson, L., et al., *Effects of Alloying Concepts on Ferrite Morphology and Toughness of Lean Duplex Stainless Steel Weld Metals.* Welding in the World, 2013. **54**.

33. Luo, H., et al., *Electrochemical behavior of 2205 duplex stainless steel in NaCl solution with different chromate contents.* Journal of Materials Engineering and Performance, 2012. **21**(7): p. 1283-1291.

34. Örnek, C. and D.L. Engelberg, *SKPFM measured Volta potential correlated with strain localisation in microstructure to understand corrosion susceptibility of cold-rolled grade 2205 duplex stainless steel.* Corrosion Science, 2015. **99**: p. 164-171.

35. Chail, G. and P. Kangas, *Super and hyper duplex stainless steels: structures, properties and applications.* Procedia Structural Integrity, 2016. **2**: p. 1755-1762.

36. Nilsson, J.-O., *Super duplex stainless steels.* Materials science and technology, 1992. **8**(8): p. 685-700.

37. Chai, G. and P. Kangas, *New hyper duplex stainless steels.* Duplex World, 2010: p. 1043-1054.

38. Jargelius-Pettersson, R.F.A., *Application of the Pitting Resistance Equivalent Concept to*

Some Highly Alloyed Austenitic Stainless Steels. Corrosion, 1998. **54**(2): p. 162-168.

39.   Alvarez-Armas, I. and S. Degallaix-Moreuil, *Duplex stainless steels*. 2013: John Wiley & Sons.

40.   Revie, R.W., *Corrosion and corrosion control: an introduction to corrosion science and engineering*. 2008: John Wiley & Sons.

41.   Strauss, B., *Die hochlegierten Chromnickelstahle als nichtrostende Stahle.* Naturwissenschaften, 1920. **8**(41): p. 812-814.

42.   Scherer, R., G. Riedrich, and G. Hoch, *Einfluß eines Gehaltes an Ferrit in austenitischen Chrom ⁻ Nickel ⁻ Stählen auf den Kornzerfall.* Archiv für das Eisenhüttenwesen, 1939. **13**(1): p. 53-57.

43.   Schaeffler, A.L., *The Investigations of Microstructures of Single Bead Chromium-nickel Austenitic Weld Deposits on SAE 4340*. 1944: University of Wisconsin--Madison.

44.   Davis, J.R., *Stainless steels*. 1994: ASM international.

45.   Garfias-Mesias, L.F., J.M. Sykes, and C.D.S. Tuck, *The effect of phase compositions on the pitting corrosion of 25 Cr duplex stainless steel in chloride solutions.* Corrosion Science, 1996. **38**(8): p. 1319-1330.

46.   King, P.F. and H.H. Uhlig, *Passivity in the Iron-Chromium Binary Alloys.* The Journal of Physical Chemistry, 1959. **63**(12): p. 2026-2032.

47.   An, L.c., et al., *Effects of Mo and Mn on Pitting Behavior of Duplex Stainless Steel.* Journal of Iron and Steel Research International, 2016. **23**(12): p. 1333-1341.

48.   Ha, H.-Y., et al., *Interpretation of the relation between ferrite fraction and pitting corrosion resistance of commercial 2205 duplex stainless steel.* Corrosion Science, 2014. **89**: p. 154-162.

49.   Lush, P. and M. Carr, *Copper dissolution in sea water under mixed activation and diffusion control.* Corrosion Science, 1979. **19**(12): p. 1079-1088.

50.   Mao, F., et al., *Passivity breakdown on copper: influence of chloride ion.* Electrochimica Acta, 2014. **144**: p. 391-399.

51.   Haugan, E.B., et al., *Effect of tungsten on the pitting and crevice corrosion resistance of type 25Cr super duplex stainless steels.* Corrosion, 2017. **73**(1): p. 53-67.

52.   Sridhar, N. and J. Kolts, *EFFECTS OF NITROGEN ON THE SELECTIVE DISSOLUTION*

OF A DUPLEX STAINLESS STEEL. Corrosion, 1987. **43**(11): p. 646-651.

53.   Levey, P. and A. Van Bennekom, *The involvement of alloyed nitrogen in the corrosion of stainless steels.* Journal of the Southern African Institute of Mining and Metallurgy, 1995. **95**(7): p. 337-346.

54.   Jargelius-Pettersson, R.F.A., *Electrochemical investigation of the influence of nitrogen alloying on pitting corrosion of austenitic stainless steels.* Corrosion Science, 1999. **41**(8): p. 1639-1664.

55.   Zhang, Z.x., et al., *A New Series of Mo-free 21. 5Cr-3. 5Ni-x W-0. 2N Economical Duplex Stainless Steels.* Journal of Iron and Steel Research International, 2014. **21**(1): p. 69-75.

56.   Wan, J., et al., *A new resource-saving, low chromium and low nickel duplex stainless steel 15Cr-xAl-2Ni-yMn.* Materials and Design, 2014. **53**: p. 43-50.

57.   Merello, R., et al., *Influence of chemical composition on the pitting corrosion resistance of non-standard low-Ni high-Mn-N duplex stainless steels.* Corrosion Science, 2003. **45**(5): p. 909-921.

58.   Abdallah, F.M. and I.u.H. Toor, *Evaluation of Pitting Susceptibility and Secondary Phase Formation in Newly Designed Ni-Free (Fe–16Cr–1Mo–1Si–0.2N–xMn–xCu) Duplex Stainless Steel Alloys.* Arabian Journal for Science and Engineering, 2020. **45**(2): p. 599-608.

59.   Moallemi, M., et al., *On the microstructural-textural characterization and deformation analysis of a nano/ultrafine grained Fe-20Cr-8Mn-0.3N duplex alloy with superior mechanical properties.* Materials Characterization, 2019. **156**: p. 109878-109878.

60.   Lei, M.K. and X.M. Zhu, *Role of Nitrogen in Pitting Corrosion Resistance of a High-Nitrogen Face-Centered-Cubic Phase Formed on Austenitic Stainless Steel.* Journal of The Electrochemical Society, 2005. **152**(8): p. B291-B291.

61.   Fu, Y., et al., *Effects of nitrogen on the passivation of nickel-free high nitrogen and manganese stainless steels in acidic chloride solutions.* Electrochimica Acta, 2009. **54**(16): p. 4005-4014.

62.   Landolt, D., *Corrosion and Surface Chemistry of Metals*. 2007: EPFL Press.

63.   Jones, D.A., *Principles and prevention of corrosion*. 1992: Macmillan.

64.   Osozawa, K. and N. Okato, *Passivity and its breakdown on iron and iron-base alloys.*

NACE, Houston, USA, 1976. **135**.

65.   McCafferty, E., *Validation of corrosion rates measured by the Tafel extrapolation method.* Corrosion Science, 2005. **47**(12): p. 3202-3215.

66.   Dickinson, E.J.F. and A.J. Wain, *The Butler-Volmer equation in electrochemical theory: Origins, value, and practical application.* Journal of Electroanalytical Chemistry, 2020. **872**: p. 114145-114145.

67.   Lasia, A. and A. Lasia, *Introduction.* 2014, Springer New York. p. 1-5.

68.   Boukamp, B.A., *A Linear Kronig ⁻ Kramers Transform Test for Immittance Data Validation.* Journal of The Electrochemical Society, 1995. **142**(6): p. 1885-1894.

69.   Jorcin, J.B., et al., *CPE analysis by local electrochemical impedance spectroscopy.* Electrochimica Acta, 2006. **51**(51): p. 1473-1479.

70.   Hirschorn, B., et al., *Determination of effective capacitance and film thickness from constant-phase-element parameters.* Electrochimica Acta, 2010. **55**(21): p. 6218-6227.

71.   Wang, Q., et al., *A self-healing stainless steel: Role of nitrogen in eliminating detrimental effect of cold working on pitting corrosion resistance.* Corrosion Science, 2018. **145**: p. 55-66.

72.   Rahimi, E., et al., *Characterization of the passive layer on ferrite and austenite phases of super duplex stainless steel.* Applied Surface Science, 2019. **496**: p. 143634.

73.   Tsujikawa, S., et al., *Alternative for evaluating sour gas resistance of low-alloy steels and corrosion-resistant alloys.* Corrosion, 1993. **49**(5): p. 409-419.

74.   Zanotto, F., et al., *Stress-corrosion cracking behaviour of lean-duplex stainless steels in chloride/thiosulphate environments.* Metals, 2018. **8**(4): p. 237.

75.   Zanotto, F., et al., *Stress corrosion cracking of LDX 2101® duplex stainless steel in chloride solutions in the presence of thiosulphate.* Corrosion science, 2014. **80**: p. 205-212.

76.   Zhang, J., X. Hu, and K. Chou, *Effect of Thiosulfate on Corrosion Behavior and Passive Films of Duplex Stainless Steel 2205 in Chloride Solutions.* Int. J. Electrochem. Sci, 2019. **14**: p. 9960-9973.

77.   Zhang, J., et al., *Effect of solution annealing on the microstructure evolution and corrosion behavior of 2205 duplex stainless steel.* Materials and Corrosion, 2019. **70**(4): p. 676-687.

78.   Zhang, J., et al., *Electrochemical Behavior of 2205 Duplex Stainless Steel in a Chloride-*

Thiosulfate Environment. Int. J. Electrochem. Sci, 2019. **14**: p. 4144-4160.

79. Mohammadi, M., et al., *Electrochemical and Passive Layer Characterizations of 304L, 316L, and Duplex 2205 Stainless Steels in Thiosulfate Gold Leaching Solutions.* Journal of The Electrochemical Society, 2016. **163**(14): p. C883-C894.

80. Lothongkum, G., S. Chaikittisilp, and A.W. Lothongkum, *XPS investigation of surface films on high Cr-Ni ferritic and austenitic stainless steels.* Applied Surface Science, 2003. **218**(1): p. 203-210.

81. E562-19e1, A., *Standard Test Method for Determining Volume Fraction by Systematic Manual Point Count.* American National Standard, 2019.

82. Vander Voort, G., *Color metallography Vol. 9 ASM handbook.* Metallography and Microstructures, 2004: p. 493-512.

83. D1141, A., *Standard Practice for the Preparation of Substitute Ocean Water - D 1141-93 (Reapproved 2003).* American National Standard, 2003. **98**(Reapproved 2013): p. 98-100.

84. Hansen, M., K. Anderko, and H. Salzberg, *Constitution of binary alloys.* Journal of the Electrochemical Society, 1958. **105**(12): p. 260C.

85. Pourbaix, M., *Atlas of Electrochemical Equilibria in Aqueous Solution.* NACE, 1974. **307**.

86. Jin, S. and A. Atrens, *ESCA-studies of the structure and composition of the passive film formed on stainless steels by various immersion times in 0.1 M NaCl solution.* Applied Physics A, 1987. **42**(2): p. 149-165.

87. Hakiki, N.B., et al., *The electronic structure of passive films formed on stainless steels.* Corrosion Science, 1995. **37**(11): p. 1809-1822.

88. Ha, H., et al., *Effects of nitrogen on the passivity of Fe–20Cr alloy.* Corrosion Science, 2009. **51**(1): p. 48-53.

89. Boissy, C., C. Alemany-Dumont, and B. Normand, *EIS evaluation of steady-state characteristic of 316L stainless steel passive film grown in acidic solution.* Electrochemistry Communications, 2013. **26**(1): p. 10-12.

90. Rahimi, E., et al., *Characterization of the passive layer on ferrite and austenite phases of super duplex stainless steel.* Applied Surface Science, 2019. **496**: p. 143634.

91. Dai, J., et al., *Nitrogen significantly enhances corrosion resistance of 316L stainless steel in thiosulfate-chloride solution.* Corrosion Science, 2020. **174**: p. 108792.

92.   Yang, Y., et al., *Effect of annealing temperature on the pitting corrosion behavior of UNS S82441 duplex stainless steel.* Corrosion, 2013. **69**(2): p. 167-173.

93.   Taweesup, K., et al., *Corrosion behavior of Ti-Cr-N coatings on tool steel substrates prepared using DC magnetron sputtering at low growth temperatures.* Surface and Coatings Technology, 2019. **358**: p. 732-740.

94.   Orazem, M.E., et al., *Dielectric Properties of Materials Showing Constant-Phase-Element (CPE) Impedance Response.* Journal of The Electrochemical Society, 2013. **160**(6): p. C215-C225.

95.   Urquidi, M. and D.D. Macdonald, *Solute ‾ Vacancy Interaction Model and the Effect of Minor Alloying Elements on the Initiation of Pitting Corrosion.* Journal of The Electrochemical Society, 1985. **132**(3): p. 555-558.

96.   Henderson, J.D., et al., *Molybdenum surface enrichment and release during transpassive dissolution of Ni-based alloys.* Corrosion Science, 2019. **147**: p. 32-40.

97.   Lutton Cwalina, K., et al., *Revisiting the effects of molybdenum and tungsten alloying on corrosion behavior of nickel-chromium alloys in aqueous corrosion.* Current Opinion in Solid State and Materials Science, 2019. **23**(3): p. 129-141.

98.   Fernández-Domene, R.M., et al., *Passive and transpassive behaviour of Alloy 31 in a heavy brine LiBr solution.* Electrochimica Acta, 2013. **95**: p. 1-11.

99.   Fernández-Domene, R.M., et al., *Effect of alloying elements on the electronic properties of thin passive films formed on carbon steel, ferritic and austenitic stainless steels in a highly concentrated LiBr solution.* Thin Solid Films, 2014. **558**: p. 252-258.

100.   Olsson, C.-O.A., *The influence of nitrogen and molybdenum on passive films formed on the austenoferritic stainless steel 2205 studied by AES and XPS.* Corrosion Science, 1995. **37**(3): p. 467-479.

101.   Tian, H., et al., *Effect of Mo on interaction between α / γ phases of duplex stainless steel.* Electrochimica Acta, 2018. **267**: p. 255-268.

VITA

NAME	Songkran Vongsilathai
DATE OF BIRTH	19 April 1995
PLACE OF BIRTH	Nonthaburi, TH
INSTITUTIONS ATTENDED	M.Eng. Chulalongkorn Univerisity
	B.Eng. King Mongkut University of Technology North Bangkok
HOME ADDRESS	35/178, Soi Bangsrimuaeng 47
	Thanamnon Road,
	Nonthaburi, TH
	11000
PUBLICATION	Corrosion behavior of a new 25Cr-3Ni-7Mn-0.66N duplex stainless steel in artificial seawater
	Material Testing 63 (2021) 6, pages 505-511, DOI 10.1515/mt-2020-0086
AWARD RECEIVED	The 3rd international Thailand Corrosion and Prevention Corrosion Control Conference (TCPC) presentation 2019

จุฬาลงกรณ์มหาวิทยาลัย

CHULALONGKORN UNIVERSITY